Ironless Inductive Position Sensor for Harsh Magnetic Environments

THÈSE N^{O} 5596 (2013)

PRÉSENTÉE LE 11 JANVIER 2013

À LA FACULTÉ DES SCIENCES ET TECHNIQUES DE L'INGÉNIEUR
LABORATOIRE D'ACTIONNEURS INTÉGRÉS
PROGRAMME DOCTORAL EN SYSTÈMES DE PRODUCTION ET ROBOTIQUE

ÉCOLE POLYTECHNIQUE FÉDÉRALE DE LAUSANNE

POUR L'OBTENTION DU GRADE DE DOCTEUR ÈS SCIENCES

PAR

Alessandro DANISI

acceptée sur proposition du jury:

Prof. R. Clavel, président du jury
Prof. Y. Perriard, Dr A. Masi, directeurs de thèse
Prof. H. Bleuler, rapporteur
Dr M. Buzio, rapporteur
Prof. C. Espanet, rapporteur

ÉCOLE POLYTECHNIQUE
FÉDÉRALE DE LAUSANNE

Suisse
2013

Ai miei genitori
Ad Emanuela
A Christian

Acknowledgments

The thesis you are holding in your hands actually constitutes the final chapter of my academic education history. It is the result of three years of research which for me have been a constant challenge and, at the same time, a lot of fun.

For having had trust in my research capabilities, I would like to thank Roberto Losito and Alessandro Masi from the European Organization for Nuclear Research (CERN), who have been closely following my progresses. Roberto Losito gave me the opportunity to join the EN-STI group and carry on an exciting research project. Alessandro Masi went well beyond his duty of thesis co-director: he has been a mentor and a friend, always suggesting me the best for my research after examining my work with critical look day by day.

Prof. Yves Perriard and Dr. Miroslav Markovic have been my reference points at the Swiss Federal Institute of Technology Lausanne (EPFL). Prof. Perriard has been a helpful tutor and a friendly guide along these three years. With his help, I understood how to shape a good research work. Dr. Markovic has always done his best to make me feel part of the Integrated Actuators laboratory; his suggestions on my research are those of a friend, as well as a scientist.

I would also like to thank Dr. Daho Taghezout (Applied Magnetics) and Aldo Reggiani (SwissCoils) for the support on the FEM simulations and the prototype manufacturing. Dr. Taghezout's assistance sometimes translated in actual solution-hunting collaborations which always reached the goal. Aldo Reggiani has been a sound reference as far as prototype manufacturing issues were concerned and always tested his expertise to the limit in order to fulfil our requirements.

Among the many young people I have met during these three years, I would like to thank the CERN guys from my section with whom I have had the pleasure to work and share countless great and funny experiences, whether long (one among all, the trip in Baden-Baden) or short. In particular, I would like to thank Pascal Oser (willsch auch a bier?), Raffaello Secondo, Lefteris Fadakis, Clement Derrez, Salvatore Danzeca, Fabrizio Marazita, Ricardo Picatoste. I will not forget the nights and the amazing concerts and festivals spent together, the discussions about eternal topics, the wireless communication between cars, as well as the Silver Star (!). The (un)official italian team at CERN never made me feel alone: for this reason, I would like to thank Giovanni de Michele, Cinzia Luzzi, Carlo Zannini, Tatiana Rijoff, Giovanni Iadarola, Michele Martino. I also had the chance to participate to a prestigious course on accelerator's physics in Greece, where I met good friends from a lot of countries. Among them, I would like to thank Eirini Koukovini, Philippe Schoofs, Nicoló Biancacci, Andrea Pesce and Agnieszka Priebe.

A special thanks goes to Giovanni Spiezia for his life suggestions, Mario di Castro for his honest and precious support regarding all aspects of work and life, Mark Butcher for his patience with my English questions (which always got an answer), Eric Vire and Katarzyna Stachyra for their support on the measurements, Valeria Amoroso for the priceless sacrifice of having a ride on the Wodan with two insane guys. Finally, I would like to thank all the people from EN/STI-ECE, who always made me feel like working among friends and not only among colleagues: thanks to Paul, Julien, Jarek, Christophe, Philippe, Jerome, Mathieu, Sergio, Jean-Yves and the people from the labs.

Working far from home and spending a lot of energy on a challenging research not always entail bright days. Nevertheless, in good and in bad moments, I could always count on the endless support of my parents and my girlfriend, who were always supporting me and understanding the sacrifice of a hard work for a good result. Since the beginning, they never had a single doubt on my potentialities and once again they will be there watching me accomplishing another objective. I hope I will make them be proud of me once more. It will be my way to say thank you. My brother Christian is also somehow “used” to my dissertations and I am looking forward to be a member of the audience for his future ones. Our tie let us live a lot of adventures in these three years (Trift, Gelmer, Rust, Bala New York!) and our determination and willpower in obtaining results carried us to the finish line of the 2012 Berlin Marathon.

Adesso, anche questa maratona sta per finire. Questa tesi è dedicata ai miei genitori, ad Emanuela e a Christian ed a loro va il mio ringraziamento piú grande, semplicemente per essere lí, sia vicini che lontani.

Abstract

Linear Variable Differential Transformers (LVDTs) are widely used for high-precision and high-accuracy linear position sensing in harsh environments, such as the LHC collimators at CERN. These sensors guarantee infinite resolution and long lifetimes thanks to contactless sensing. Furthermore, they offer very good robustness and ruggedness, as well as micrometer uncertainty over a range of centimeters when proper conditioning techniques are used (such as the three-parameter Sine-Fit algorithm). They can also be adapted to be suitable for radioactive environments. Nevertheless, an external DC/slowly-varying magnetic field can seriously affect the LVDT reading, leading to important position drifts (e.g. hundreds of micrometers), often unacceptable in high-accuracy applications. The effect is due to the presence of non-linear ferromagnetic materials in the sensor's structure.

A detailed Finite Element model of an LVDT is first proposed in order to study and characterize the phenomenon. The model itself becomes a powerful design tool for possible countermeasures to the interference effect. In particular, a combination of magnetic shielding and DC polarization is proposed to reduce the drift due to the external field. Nevertheless, such solutions cannot lead to complete immunity, given the unavoidable presence of magnetic materials in the sensor.

Taking the CERN application as a starting point, this thesis aims at conceiving, modelling and characterizing a valid alternative to LVDTs for harsh magnetic environments, which would guarantee magnetic-field-immune position sensing while keeping all the advantageous properties of LVDTs.

The Ironless Inductive Position Sensor (I2PS) is an air-cored structure made of 5 coaxial coils. The position sensing is achieved by spatially-variable magnetic fluxes, which give rise to position-dependent coil voltages, just as for LVDTs. The complete electromagnetic model of the sensor is proposed, showing the working principle and demonstrating the magnetic-field immunity from a theoretical viewpoint. In addition, a high-frequency electromagnetic analysis is performed, in order to model the skin and proximity effects in the conductors and foresee their impact on the sensor's functioning. The models are validated with FEM simulations and experimental measurements. The thermal behaviour of the sensor is also investigated and an effective compensation algorithm is proposed to cancel the temperature-dependence of the position reading. In addition, a smart real-time reading algorithm is proposed in order to significantly reduce the estimation error of standard three-parameter Sine-Fit algorithms when an additional sinusoidal signal is present on the main waveform. Finally, a generic optimization procedure is proposed in order to maximize the performances of the sensor in terms of sensitivity.

Taking this procedure as a guideline, an actual I2PS optimized prototype is designed and manufactured, having the specifications of the LHC collimators application as a reference. The optimized prototype shows immunity to external ramped and sinusoidal fields, as expected. In addition, it is used for the experimental validation of the models and the reading techniques, which demonstrate their effectiveness.

Keywords: electromagnetic modelling, finite element method, linear variable differential transformer, skin effect, proximity effect, Maxwell's equations, digital signal processing, thermal effects, optimization procedure.

Résumé

Les LVDTs (de l'anglais Linear Variable Differential Transformer) sont largement utilisés pour la détection de position linéaire dans des conditions extrêmes, telles celles qu'imposent les collimateurs du LHC au CERN. Ces capteurs montrent une résolution infinie et une très grande durée de vie grâce à leur principe de mesure sans contact, ainsi qu'une incertitude de mesure de l'ordre du micromètre sur une échelle centimétrique en utilisant un conditionnement du signal adapté (algorithme sine-fit à trois paramètres). Ils peuvent même être adaptés pour un environnement radioactif. Néanmoins, un champ magnétique continu ou variant lentement peut introduire une dérive en position importante (centaines de micromètres) et souvent inacceptable dans le cas des mesures à haute précision. Cet effet est dû à la présence de matériaux magnétiques non-linéaires.

Un modèle à éléments finis d'un LVDT est proposé, dans le but de caractériser le phénomène. Ce modèle devient lui-même un puissant outil de design pour réaliser des contres mesures de cette interférence. En particulier, la combinaison d'un blindage magnétique et d'une polarisation DC est proposée pour réduire la dérive en position. Néanmoins, de telles solutions ne peuvent pas apporter une immunité, étant donné la présence obligatoire de matériaux magnétiques dans le capteur.

En prenant l'application du CERN comme point de départ, cette thèse vise à concevoir, modéliser et caractériser une alternative aux LVDTs en environnement magnétique, qui garantirait une mesure de position immunisée contre les champs magnétiques, tout en conservant les propriétés des LVDTs.

Le capteur de position inductif sans fer (I2PS de l'anglais Ironless Inductive Position Sensor) est une structure constituée de 5 bobines coaxiales sans noyau. La détection de position repose sur la variation spatiale des flux magnétiques, qui engendrent des tensions proportionnelles à la position, comme dans le cas d'un LVDT. Le modèle électromagnétique complet du capteur est proposé, le principe de fonctionnement est présenté de manière analytique et l'immunité aux champs magnétiques est démontrée. De plus, une analyse électromagnétique aux hautes fréquences est réalisée pour modéliser les effets de peau et de proximité dans les conducteurs et de prévoir leur impact sur le fonctionnement du capteur. Les modèles sont validés par simulations et mesures expérimentales. Les effets thermiques sont également examinés et un algorithme efficace de compensation est proposé afin d'annuler la dépendance en température des mesures de position. De plus, un algorithme de lecture en temps réel intelligent est conçu afin de réduire sensiblement l'erreur dans l'estimation de l'algorithme Sine-fit à 3 paramètres lorsqu'un signal sinusoïdal supplémentaire est présent dans l'onde principale. Enfin, une procédure d'optimisation générique est proposée afin de maximiser les performances du capteur en termes de sensibilité.

En prenant cette procédure comme directive, un prototype d'I2PS est conçu et produit, ceci en conservant les spécifications des collimateurs du LHC comme référence. Comme prévu, le prototype montre une immunité aux champs externes de types rampes et sinusoïdes. Il est de plus utilisé dans la validation expérimentale des modèles et techniques de lecture, qui démontrent leur efficacité.

Mots clefs: Modélisation électromagnétique, méthode des éléments finis, LVDT, effet de peau, effet de proximité, équations de Maxwell, effets thermiques, traitement du signal numérique, procédure d'optimisation.

Ironless Inductive Position Sensor for Harsh Magnetic Environments

Table of Contents

List of Figures

List of Tables

Chapter 1
Introduction

Abstract

In this chapter, an introduction on the scientific topic of the research and an overview of the Large Hadron Collider (LHC) project is proposed. The latter constitutes the specific application from which the more generic research work of the thesis was born. A description of the LHC Collimators is also addressed, giving more attention to details which will be useful for the scientific and engineering discussions of the next chapters.

1.1. Scientific Background

The research work presented in the next chapters is in the wide framework of applied electromagnetics. In particular, it involves the electromagnetic and thermal modelling of an ironless inductive position sensor, together with the conception of the reading techniques. When possible, the research is conducted without specifically referring to a particular application, so as to keep the nature of generality and enable the use of the presented methods for other kinds of applications. However, when the sensor's operative constraints (e.g. for comparison with existing sensors' performances, state-of-the-art investigations, choice of parameters, optimization) or applicative examples have to be addressed, the application of linear position sensing in the collimators of the Large Hadron Collider has been considered. Moreover, the problem that this research work proposes to solve (i.e. the magnetic interference on particular ferromagnetic linear position sensor) has been observed first in this environment. Therefore, this application constitutes also the starting point for the general scientific research which is proposed in the next chapters.

1.2. The Large Hadron Collider (LHC)

This section briefly introduces the wide framework of the Large Hadron Collider (LHC), a particle accelerator built at the European Organization for Nuclear Research (CERN), and its specific collimation system. This introduction allows a better understanding of the performances and constraints for the linear position sensor which will be discussed in the next chapters. However, as already advanced in the previous section, the scientific purpose of the pure research is kept general, addressing the CERN's application as a case study.

1.2.1 Fundamentals of Particle Accelerators' Physics

A particle accelerator is a complex system which makes use of electromagnetic fields to confine, guide and accelerate elementary particles (such as electrons or protons) to high speeds and use them for experiments or collisions.

Electrons and protons exist in all materials, but they must be separated out for using them in an accelerator. Electrons are usually produced by an "electron gun", which contains a cathode which is heated so that electrons separate from the atoms. The emitted electrons are attracted toward an anode where they pass through a hole. Protons are produced starting from hydrogen gas. The

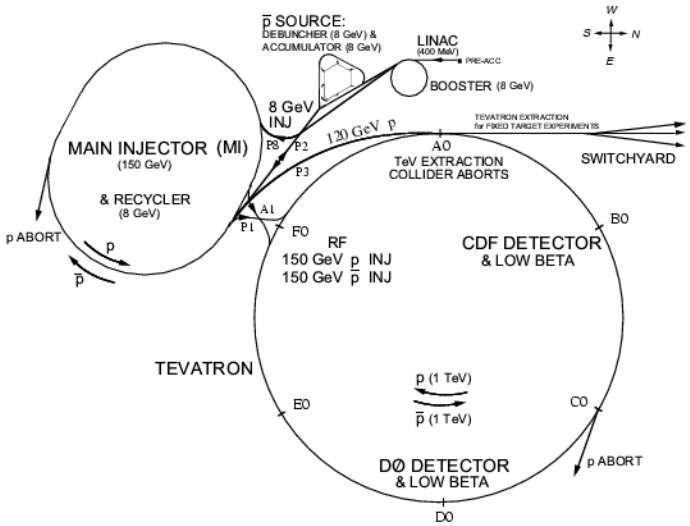

Figure 1.1. A circular (or cyclic) accelerator (in this example, the Tevatron from Fermilab and its main injector). In the accelerator complex, there are also LINACs and transfer lines. The energy is reported in eV. (Source: Fermi National Accelerator Laboratory homepage fnal.gov).

electrons and protons are separated in an electric field (i.e. the gas is ionized) and the protons escape through a hole [1].

The key-feature of a particle accelerator is the accelerating electric field. The simplest method to realize that is a voltage giving rise to a uniform static field between positive and negative electrodes. The consequent electrical force pushes the electron towards the positive potential, increasing its velocity and its energy. The energy an electron gains traveling through a potential difference of 1 Volt is defined as 1 electron-Volt (eV, equivalent to $1.6 \cdot 10^{-19}$ Joules) [2].

A more practical realization is to use several stages of weak electric fields set up by low voltage equipment. This is the principle involved in linear accelerators (or LINACs, not treated in this section) and cyclic accelerators (Figure 1.1). In the latter, the particles are guided on a circle many times through the same small electric fields. The final energy depends on the cumulative effect of the fields.

The repetitive structure of a cyclic accelerator naturally suggests the use of alternating rather than DC voltages to create the accelerating field. Both linear and cyclic accelerators generally use the alternating electric fields in electromagnetic waves at radio or microwave frequencies (100 to 3000 MHz) to accelerate the particles [3].

The electromagnetic wave is set up so that, when the particles arrive in the cavity, the electric field is in the right direction to provide acceleration. This task can be achieved with a standing wave (i.e. a superposition of travelling waves moving in opposite directions). Alternatively, for very fast-moving electrons, which travel very close to the speed of light (in other words, close to the speed of the wave itself), a traveling wave can be used for acceleration [3, 4].

A primary-role effect in acceleration with alternating electric field is the “phase stability” [1, 3-5]. If a particle whose velocity is increasing arrives too soon as the field rises, it will not experience a field as high as it should and so will receive a reduced acceleration. Therefore, when it reaches the next accelerating cavity, it will arrive late and will receive a higher acceleration. The net effect will be

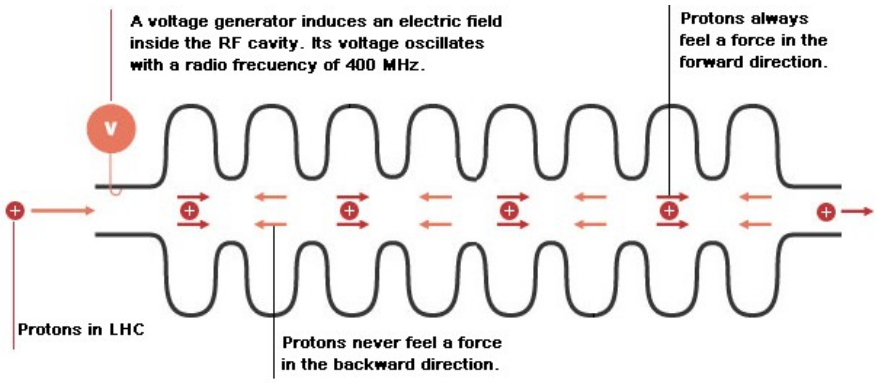

Figure 1.2. Radio-frequency accelerating cavity in the Large Hadron Collider. The time of arrival of the particle is synchronized with the oscillating field. (Source: lhc-closer.es).

phase stability: the particle will be kept in phase with the field in each accelerating region (Figure 1.2). Another effect will be a grouping of the particles in time, so that they will form a train of bunches rather than a continuous beam of particles.

Magnetic fields also play an important role, as they can change the direction of charged particles, according to the Lorentz force (in vector notation)

$$\boldsymbol{F} = q\boldsymbol{E} + q\boldsymbol{v} \times \boldsymbol{B} \tag{1.1}$$

where $\boldsymbol{B}$ is the magnetic flux density vector, q is the charge, $\boldsymbol{v}$ the particle speed vector and $\boldsymbol{E}$ the electric field vector. This means that magnets can be used to bend particle beams along a circular path, so that they pass repeatedly through the same accelerating cavities. This effect is widely used in cyclic accelerators such as cyclotrons and synchrotrons and is achieved by means of the so-called dipole magnets (Figure 1.3) [3, 4, 6].

Particular electromagnets in particle accelerators are also used to focus the particle beams, in order to keep them as narrow and intense as possible. This is the case of a quadrupole (Figure 1.3), a magnet built with four poles arranged in opposite ways. This configuration pushes the particles

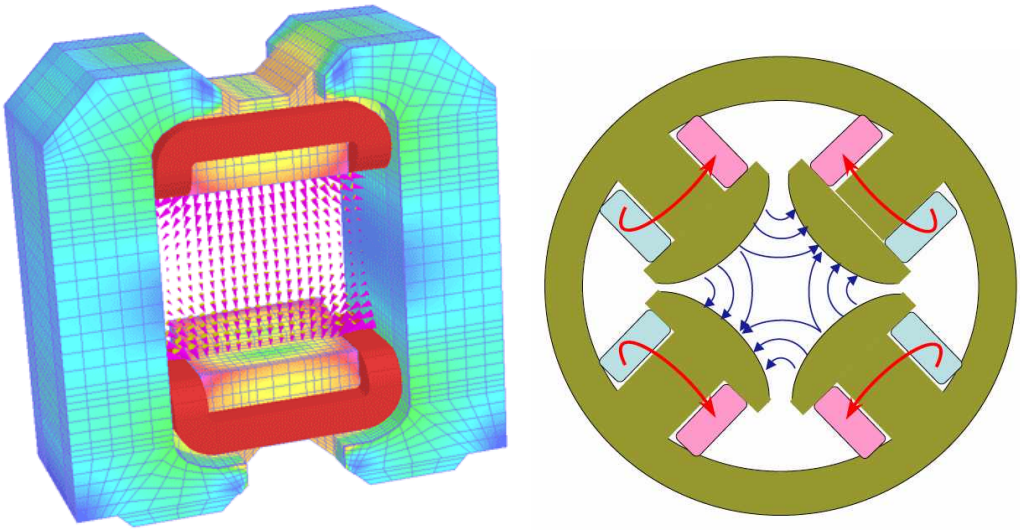

Figure 1.3. (Left) Magnetic flux density distribution on a dipole magnet. (Source: Vector Fields software cobham.com). (Right) Configuration of a quadrupole magnet. The blue and pink rectangles indicate the coils (Source: UCLA Particle Beam Physics Laboratory homepage pbpl.physics.ucla.edu)

toward the center in one direction and away from the center in the perpendicular direction. Therefore, quadrupole magnets must be used in pairs in order to provide proper focusing. Magnets with larger numbers of poles (e.g. sextupoles and octupoles) are also used for more-sophisticated focusing.

As the speed (i.e. the energy) of the circulating particles increases, the strength of the magnetic field used to guide them is also increased, thus keeping them always on the same path [5, 6]. Injection and extraction of a particle beam in a storage ring is usually achieved by means of so-called kicker magnets, particular electromagnets that switch on just long enough to "kick" the particles (e.g. out of the synchrotron ring and along a beam line) [6]. When the beam is extracted, the fields in the dipole magnets are then ramped down, and the machine is ready to receive its next pulse of particles.

1.2.2. Particles Collision

Many particle accelerators are set up with two different storage rings with two beams circulating in opposite directions. The beams are then colliding in specific points where the two rings meet. A major advantage of such machines is that when two beams collide head-on, the energy of the particles turns directly into the energy of the interactions between them. This is not the case when an energetic beam collides with material at rest: in this case much of the energy is lost in setting the target material in motion, in accord with the principle of conservation of momentum [1, 3, 4].

As already pointed out, the beam in a synchrotron is not a continuous stream of particles but is clustered into bunches. A bunch may be a few centimeters long and a tenth of a millimeter large, and it may contain about 10^{12} particles (the value depends on the specific accelerator). However, this is not a very high concentration: normal matter of similar dimensions contains about 10^{23} atoms. Thus, when two particle bunches cross in a colliding-beam machine, there is only a very small chance that two particles will actually interact. The particles can indeed continue around the ring and intersect again. To enable this repeated beam crossing, the vacuum in the rings of colliding-beam machines must be particularly good so that the particles are not lost due to collisions with residual air molecules.

1.2.3. The role of the Large Hadron Collider

The Large Hadron Collider (LHC) is the world's largest and highest-energy particle accelerator. It has been built by the European Organization for Nuclear Research (CERN), the largest particle physics laboratory in the world, near Geneva, across the Franco-Swiss border (Figure 1.4). The LHC has been completed on July 2008 and tested for the first time on September the 10th, 2008 with its first circulating beam [7].

It is theorized that the collider will produce the Higgs boson, the last unobserved particle among those predicted by the Standard Model[1]. The verification of the existence of the Higgs boson would also explain the mechanism of electroweak symmetry breaking [9, 10], through which the particles of the Standard Model are thought to acquire their mass.

[1] The Standard Model is a theory that describes the three fundamental forces, which are the electro-magnetism, the weak nuclear interaction and the strong nuclear interaction, as well as all the particles that form the matter. The gravity is not considered [8].

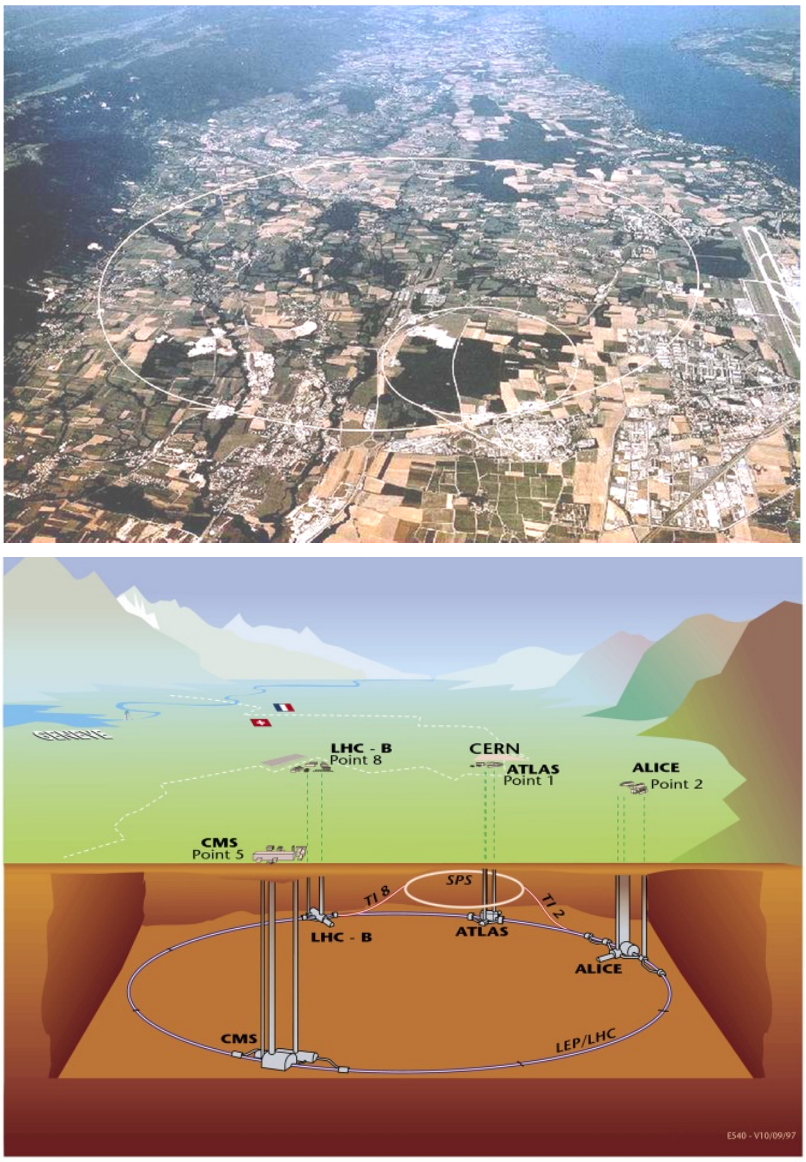

Figure 1.4. (Top) Aerial view of the Large Hadron Collider area with highlighted the cycle of the CERN's accelerators. (Bottom) Scheme of the Large Hadron Collider experiments and their access points on the surface. (Source: cern.ch).

The LHC physics program is mainly based on proton–proton collisions. However, shorter running periods, typically one month per year, with heavy-ion collisions are included in the program. While lighter ions are considered as well, the baseline scheme deals with lead ions. The aim of the heavy-ion program is to provide a window on a state of matter known as Quark-gluon plasma, which characterized the early stage of the life of the Universe [11].

The collider is contained in a circular tunnel, with a circumference of 27 kilometres, at a depth ranging from 50 to 175 metres underground (Figure 1.4). The 3.8-m-wide concrete tunnel, built between 1983 and 1988, was formerly used to house the Large Electron-Positron Collider (LEP) [12]. It crosses the border between Switzerland and France at four points, with most of it in France. Surface buildings hold auxiliary equipment such as compressors, ventilation equipment, control electronics and refrigeration plants.

The collider tunnel contains two adjacent parallel beam rings that intersect at four points, each

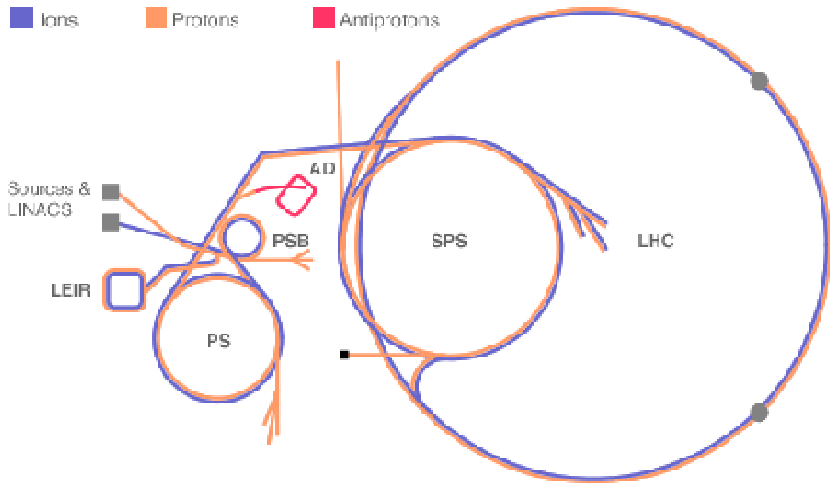

Figure 1.5. The CERN's accelerators complex (Source: lhcathome.web.cern.ch).

containing a proton beam. 1232 dipole magnets keep the beams on their circular path, while additional 392 quadrupole magnets are used to keep the beams focused, in order to maximize the chances of interaction. In total, over 1600 superconducting magnets are installed, with most weighting over 27 tons. Approximately 96 tons of liquid helium are needed to keep the magnets at their operating temperature, making the LHC the largest cryogenic facility in the world at liquid helium temperature [1].

Prior to being injected into the main accelerator, the particles are prepared by a series of systems that successively increase their energy, as depicted in Figure 1.5. The first system is the linear particle accelerator LINAC 2 generating 50 MeV protons, which feeds the Proton Synchrotron Booster (PSB). There the protons are accelerated to 1.4 GeV and injected into the Proton Synchrotron (PS), where they are accelerated to 26 GeV. Finally the Super Proton Synchrotron (SPS) is used to further increase their energy to 450 GeV before they are at last injected into the main LHC ring. Here the proton bunches are accumulated, accelerated (over a period of 20 minutes) to their

Maximum kinetic of a proton	7 TeV
Field strength of dipole magnets	8.33 T
Number of particles per bunch	1.1×10^{11}
Circulating current per beam	0.54 A
RMS bunch length	7.5 cm
Bunch spacing	25 ns
Tunnel circumference	27 km
Number of bunches around ring	2808
Number of dipole magnets	1232
Length of each dipole magnets	14.3 m
Maximum proton velocity	0.99999991c
Injection Energy	450 GeV
Energy loss per turn	6.7 keV

Table 1.1. General operational data regarding dimensional, magnetic and particle parameters of the Large Hadron Collider.

Figure 1.6. The Compact Muon Solenoid (CMS) experiment during construction (Source: cern.ch).

peak 7 TeV energy, and finally circulated for 10 to 24 hours while collisions occur at the four intersection points. The general data are summarized in Table 1.1.

Six detectors have been designed and built at the LHC, located underground in large caverns excavated at the LHC's intersection points. Two of them, the ATLAS experiment and the Compact Muon Solenoid (CMS, Figure 1.6), are large, general purpose particle detectors. A Large Ion Collider Experiment (ALICE) and LHCb have more specific roles and the last two (TOTEM and LHCf) are much smaller and for specialized research.

CMS and ATLAS are used to look for signs of new physics, including the origins of mass and extra dimensions. ALICE studies a "liquid" form of matter called quark-gluon plasma that existed shortly after the Big Bang. Equal amounts of matter and anti-matter were created in the Big Bang. LHCb investigates what happened to the "missing" anti-matter.

On July the 4th, 2012, ATLAS and CMS announced separately the discovery of a new particle at the energy of 125 GeV with a local significance of 5 sigma (less than 1 in 10^6 chances of error). Even if there is not the certainty of the fact that this new particle is actually the Higgs Boson, the observations are so far consistent with that [13]. Further confirmation will require more precise data on some of the characteristic of the new particle.

1.3. The LHC Collimation System

To assure machine protection and guarantee the safety during nominal operation, a particle accelerator is usually equipped with collimators, complex devices whose main function is to physically narrow the beam of particles in the transversal plane. By doing so, the particles in excess (i.e. outer part of the beam halo) are cleaned and the protection of the superconducting magnets is

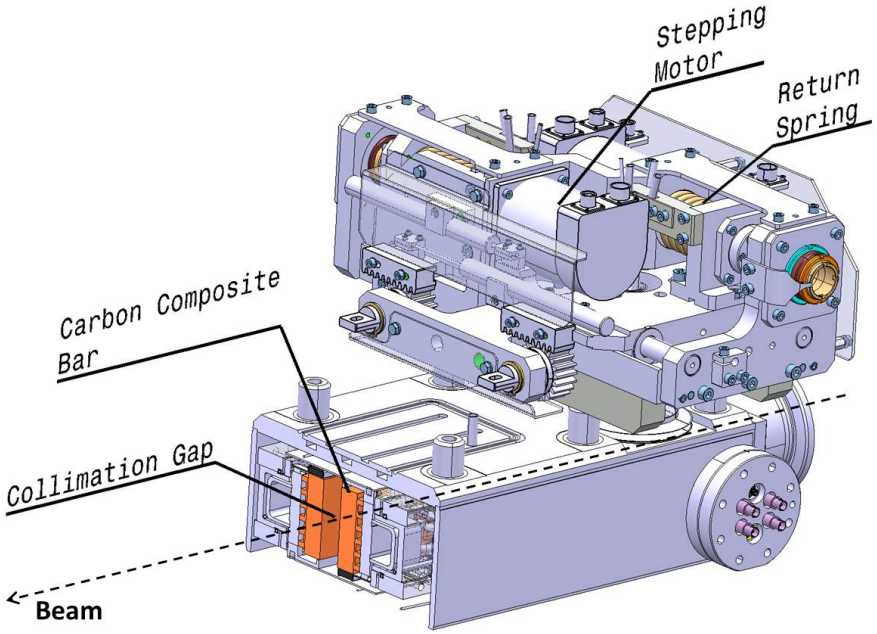

Figure 1.7. Half 3D reconstruction of an LHC collimator (Source: CERN EN/STI Group). The graphite jaws are typically 1.2-m long and about 10-cm-high. They move on the transversal plane to the beam direction.

assured. In this section, the collimation system of the Large Hadron Collider is briefly described, focusing on the assembly and the sensors' system, since they constitute the applicative example of the scientific work carried out in the next chapters. The LHC is equipped with 107 collimators all along its 27-km circumference.

1.3.1. Design Goals

In the Large Hadron Collider, each of the two rings handles a stored beam energy of up to 350 MJ ($3 \cdot 10^{14}$ protons at 7 TeV). This makes the LHC beams highly destructive. At the same time the superconducting magnets in the LHC would quench[2] at 7 TeV if small amounts of energy (on the level of 30 mJ/cm^3, induced by a local transient loss of $4 \cdot 10^7$ protons) are deposited into the superconducting magnet coils. Any significant beam loss must therefore be avoided. However, beam losses cannot be completely suppressed. The handling of the high-intensity LHC beams and the high loss rates of protons requires a collimation system with the following functionalities [14]:

- Efficient cleaning of the beam halo such that beam-induced quenches of the superconducting magnets are avoided during routine operation.
- Minimization of halo-induced background noise in the particle physics experiments.
- Passive protection of the machine aperture against abnormal beam loss. Beam loss monitors at the collimators detect any unusually high loss rates and generate a beam abort trigger.
- Scraping of beam tails.

The collimators must be sufficiently robust to fulfil these tasks without being damaged both during normal and abnormal operational conditions. Nevertheless, any possible hardware solution

[2] The magnet quench is an abnormal situation where parts of the superconducting coils enter the normal-conducting state. These parts are therefore subject to sudden Joule heating, which on turn makes other parts of the coils exit the superconducting state. This creates a chain reaction which rapidly makes the entire magnet reach the resistive state, with a consequent bang due to the sudden conversion of magnetic energy into heat. The cryogenic fluid boils off and there may be voltage spikes and arcing [6].

for the collimators can only resist a small fraction of the LHC beam.

1.3.2. Collimator's Assembly

The mechanical design of collimators (Figure 1.7) that can withstand the high intensity LHC beam is a hard task. Collimators do not only need to be very robust but at the same time quite long and very precise (small collimation gaps).

The small minimum collimation aperture (gap size) of 0.5 mm and the small beam size at the collimators (200 μm) imply tight mechanical tolerances [14]. These are relaxed for initial running. The mechanical parts which actually enter in contact with the beam (the so-called jaws, two blocks of graphite depicted in orange in Figure 1.7) must be remotely movable with good precision and positioned with very low uncertainty (± 10 μm). Reproducibility of settings is crucial in order to avoid long re-optimizations. The absolute opening of the collimator gap is safety-critical and must be known at all times with good accuracy.

The main technical features of the LHC secondary collimators are:

- An internal alignment system allowing both lateral displacement and angular adjustment.
- A plug-in external alignment system, allowing a quick and simple positioning of the collimator assembly in the machine.
- A precise actuation system including a semi-automatic mechanical return and a misalignment prevention device.
- A motorization and a control set.

The system is free from the effect of vacuum force.

1.3.3. Sensors' System

A Position Readout and Survey (PRS) system has been defined [15] in order to ensure the level of machine safety required by the LHC. The required precision of positioning is one tenth of the beam core diameter, which at nominal energy is about 200 μm. Therefore, 20 μm is assumed as a design feature for the precision.

The PRS verifies in real time the actual position of the jaw. Depending on the type and energy of the circulating beams, the PRS is enabled to trigger a beam abort in case of discrepancy between the desired and the measured position of the jaw. Each jaw can be moved on both ends by stepping motors that can position it at a well-defined angle and distance with respect to the nominal beam trajectory [14, 15].

Linear position sensors (which will be presented in Chapter 2) have been chosen to measure the jaw position; 7 specifically-designed position sensors are installed on each collimator, while each PRS controls up to three collimators (primary, secondary and tertiary collimators). Therefore, it should take position signals from 21 sensors at the same time. Overall, the PRS systems have to monitor in real time more than 700 position sensors (since more than 100 collimators are installed in the machine).

The PRS is required to be independent from the Motor Drive Control (MDC), the module that directly controls the motion of the stepping motors, in order to increase the overall reliability of the control system [15]. Two chassis with two different controllers are therefore attached to one, two or

three collimators and host one the MDC and the other the PRS. The two PXI chassis are completely independent, and do not directly communicate with each other.

The PRS monitors the position of the jaws through the up to seven sensors installed on each collimator at a survey rate of 100 Hz. Such a high rate is necessary to assure that the relative position of two jaws in different collimators remains unchanged during the execution of a movement function within a tolerance of 20 μm.

The reading from the PRS, once each position sensor has been properly calibrated, is precise to within some micrometers at normal pressure and temperature, even with cable lengths up to 800 m. In addition, the sensors themselves have been designed to withstand the nuclear radiation coming from the interaction between the beam and the jaws and to have a negligible thermal sensitivity.

1.3.4. Collimator Instrumentation

The collimators are equipped with sophisticated instrumentation which will provide extensive diagnostics. The main diagnostics information is [14, 16, 17]:

- Position of each motor and jaw support point.
- Independent measurement of collimator gap at both extremities of collimator tank (average gap and angle between the two jaws measured by 2 linear position sensors).
- Independent measurement of one jaw position at both extremities of collimator tank and measurement of the vertical tilt (5 position sensors installed for this purpose, bringing to 7 the total number of linear position sensor per collimator).
- Temperature of each graphite jaw at both of its extremities (start and end).
- Temperature of cooling water at inlet and outlet.
- Beam-induced shock waves (one microphonic sensor per jaw).
- Flow of cooling water.

The extensive diagnostics will allow fail-safe setting of collimator gaps, important checks on self-consistency and detection of abnormal beam load conditions.

Chapter 2

Linear Position Sensing in Harsh Environments

Abstract

In this chapter, a state-of-the-art review of the available linear position sensing techniques is made, with special attention on the ones suitable for harsh environments. The operational specifications are given taking as case study the application of linear position sensors for the LHC Collimators at CERN. The Linear Variable Differential Transformer (LVDT), which is the most promising solution, will be then introduced and its advantages and drawbacks presented. In particular, the problem of the magnetic interference will be addressed and in the final part possible solutions, explicitly designed for this sensor, are also advanced.

2.1. Preliminary State of the Art

2.1.1. Harsh Environment Specifications

The "harsh environment" condition for a linear position sensor (and, more in general, for any engineering device) generally refers to a set of particularly restricting specifications given by the singular operational situation in which the sensor is intended to work. This can include particularly noisy installations (e.g. presence of long cables, electromagnetic interferences, low Signal-to-Noise ratio), severe stress due to temperature changes (e.g. presence of intense heat sources or loads), nuclear radiations (e.g. installations next to radiating devices). Usually, these conditions reflect into a set of strict requirements for the linear position sensor. Together with the desired performances (in terms of uncertainty, linearity etc.), they establish the list of operational specifications, which is evidently application-specific.

The operational conditions here considered for a linear position sensor refer to the case study of the collimators of the CERN's Large Hadron Collider, already presented in Chapter 1. They involve the presence of severe nuclear radiation (due to the presence of the particle beam and its interaction with the matter) and interfering magnetic field coming from nearby devices (such as current cables and electric motors). The specifications associated to the applications can be then listed as follows [15]:

- *Uncertainty*: under ± 10 micrometers.
- *Lifetime and Robustness*: the sensor should be in place for at least 10 years and be operational without maintenance.
- *Radiation Hardness*: the position measurement should not be affected by nuclear radiations (i.e. the sensor should be *rad-hard*). For this application, the sensor has to withstand integrated doses of more than 10 Mgy[3] over 10 years. In addition, no conditioning electronics can be placed next to it (it is placed hundreds of meters away instead) [14].

[3] The Gray is the SI derived unit of absorbed radiation dose coming from ionizing radiation (e.g. X-rays), and is defined as the absorption of one joule of ionizing radiation by one kilogram of matter [2].

- *Magnetic Field Immunity*: the sensor's position measurements should not be perturbed by external DC/slowly varying magnetic fields coming from surrounding devices. This is the case, for example, of current cables feeding the normal-conducting magnets of the accelerators complex. They can give rise to DC magnetic flux density of 1 mT in air.
- *Cost efficiency*: the solution should be attractive from the point of view of the cost, for its actual implementation.

The state-of-the-art investigation on possible solutions is then referred to this requirements set.

2.1.2. Review of position sensing techniques

Among all the linear position sensing principles, a first selection has been done by eliminating those whose uncertainty does not meet the requirements. All contact-type linear position sensors (e.g. resistive sensors, depicted in Figure 2.1, which make use of a variable resistance with a sliding contact in order to measure the linear position [18]) are not suited for the requirements, because of their relatively high uncertainty and low robustness [18].

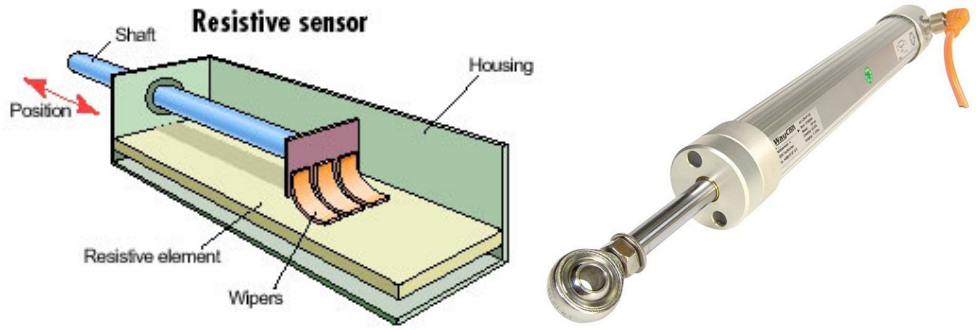

Figure 2.1. Working principle (left) and example (right) of a resistive position sensor. Source: MachineDesign.com and WayCon.de

As a matter of fact, contact-type sensors suffer from performances degradation over time, due to the wear of the resistive element, leading to erratic output signals and unreliability, as illustrated in Figure 2.2.

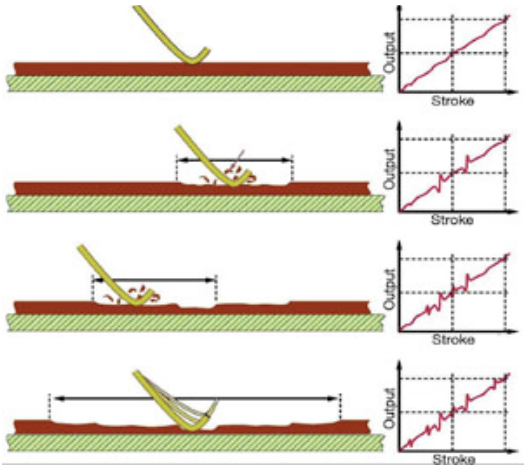

Figure 2.2. Wear effect on the resistive element of a resistive linear position sensor. Source: Balluff.com

Capacitive linear position sensors (Figure 2.3) sense the variation of an electrical capacitance, due to the object movement, in order to measure its position, as illustrated in [19], with good

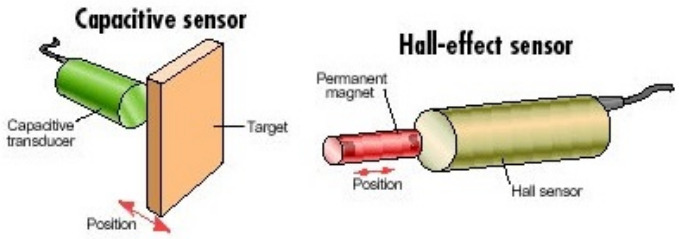

Figure 2.3. Illustration of the working principle of capacitive (left) and hall-effect (right) linear position sensors. Source: MachineDesign.com

uncertainty performances [20] and non-contact sensing [19], which leads to rather long lifetime. Nevertheless, such sensors have been tested in ionizing radiation environments, and influences on their functioning are reported [21-23]. In particular, the radiation-induced charge is accumulated on the capacitor's plates and provokes a voltage variation in the sensor (which operates at constant electric field) [21].

Position sensors based on the Hall Effect are widely used in automotive and industrial products [24] in order to measure the linear position with good uncertainty, through properly arranged permanent magnet and sensitive element [25]. The change of magnetic field produced by the movement of the permanent magnet modulates the Hall voltage which is collected on the Hall element [24], as depicted in Figure 2.3. This type of sensor cannot be used in radioactive environment for different reasons. First of all, having a small-amplitude voltage output, an amplifier should be used in place [25]. Nevertheless, it is widely known that the electronics does not withstand the nuclear radiation dose (or fluence, according to the radiation type) [26]. For this reason, generally, all sensors which involve in-place electronic and/or optoelectronic components (e.g. optical encoders) have to be discarded as well. Secondly, to assure better sensitivity, the Hall element should be made of semiconductor material, which on turn is sensitive to nuclear radiation (the effects of radiations on all semiconductors types and on electronic devices is detailed in [26]). Finally, the Hall element being sensitive to magnetic fields, the immunity to external magnetic fields is to be verified according to the sensor's geometry.

A promising technique which assures very low-uncertainty measurements relies on a fiber-based Fabry-Perot interferometer structure [27, 28]. Through a phase/frequency shift measurement between two signals coming from the interferometer, commercial sensors based on this principle can reach uncertainty of 0.5 ppm [29] even in presence of electromagnetic interference [18]. Nevertheless, since nuclear radiations have been demonstrated to affect the performances of optical fibers and related optical components [26, 30-32], the measurement uncertainty and

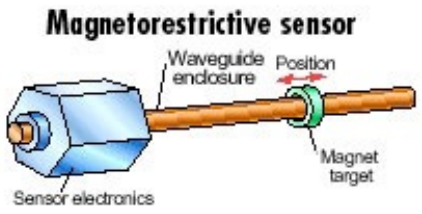

Figure 2.4. Illustration of the working principle of magnetostrictive sensors. Source: MachineDesign.com

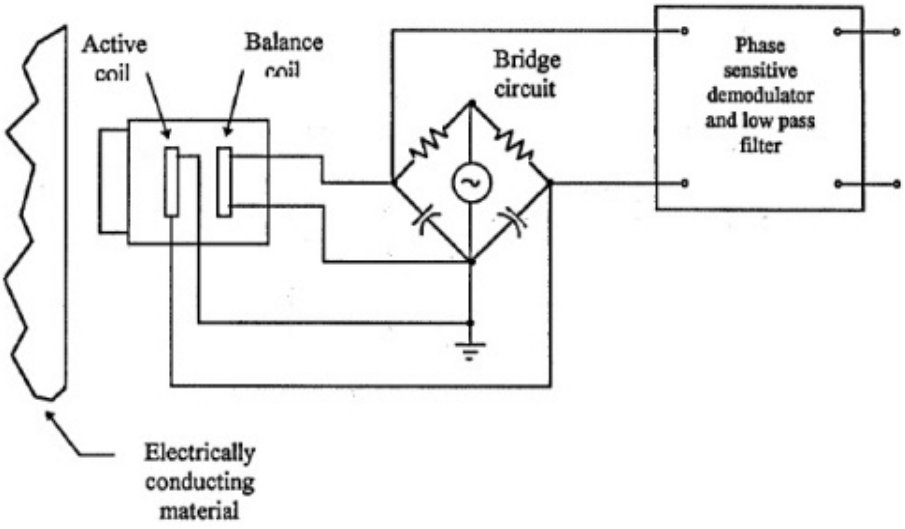

Figure 2.5. Arrangement and reading of an eddy current linear position sensor (Source: ref. [34]).

reliability in radioactive environment in this case have still to be verified. In addition, good-uncertainty fiber-based interferometric sensors often are rather expensive, compared to the other solutions discussed.

Magnetostrictive position sensors are contactless and have essentially infinite resolution [24]. The magnetostriction (i.e. the property of a ferromagnetic material to change size or shape when subject to a magnetic field) is triggered in a probe by a permanent magnet, as illustrated in Figure 2.4. The magnetic field provokes a torsional force in the probe (Weidemann Effect). The torsional pulse travels as a sonic wave along the probe, which acts as a ferromagnetic waveguide, and the corresponding elapsed time to the pick-up element gives the position reading. These sensors requires pick-up devices (i.e. electronics) integrated in the sensor [33] and can be sensitive to external magnetic fields.

Magnetoresistive position sensors make use of the dependence of electrical resistance on the applied magnetic field, when the magnetization is perpendicular to the current flow [33]. The magnetic field can be generated by a moving permanent magnet and the sensing element material can be engineered so as to have good sensitivity (e.g. fabrication on different layers, different levels of magnetoresistance etc.). Nevertheless, these sensors are not often used as position sensor because of cost and fabrication constraints [33]. In addition, they do not give sufficiently good uncertainty for the specified requirements [24].

Inductance variation sensors sense the reluctance variation of a magnetic circuit (with a movable part) made up of ferromagnetic materials with air-gaps. Different arrangements for the magnetic circuits are available [34], but these sensors cannot guarantee the required uncertainty stated above. A particular case of inductive sensor is the eddy current position sensor (see Figure 2.5), which generates a magnetic field with an active coil. The magnetic field of the eddy currents produced in a movable conducting plate is a function of the relative position of the plate. The balance coil serves to complete the bridge circuit, whereas the voltage output is given by a properly-designed demodulator [34]. Nevertheless, the eddy current sensors, and in general all inductive position sensors, can be seriously affected by an external magnetic field [34].

2.2. The Linear Variable Differential Transformer (LVDT)

2.2.1. The sensor's properties

Probably the most promising solution for linear position sensing in the harsh environment conditions listed in Section 2.1 is the Linear Variable Differential Transformer (LVDT).

The Linear Variable Differential Transformer is contactless (i.e. has very long lifetime), absolute-reading, and has essentially infinite resolution. Furthermore, since it can be hermetically sealed, it provides particular robustness [35]. In addition, it can be set up to be radiation-hard with proper insulation layers made of Kapton [36] (performances of Kapton polyimide in radiation environments can be found in [37]). The use of Kapton, together with other special insulation and sealing materials, enables the sensor to be radiation-hard even up to relevant dose levels (in [36], the radiation hardness is tested up to 50 MGy). Practical Linear Variable Differential Transformers can be designed with a non-linearity of less than 0.2% and full-scale ranges from less than 1 to over 100 millimeters [24].

The conditioning electronics can in principle be placed away from the sensor; in this case, the distance (so the cable length) depends on the application and can reach several hundreds of meters. Special reading algorithms have been implemented in order to achieve good reading uncertainty even with such cable lengths: the Sine-fit algorithm, combined with a ratiometric [38] reading technique, allows reaching an uncertainty of a few micrometers [39]. The ratiometric reading technique also allows performing temperature-independent and primary-variation-independent position reading [38]. Finally, given the simple geometry and the relatively straight-forward manufacturing, the LVDT is also a rather cost-effective solution.

Popular applications include industrial machinery, such as metal forming machines and in-process dimensional verification, as well as automotive and commercial products [35]. Usually, LVDTs require a set of driving and conditioning electronic circuits.

2.2.2. The structure and the working principle

A basic LVDT consists of a primary coil, two secondary coils, and a movable core (Figure 2.6). The

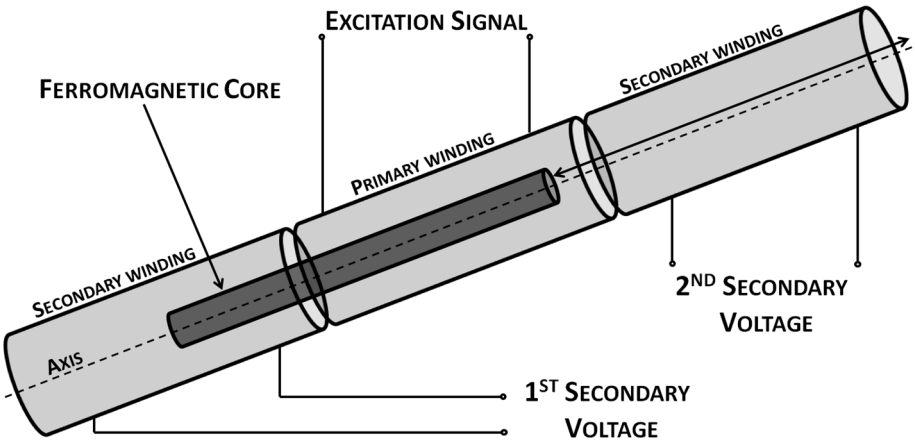

Figure 2.6. Structure and working principle of a Linear Variable Differential Transformer.

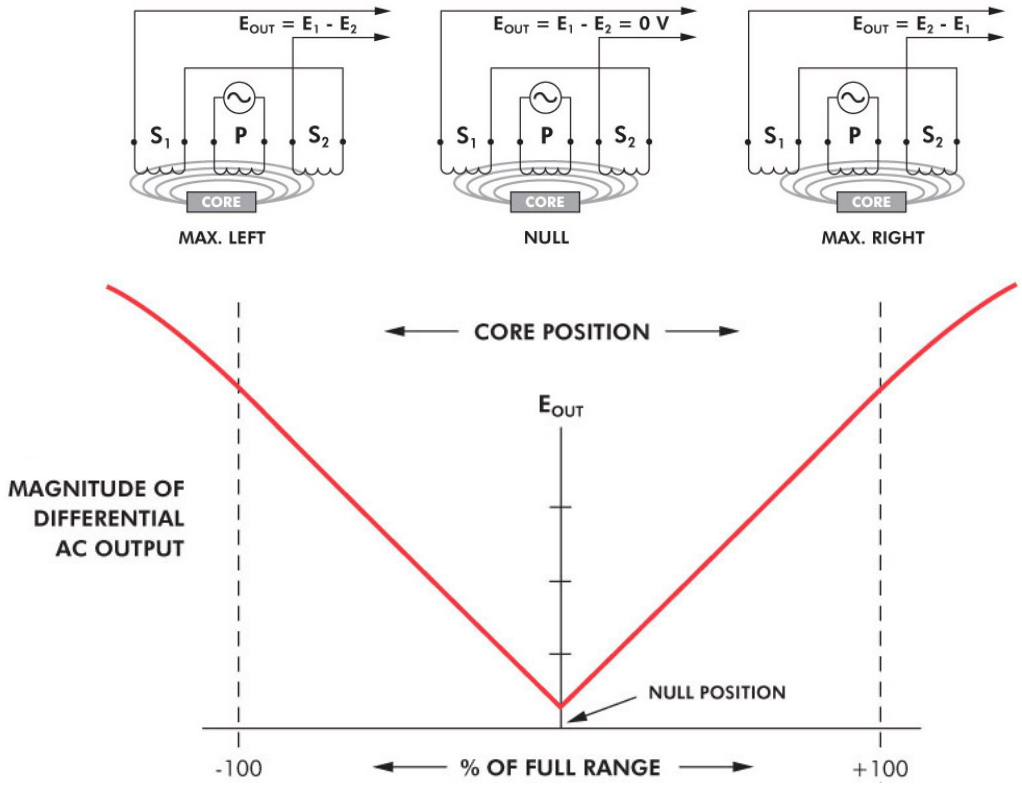

Figure 2.7. Typical curve showing the absolute value of the difference between the secondary voltages of a Linear Variable Differential Transformer as a function of the core position. Source: MacroSensors.com

coils are wound onto a tubular bobbin form, the interior of which forms the bore. In reality, such coils are inter-penetrated rather than put side by side, in order to reduce as much as possible the dispersion reactance. Electromagnetic link between the moving and the stationary parts of the sensor is achieved by means of inductive coupling. Therefore, any number of position changes can be made with theoretically infinite resolution[4], without incurring wear to the transducer parts [24].

An LVDT core is normally a cylinder of magnetically permeable material (usually in Ni-Fe alloy, commonly used for these purposes [40, 41]) and provides inductive coupling between the primary coil and the secondary coils. Before installing the core in the device, it is usually subject to an annealing process, in order to increase the permeability and make it more uniform [42]. The primary winding can be energized both with a current [43] or voltage signal [44, 45]. As the core moves along within the bore, one of the two secondary voltages increases, whereas the other decreases, due to the different mutual inductance with the primary winding. By a differential reading of these two voltages, the distance from the center between secondaries to the center of the core (i.e. the displacement of the movable core) can be extracted. When the distance from the center of the core to the center between the secondaries is zero, the core is approximately in the position known as the null. The exact position of the null point is where the two secondary voltages are equal. In principle, this should ideally coincide with the geometrical center-point of the sensor, in the case when all the windings have been wound in a perfectly symmetrical way. An example of such a

[4] The concept of "infinite resolution" used from now on merely refers to the possibility of the moving part to displace continuously, without a minimum step value *a priori*. As a matter of fact, the transducer will always be characterized by a finite resolution, taking into account the conditioning electronics or the resolution of the positioning system which controls the movable part.

behaviour is plotted in Figure 2.7, where the modulus of the difference of the secondary voltages, E_{OUT}, is depicted as a function of the position. It is also evident how the dependence on the core position becomes less and less linear as the core goes outside the designed position range.

The housing of the sensor is used to enclose the entire structure and to provide a first magnetic shielding of the coils. For this reason, a permeable material is used, such as nickel-plated steel [24]. This magnetic shield is completed by using two circular end-plates and it helps avoiding or reducing interference effects from nearby electromagnetic fields.

The LVDT is generally used either in a 4-wire or in a 5-wire configuration. In the 4-wire configuration the signal at the output terminals is the difference of the secondary voltages. The 4-wire LVDT does not have a center tap available. The 5-wire configuration includes an additional wire which represents the connection point (center tap) for both secondary windings, allowing the individual measurement of the voltage at each secondary winding with respect to the center tap [33].

The secondary voltages amplitude can be computed with several techniques [44, 46]. One of them consists in multiplying the secondary voltage sinusoid *y(t)* with a synchronous carrier *s(t)* and then applying a low-pass filter

$$[y(t)\cdot s(t)]_{LP} = [A(x)\cdot cos(2\pi f_0 t+\varphi)\cdot cos(2\pi f_0 t)]_{LP} = \\ = \left[A(x)\cdot\frac{cos\,\varphi}{2} + A(x)\frac{cos(2\pi\cdot 2f_0 t+\varphi)}{2}\right]_{LP} = A(x)\cdot\frac{cos\,\varphi}{2} \qquad (2.1)$$

Therefore, the position reading in this case depends on the phase difference, which on turn depends on the cable length used to drive the sensor. A manual tuning is then needed to compensate the phase error [39].

2.2.3. The Linear Variable Differential Transformer in the LHC Collimators

Thanks to its excellent performances, the Linear Variable Differential Transformer has been the

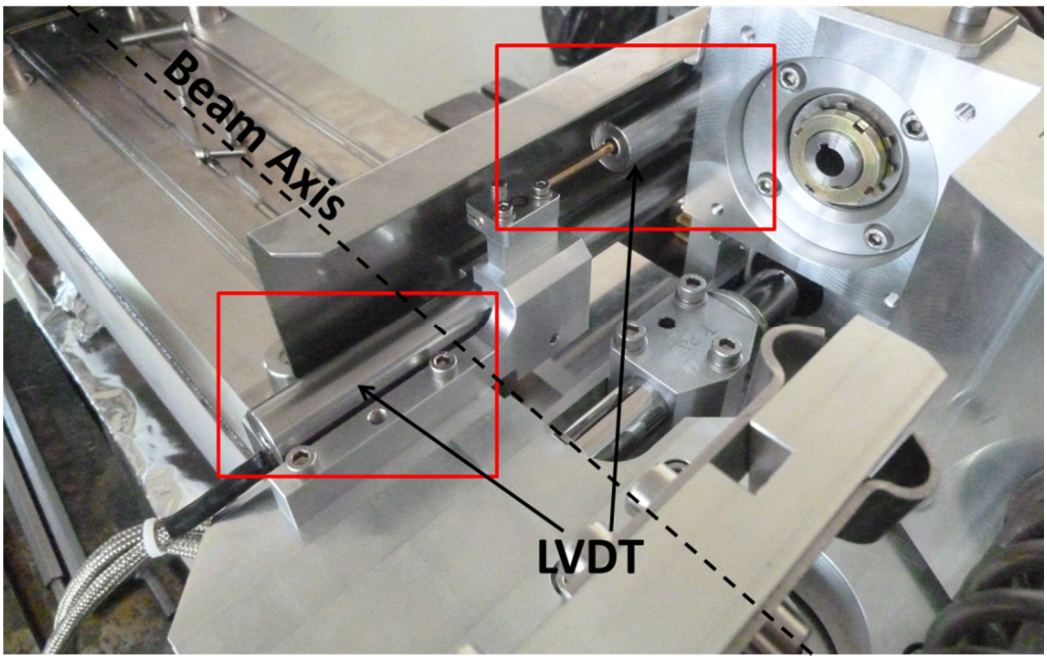

Figure 2.8. Installation of two Linear Variable Differential Transformers in a LHC Collimator test prototype. Source: CERN.

choice for the linear position sensor installed on the LHC collimators [14, 15, 47]. In particular, the LVDT sensors are used to monitor the position of the graphite jaws of each collimator (refer to Chapter 1 for the LHC collimation system), which are actually the elements that physically touch the beam during the collimation. Each collimator presents 7 LVDTs to monitor the position of the 2 graphite jaws, their difference, and the vertical tilt [15]. Therefore, 749 LVDTs are installed in the LHC. A picture of the installation of two LVDTs in a LHC collimator is shown in Figure 2.8.

However, to achieve the uncertainty performances requested by the application, a custom-made reading algorithm has been designed in order to process the LVDT output signals, based on the three-parameter Sine-Fit algorithm [39]. In practice, the amplitude of the sinusoidal signals coming from the two secondary windings of the sensor has to be evaluated, in order to allow the extraction of the core position. To do this, the signals are acquired with a sampling frequency of 250 kS/s for 2000 samples. Usually, the working frequency of the LVDTs used in the LHC collimators is around 2 kHz, so this corresponds to an acquisition of 16 periods (i.e. 8 ms). To demodulate the acquired signal, the three-parameter Sine-Fit algorithm is used, which acts as an asynchronous demodulation. This is preferred to normal demodulation procedures, since it does not suffer from the phase error.

The Sine-Fit algorithm estimates the amplitude of the voltage sinusoid by minimizing the following quantity

$$e = \sqrt{\sum_{i}^{N} [y_i - A_c\, cos(2\pi f_0 t_i) - A_s\, sin(2\pi f_0 t_i) - O_o]^2} \tag{2.2}$$

where N is the number of samples, f_0 is the working frequency, t_i is the time instant and y_i is the current sample. The estimated amplitude, offset and phase of the sinusoid are

$$\begin{gathered} A = \sqrt{A_c^2 + A_s^2} \\ \varphi = arctan(A_s/A_c) \\ O = O_o \end{gathered} \tag{2.3}$$

An alternative matrix formulation of the algorithm is proposed in [39], where the estimation reduces to the computation of the elements of two matrixes and a matrix multiplication. It has been demonstrated [39] that this algorithm is characterized by very high white noise suppression.

Actually, the three-parameter Sine-Fit algorithm performs an average of the amplitude variation of the sinusoid inside the acquired time window. Let the generic tone with variable amplitude be

$$y(t) = A(t) \cdot cos(2\pi f_0 t) \tag{2.4}$$

where the amplitude is a function of time (due to the core movement). Taking into account that $A(t)$ is varying much more slowly than the cosine part (i.e. the core does not move so fast to have components of some kHz in the amplitude signal), at the general survey time t_k^S the algorithm returns the following value [39]

$$\check{A}(t_k^S) \cong \frac{f_S}{N} \int_{t_k^S - N/f_S}^{t_k^S} A(t)dt \tag{2.5}$$

For the LHC collimators application, the cited values for number of samples, sampling frequency and working frequency have been chosen in order to assure a survey frequency (i.e. the inverse of

the time interval between two following position readings) of 100 Hz [15].

Once the two voltages have been demodulated and their amplitudes estimated, the position has to be extracted. To perform this last task, the ratiometric reading technique has been adopted [38]. The ratiometric is defined as the ratio

$$r = \frac{V_1 - V_2}{V_1 + V_2} \tag{2.6}$$

where V_1 and V_2 are the secondary voltages. The ratiometric is computed after the evaluation of the signals' amplitude. This reading technique guarantees very good uncertainty, is immune to primary excitation voltage variations and it allows a temperature-independent reading of the sensor [38]. For typical LVDTs, the relationship between ratiometric and position is linear (even with linearity errors under 0.1 % [24]), so the position can be easily measured. The proportionality coefficient between the ratiometric and the measured position is the *gain* of the sensor. Typical values of gain for LVDT sensors can be around 100.

2.3. The LVDT Magnetic Interference

2.3.1. Problem Observation

In spite of the described excellent performances and the presence of an enclosing shielding material, Linear Variable Differential Transformers have shown to be rather sensitive to external DC/slowly-varying magnetic fields. In the majority of LVDT datasheets, the possibility to have an influence on the position reading given by an external magnetic flux density is not addressed. In some of them, the user is warned about the problem, but no quantitative information is given.

In the CERN's LHC Collimators application, the magnetic interference on LVDTs has been first observed as a drift on the sensor's position reading, localized on certain sensors along the accelerators complex, especially in the transfer lines that connect the beam-lines of different circular

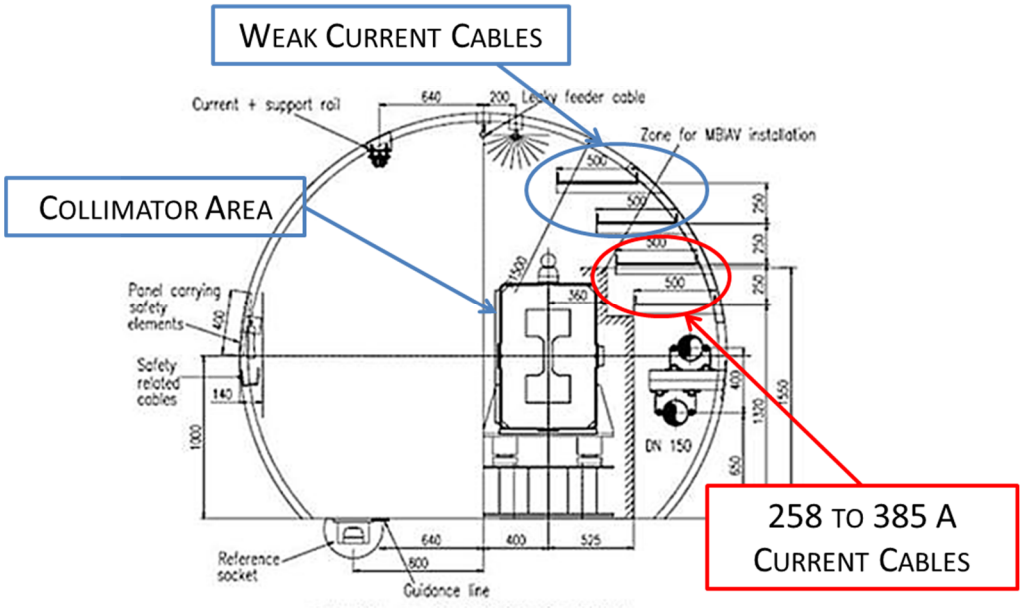

Figure 2.9. Typical cross section of a transfer line to the LHC tunnel. Source: CERN.

machines (refer to Chapter 1 for an overview on the CERN accelerators complex) [48].

Figure 2.9 shows the typical cross section of a transfer line. It is clear that not far from the collimator area (i.e. less than a meter) several current cables are placed on planes. Starting from the top, the first two ledges are equipped with cables in which the current is characterized by low peak amplitude. The other two ledges are equipped with two series of cables in which the current is constant with a superposed high-amplitude pulsed waveform. This is actually a very slowly variable signal (according to the SPS extraction cycle) with respect to the sensors and motors signals [49]. For this reason, it can be considered as a constant or DC signal. The magnitude of these current signals is of some hundreds of Amps and their function is to feed the transfer lines' magnets during their cycle modes [49].

The DC magnetic field produced by the current of these two series of cables, rather than the first two, is the main source of the magnetic interference recorded on the LVDT positioning sensors of the LHC collimators. As a matter of fact, this assertion is confirmed by the measurements which have been done on a collimator, shown in Figure 2.10. As the graphs suggest, there is strong correlation between the current signal of the cables and the position reading of one of the LVDT installed in the collimator. In fact, the two traces are perfectly synchronized. As far as the magnitude of the position drift is concerned, the same graphs show that this can reach 200 micrometers. From the specifications given in paragraph 2.1.1 regarding the position uncertainty, it is clear that this kind of drift cannot be tolerated.

However, it is important to point out that such relevant position drift occurs with relatively low magnetic field strengths. In fact, the current cables are arranged on the ledges so as to have always

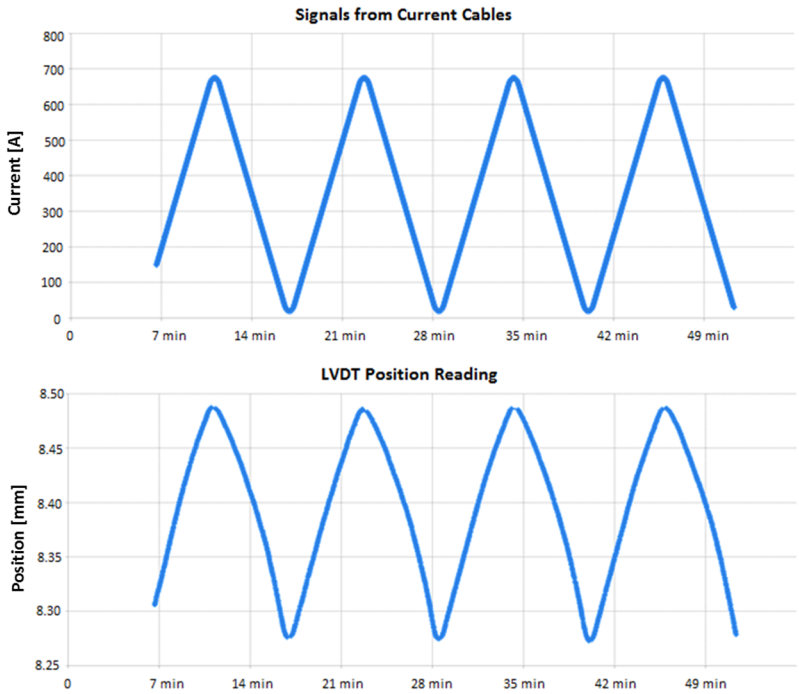

Figure 2.10. Correlation between the current signal coming from the cables (up) and the position reading of a Linear Variable Differential Transformer of a nearby collimator (down). Source: CERN.

pairs: the two cables in each pair are carrying two equal-and-opposite currents. In this condition, the magnetic field is maximal between the cables, and decreases quite rapidly with the distance from the pair. Both simulations and measurements [48, 50] have been done in order to evaluate the magnetic field strength in the tunnel. An example is depicted in Figure 2.11, where the cross section of the transfer line (i.e. collimator, cables and metal parts) has been simulated. The results of this study were that the maximum magnetic field to expect on the LVDTs placed in the collimators is around 800 A/m, which corresponds to about 1 mT in air.

Therefore, the huge position drifts which have been observed are due to a relatively low-intensity magnetic field. This points out that the LVDT sensor shows a quite sensitive behaviour to external magnetic fields.

2.3.2. The Importance of the Problem Characterization

Once the problem of magnetic interference has been demonstrated with on-the-field measurements and on-line survey of the LVDT readings, the same effect has been recreated both in finite-element simulations and in laboratory with proper equipment, in order to characterize the phenomenon.

First of all, preliminary study showed [48] that the position reading of a Linear Variable Differential Transformer is sensitive to external magnetic fields which are oriented along the axis of the sensor (i.e. longitudinal fields). On the contrary, it exhibits negligible sensitivity to transversal magnetic fields, which are more efficiently shielded by the sensor's external housing. Therefore, the cases that will be here presented refer to the circumstance where the magnetic field is longitudinal.

In addition, an analytical modelling of the phenomenon [51] showed that this kind of interference leads to unavoidable effects on the LVDT position reading. As a matter of fact, the following proportionality for the sensor's secondary voltages can be written [51]

$$V_{sec} \propto S_{sec} \cdot \mu_d(H_{DC}) \tag{2.7}$$

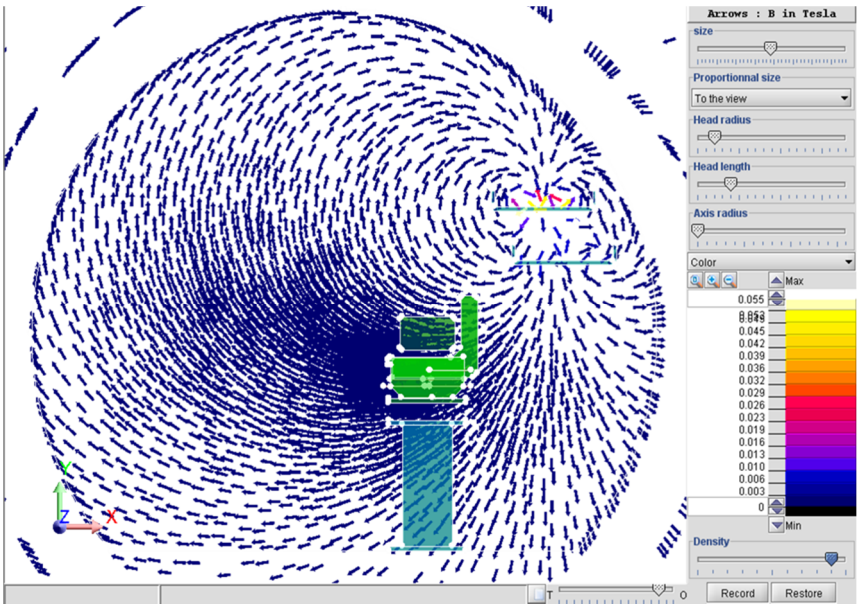

Figure 2.11. 2D Simulation of the cross section of a transfer line with a collimator and the current cables.

where S_{sec} is the transversal surface of secondary coils and μ_d is the equivalent differential permeability [52][5]. Being non-linear the magnetic materials of the sensor (i.e. the relationship between the magnetic flux density *B* and the magnetic field *H* is not linear), the interfering field H_{DC} modulates the value of the differential permeability, and so the voltage's main harmonic. The voltage change (not due to any displacement of the core) leads to a consequent position drift. This effect is unavoidable, since all magnetic materials exhibit non-linear behaviour. In addition, referring to the strict uncertainty specification listed in section 2.1.1, even a tiny modulation of the differential permeability may anyway result in an unacceptable position drift.

However, relation (2.7) and, in general, the entire analytical model of the effect do not allow any prediction on the size of the effect (i.e. the magnitude of the drift with a certain external magnetic field amplitude), since it is difficult to estimate the polarization field inside the magnetic materials. As a matter of fact, different ferromagnetic materials are used in a LVDT sensor and many of them do not constitute a closed magnetic circuit, giving rise to demagnetization fields [53].

For these reasons, the characterization of the effect by means of simulations and measurements which is here presented has to be intended as an effort to make a design tool available for quick predictions of position drift with assigned magnetic fields, parameters testing and dimensioning, in the framework of a possible design of LVDTs in magnetic environments.

2.3.3. The Finite-Element Model

To build the finite-element model of the sensor, the simulation software FLUX® has been used. It uses the finite element method [54] to solve the Maxwell's equations for both 2-dimensional and 3-dimensional structures. Given the cylindrical symmetry of the sensor's geometry and given that the interference field will be always longitudinal (i.e. cylindrical symmetry of the field distribution), the finite-element model has been built in the 2D environment, imposing symmetry around the sensor's longitudinal axis. This leads also to considerable gain in term of computational time.

The simulation geometry is depicted in Figure 2.12. The Linear Variable Differential Transformer structure has been simulated together with an enclosing solenoid, which is used to generate the external longitudinal field. As boundary condition, an infinite box has been used. The infinite box is a simulation tool used to simulate infinite space (e.g. for open problems), in which a geometrical transformation is performed to translate the infinite bounds into a finite region [55].

Figure 2.12 also shows a zoom of the simulated LVDT section. The different physical regions of the sensor (magnetic core, housing, coils, filler etc.) and their arrangement in the geometry have been first defined as simple geometrical surfaces, then physical properties have been added to define their role in the Maxwell's equation solving process. In particular, the magnetic core has been defined as a conducting element and its resistivity has been specified. In addition, to add the ferromagnetic property, the normal B-H curve has been set. The same procedure has been repeated for defining the regions of the external housing (in ferromagnetic steel). The winding regions are defined as coil conductors and are usually linked to an external electrical circuit (to perform the

[5] The differential permeability is defined as the derivative of the magnetic flux density with respect to the magnetic field strength. It is actually the slope of the BH curve.

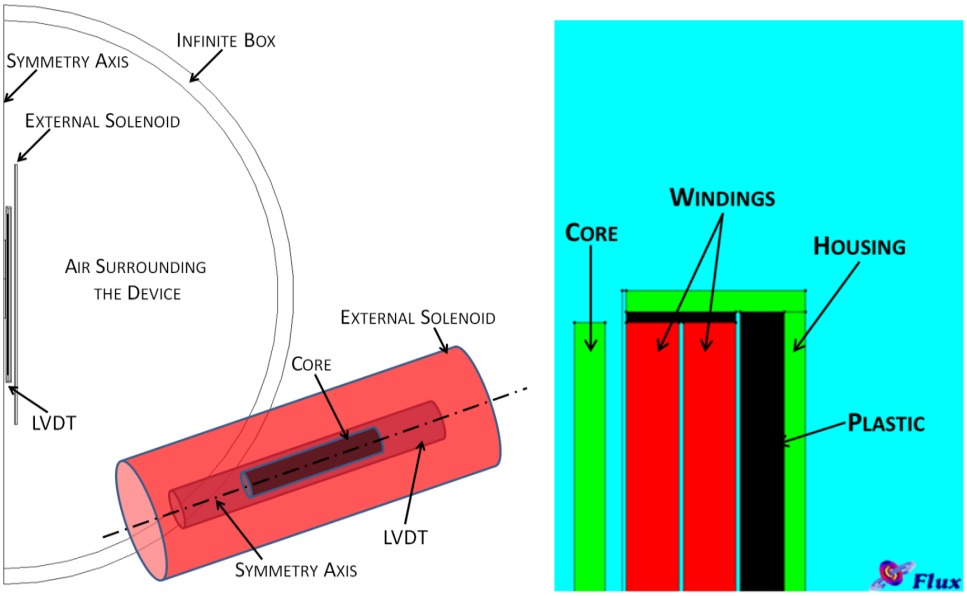

Figure 2.12. 2D Simulation structure of a LVDT inside a solenoid and 3D reconstruction (left). Particular of the LVDT structure with highlighted physical regions.

supply). For these regions, the number of turns is the only parameter to define. Regarding the coils specifications, a number of turns of 1500 has been chosen for the primary winding, in order to have a sufficiently high field inside the sensor, whereas a number of turns of 1600 has been chosen for both secondary coils, setting the transformation ratio. All other regions which are in principle not conductive and non-magnetic have been modelled as air regions. In Table 2.1 the values of all electrical, magnetic and dimensional parameters are listed. In particular, the values of relative permeability and saturation flux density refers to the actual values of two materials, the PERMENORM magnetic alloy and the 416 grade steel, which have been taken as reference materials for the core and the housing respectively. The values come from magnetic measurements performed by the materials' suppliers on annealed samples.

The structure has a high aspect ratio, thus a fine mesh has been chosen in order to discretize the

Parameter	Value
Maximum Relative Permeability of Core Material	20000
Saturation Flux Density of Core Material	1.54 T
Maximum Relative Permeability of Housing Material	800
Saturation Flux Density of Housing Material	1.72 T
Number of Turns of Primary Winding	1500
Number of Turns of Secondary Winding	1600
Core Length	100 mm
Core Diameter	5 mm
Total Sensor's Length	230 mm
Sensor's Maximum Diameter	20 mm

Table 2.1. Electrical, magnetic and geometric properties of the simulated LVDT structure.

thicknesses, whereas the mesh along the length of the sensor can be coarser. By doing so, the mesh has been optimized using triangular elements on all the geometry. The meshing and the solving parameters for the geometry are reported in Table 2.2. The presence of a small amount of poor elements (i.e. nearly flat triangular elements), disposed axially, is not a concern; indeed in such a structure the variation of the fields in a single region is supposed to be more rapid in the transversal direction, rather than in the longitudinal one [56].

This assumption applies also to the regions of the structure between the coils and the external case, in which the poor elements are present. In addition, in the regions corresponding to the magnetic media, the mesh density has been adapted to the penetration depth. Being the magnetic permeability a function of the magnetic field, the penetration depth has been calculated in the worst case (i.e. maximum permeability) and the meshing density arranged so as to have at least two meshing elements inside the skin depth area [55].

Geometrical distances, including crucial parameters (e.g. the core displacement) have been parameterized in order to allow rapid parametric simulations embedded in the same simulation scenario. The time transient solver has been chosen for the simulations, since the problem involves both harmonic magnitudes (the fields generated and coupled with the sensor's coils) and constant fields (coming from the solenoid). The Newton-Raphson method is used for non-linear solving. The numerical transients have been avoided by using an initialization by static computation [55]. On the other hand, for each simulation, an adequate time window has been chosen for the time transient computation, in order to avoid physical transient phenomena.

The parameterization of the core displacement allows performing a set of simulations at different core positions. For each of them, the geometry is re-meshed and the time transient computation performed. The core position range which has been set goes from -20 mm to 20 mm in 11 steps with constant spacing. By doing so, the simulation in standard working conditions results in the sensor's calibration.

For the interfering field simulation, taking critical installations as an example [15], the case of a 1 mT external magnetic flux density has been considered. The magnetic field is axially oriented and

Info	Parameters
Mesh Type	2D Triangular Mesh
Mesh Order and Density	2nd Order, Non-uniform
Number of Meshing Elements in the Skin Depth	3-4
Number of Poor Elements	2.8 %
Number of Nodes	About 43000
Solving Scenario	Time Transient
Target relative epsilon of the Newton-Raphson solver	10^{-4}
Maximum Number of Iterations	100
Solving time (simple computation: no parameters except time)	24 minutes

Table 2.2. Meshing information of the simulation geometry.

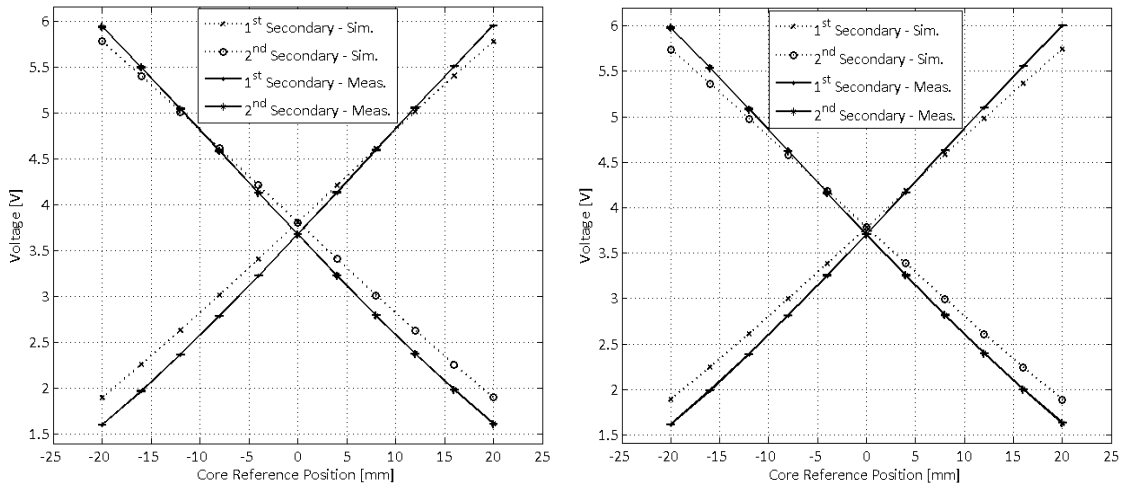

Figure 2.13. Simulations and Measurements results regarding the LVDT secondary characteristic curve (Left: voltage supply; Right: current supply). The measurement data are depicted with the corresponding uncertainty error bars.

spatially uniform. The entire simulation analysis has been performed both with a current and a voltage as supply signals.

2.3.4. Simulation Results

Although the two supply modes (voltage and current) are both used in commercial LVDTs, the need of studying the phenomenon with two different supplies comes from the fact that when the supply signal is a purely sinusoidal current, the overall magnetic field is sinusoidal, whereas with voltage supply the overall magnetic field is distorted due to the nonlinearity of the magnetic media. Hence, the influence of the external magnetic field can, in principle, play different roles in the two examined cases.

For each supply case, the LVDT characteristic curve, which shows the first harmonics of the secondary voltages with respect to the reference position, is shown in Figure 2.13 (dotted lines).

For voltage supply, the primary has been fed by a 3.5 V-peak sinusoidal voltage at 2000 Hz. It can be noticed that for both supply modes the curves have a dual behaviour in terms of trend (i.e. one decreases, the other one increases), which recalls the working principle of LVDT sensors. The curve is symmetric with respect to the null position, due to the complete symmetry of the device. The simulations show that the secondary transformation ratio of the sensor goes from 0.54 (minimum core coupling) to 1.66 (maximum core coupling). For current supply, the sensor has been fed with a current sine-wave at 2 kHz whose amplitude, 24.0 mA, has been chosen in order to have the amplitude of the first harmonic of the primary voltage of about 3.5 V when the core is in null position. By doing so, the results can directly be compared with the ones obtained with voltage supply. Again, a dual behaviour of the two curves in terms of trend and the symmetry around the null position can be noticed. In this case as well, the secondary transformation ratio of the sensor goes from 0.54 (minimum core coupling) to 1.66 (maximum core coupling).

Starting from these curves, the sensor's calibration curves have been computed as well, using ratiometric reading (see equation (2.6)). These curves show the trend of the ratiometric with respect

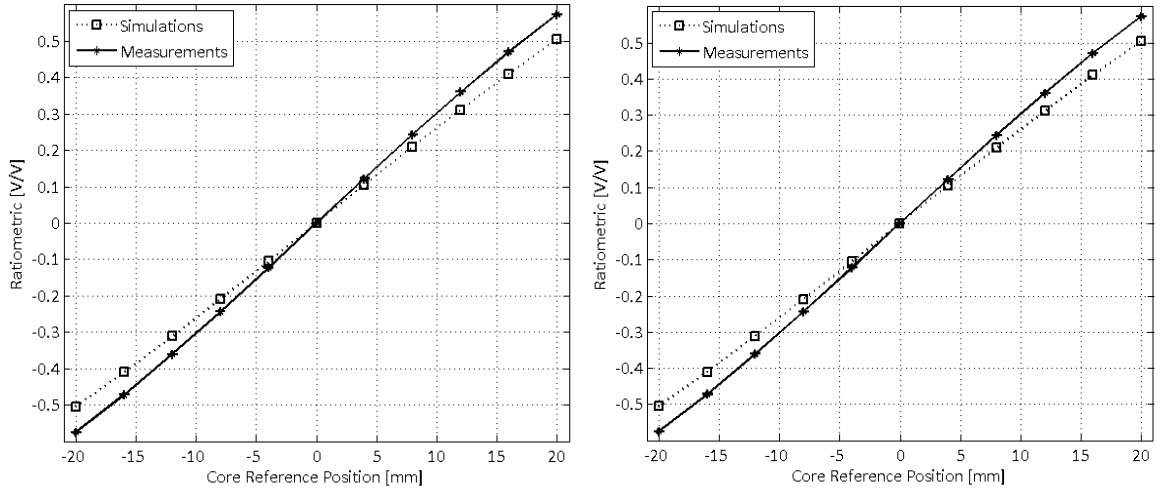

Figure 2.14. Simulations and Measurements results regarding the LVDT calibration curve (Left: voltage supply; Right: current supply). The measurement data are depicted with the corresponding uncertainty error bars.

to the core reference position. They are shown in Figure 2.14 (dotted lines). On these curves, a non-linearity error has been computed as

$$NLE = 100 \cdot \frac{max(p' - p^*)}{CPR} \tag{2.8}$$

where p^* is the core reference position, p' is the position calculated through linear interpolation of the curve, CPR is the core position range. Even if normally the core position range goes from -20 mm to 20 mm, some interesting results hold for smaller ranges too.

As from Figure 2.14, for both supplies the ratiometric is a monotonic function rising from about -0.5 to about 0.5 over the full core position range. Once again, the perfect odd symmetry of the curve reflects the perfect geometrical symmetry and reciprocity of the simulated device. With voltage supply, the non-linearity of the device resulted 0.7 % in the range [-20 mm, 20 mm]. The linearity becomes more acceptable when the core position range is reduced: nonlinearity error is 0.11 % in the range [-10 mm, +10 mm]. In current supply, these error values are roughly the same as for voltage supply.

In case of interference, since the external magnetic field yields an error on the measured position, a position drift has been computed at each core position as the difference between the position read in presence of the external interference and the position read in absence of the interference. In both cases, the position is read by means of the calibration curve obtained in standard working conditions. Actually the position drift allows performing a relative study (i.e. a study on a position variation) in order to highlight the effect of the external magnetic field on a certain position.

The results for the longitudinal interference case are displayed in Figure 2.15 (dotted line). Some interesting remarks can be pointed out by looking at these graphs. In both supply modes, the position drift is a monotonic function of the core position and it exhibits an odd symmetry (which again reflects the geometrical symmetry of the device). In addition, it is zero in the null position. The

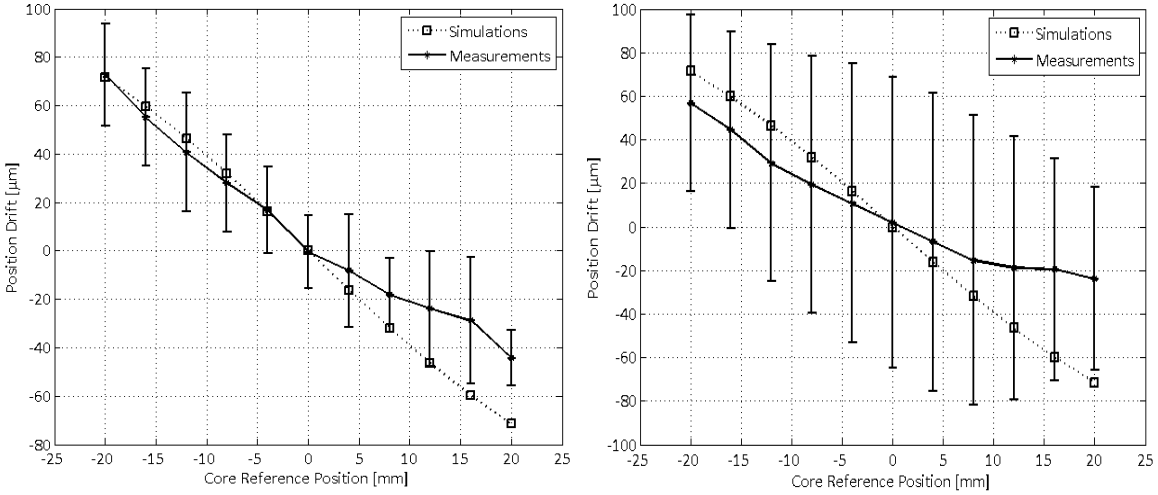

Figure 2.15. Simulations and Measurements results regarding the position drift (Left: voltage supply; Right: current supply). The measurement data are depicted with the corresponding uncertainty error bars.

farther from the center the core is, the greater the position error is. In the worst case, which occurs with current supply at 20 mm, the position drift reaches a value of about 72 micrometers.

2.3.5. The Prototype and Experimental Setup

The simulation work also constituted the starting point for a LVDT prototype manufacturing. The dimensions, materials, geometry and coils specifications reflect the simulation criteria but are not optimized, since the goal of the prototype is just to verify the FEM modelling. As already mentioned, FEM simulators model the nonlinearity of magnetic materials by considering their normal magnetization curve, therefore not taking into account major and minor hysteresis effects [55]. On the other hand, the materials which have been chosen for the magnetic parts of the LVDT sensor model had been through an annealing procedure, leading then to high permeability and narrow hysteresis cycle [57], as well as uniformly distributed magnetic permeability [42]. Therefore, the B-H curve of the actual prototype materials closely reproduces the ones used in the simulations.

The primary coil has been wound on 2 layers with a wire diameter of 0.28 mm (in order to allow possible measurements even with high currents), whereas the secondaries are single layer coils with a wire diameter of 0.06 mm, since they are supposed to be connected to high impedances, typical of Data Acquisition boards. An expanded view of the manufactured prototype, with highlighted information, is displayed in Figure 2.16.

To carry out the validation measurements, an LVDT measurement test bench has been used. The test bench has been designed to study and characterize the interference effects on Linear Variable Differential Transformers and can be additionally used to perform tests and calibrations, both on commercial sensors or custom prototypes [58]. As for the FEM analysis, the measurements have been performed with both supply modes and with the core position ranging from -20 mm to 20 mm. Anyway, considerations have been done also for reduced ranges. In particular, the measurement at different positions are preceded by an iterative research of the null point of the sensor (electric zero research) [58].

The external longitudinal magnetic field is generated by means of an external calibrated solenoid, fed by a DC current so as to have the desired amplitude and a uniform distribution for the field along the solenoid length. In addition, a demagnetization procedure has been foreseen in the measurement process [58], in order to demagnetize the magnetic circuit of the sensor and keep as fixed as possible the static working point of the equivalent B-H curve during the different measurement steps. The position drift is computed as described in the previous paragraph.

In all experimental results, the related expanded measurement uncertainty is also shown. This has been calculated on 30 repeated measurements, supposing the values spread as a Gaussian distribution in the measurement interval. A chi-squared test [59] on the repeated electric zero research results confirmed that the null point of the LVDT prototype is spread as a Gaussian distribution with a standard deviation of 6 micrometers. The uncertainty of the measurements at different positions is therefore dominated by this component, since the other sources of uncertainty coming from the test bench give much smaller values [58]. The resulting expanded measurement uncertainty has been computed using a coverage factor 2. The uncertainty on the position drift has been calculated as follows

$$u_{drift} = \sqrt{u_{p1}^2 + u_{p0}^2} \tag{2.9}$$

where u_{p1} and u_{p0} are the uncertainties on the measured position in absence and in presence of the external field, respectively.

The measurements in current supply have been performed by using a sinusoidal feeding current whose peak amplitude is 23.0 mA. This value ensures a first harmonic amplitude of the primary voltage of 3.5 V when the core is in null position. This current value is in agreement with the one coming from the simulations; thus, there is a good match between measurements and simulations regarding the primary impedance.

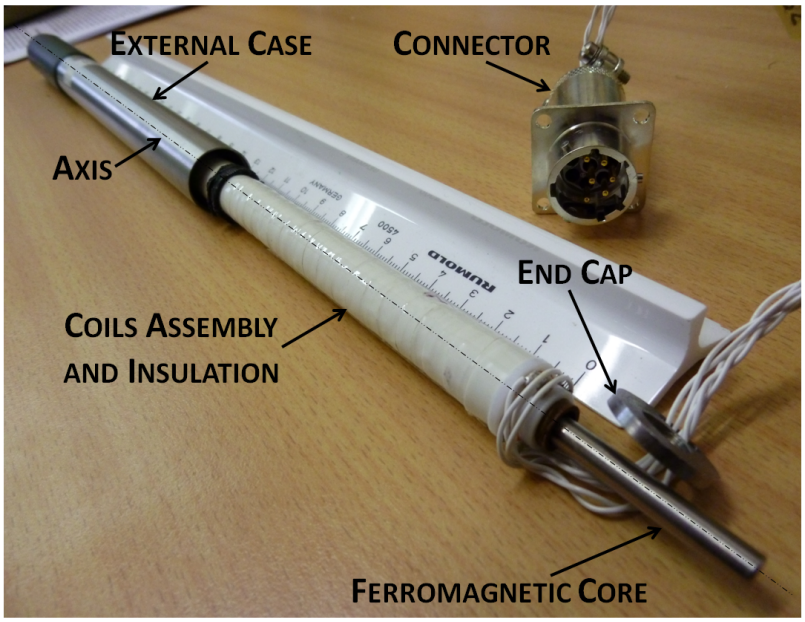

Figure 2.16. Expanded view of the custom prototype used to validate the FEM model. The comparative dimension scale is in centimeters.

2.3.6. Experimental Results

The prototype characteristic curve is depicted in Figure 2.13 (continuous line). With voltage supply, the measurements showed that the secondary transformation ratio of the sensor goes from 0.48 (against a value of 0.54 for the simulations) to 1.69 (against a value of 1.66 for the simulations). With current supply, the measured transformation ratios go from 0.48 (against a value of 0.54 for the simulations) to 1.70 (against a value of 1.66 for the simulations).

Regarding the voltage amplitudes, the agreement between simulation and measurements results with both supply signals is good, since it is always greater than 85%, whereas it increases to more than 95 % when reducing to [-10 mm, +10 mm] the core position range.

The results for the ratiometric are depicted in Figure 2.14 (continuous line). With voltage supply, the ratiometric is rising from about -0.58 (against a value of -0.5 for the simulations) to about 0.57 (against a value of 0.5 for the simulations). Measurements results show a more pronounced nonlinearity, especially for high core position ranges (1.11 % in [-20 mm, 20 mm]). With the current supply signal, the ratiometric ranges from -0.57 (against a value of 0.5 for the simulations) to 0.57 (against a value of 0.5 for the simulations). In this case, the non-linearity (calculated as in (2)) is 1.12 % in [-20 mm, 20 mm]. The ratiometric reading affects the agreement between simulations and measurements, since while the match regarding the secondary voltages is more than 85 %, the one

Item	Voltage Supply	Current Supply
Feeding Signal Amplitude	3.5 V (**3.5**)	23.0 mA (**24.0**)
Transformation Ratio	from 0.48 (**0.54**) to 1.69 (**1.66**)	from 0.48 (**0.54**) to 1.70 (**1.66**)
Ratiometric Range	from -0.58 (**-0. 50**) to 0.57 (**0.50**)	from -0.57 (**-0.5**) to 0.57 (**0.5**)
Voltage Swing (V)	4.30 (**3.90**)	4.35 (**3.90**)
Non linearity error (%)	1.11 (**0.7**) in [-20 mm, 20 mm] 0.14 (**0.11**) in [-10 mm, 10 mm]	1.12 (**0.7**) in [-20 mm, 20 mm] 0.15 (**0.11**) in [-10 mm, 10 mm]
Primary Voltage Repeatability (mV)	0.8 (no interference) 2.5 (with interference)	1.5 (no interference) 8 (with interference)
Secondary Voltage Repeatability (mV)	1.6 (no interference) 2.9 (with interference)	2.1 (no interference) 8.8 (with interference)
Measured Position Uncertainty (micrometers)	11 (no interference) 15 (with interference)	13 (no interference) 52 (with interference)
Position Drift Values (micrometers)	from 71 (**72**) to -44 (**-72**)	from 58 (**72**) to -25 (**-72**)
Position Drift Uncertainty (micrometers)	19	55
Agreement with Simulations (Characteristic Curve) (%)	>85 in [-20 mm, 20 mm] >95 in [-10 mm, 10 mm]	>86 in [-20 mm, 20 mm] >92 in [-10 mm, 10 mm]
Agreement with Simulations (Ratiometric) (%)	>83	>84

Table 2.3. Summary of experimental and simulation results.

regarding the ratiometric is lower by a few percentage points for both supply cases. Furthermore, such effect does not act uniformly on all the positions.

For a fast and complete comparison between experimental and simulation results, see Table 2.3. In this table, the numerical results regarding the measurements in the different supply cases are summarized and compared with the corresponding values obtained with the FEM simulations, reported in brackets and expressed in the same measurement units.

Regarding the interference conditions, the related position drift is presented in Figure 2.15 (continuous line). Some remarks on this figure have to be pointed out briefly. First of all, for both supply modes the drift at 0 mm is zero in the simulations and in the measurements (mean value): this is due to the fact that when the core is in the center, the interference effect on the two secondary windings is the same, resulting in a non-perturbed ratiometric reading (i.e. the measured position is not affected and the position drift is null). In addition, it can be stated that the good agreement between simulations and measurements (the simulation values are almost always within the measurement uncertainty in Figure 2.15) gets even better when considering only negative positions. As a matter of fact, the agreement in this area is more than 90%. For positive positions, even if the simulations values are still within the measurement uncertainty, the agreement decreases. In other words, the intrinsic symmetry of the position drift which simulations have shown (Figure 2.15, dotted line) is not fully reflected by the measurements values (Figure 2.15, continuous line). In fact, for both simulations and measurements the drift is positive for negative positions, negative for positive positions and null in 0 mm, but in the measurements (e.g. for voltage supply) the drift goes from 71 micrometers (against a value of 72 micrometers for the simulations) to -44 micrometers (against a value of -72 for the simulations). Such discrepancies are due to slight (micrometer order) asymmetric wire assembly of the prototype. Anyway, the overall agreement between FEM analysis and experimental measurements regarding the position drift is good.

A remark on the measurement uncertainty has to be finally done. For voltage supply, it can be noticed that the measurement uncertainty is meanly around 20 micrometers. For current supply, it is higher. Actually, with current supply the uncertainty on the primary voltage is higher (the primary voltage is not fixed by the generator), as reported in Table 2.3, leading to a higher uncertainty on the secondary voltages and finally on the position drift.

2.3.7. The FEM model as a design tool

The scientific target of the FEM model described in this section is to make available a tool both for the study of the physical phenomenon and for the design of future Linear Variable Differential Transformers where the sensitivity to external field can be correctly taken into account from the very preliminary phase.

The possible design of a LVDT with less sensitivity to external magnetic fields could indeed benefit from considerations and results based on the FEM model here presented: for example, the simulation data can affect the improvement of the performances of a LVDT by giving rapid design feedbacks regarding the choice of a certain material for the core or for an external magnetic shield, or allowing a sensitivity study with different coiling specifications, magnetic field intensity and

orientation etc. Furthermore, the proposed model and its future expansion can significantly support the study (analytical or FEM-aided) of a more complex and general case of magnetic interference on Linear Variable Differential Transformers (for example, considering non-uniform and slowly varying interfering magnetic fields).

2.4. Possible Countermeasures

As an application of the previously presented finite-element model of Linear Variable Differential Transformer, a design effort has been made to conceive a possible countermeasure for the interference problem. Given the unavoidability of the phenomenon, such a solution would in principle lead to a reduction of the interference effects, but anyway not to a complete immunity. On the other hand, since the discussed numerical model does not refer to any specific LVDT sensor, the presented countermeasures are general and can also be applied as design guidelines for different applications.

2.4.1. The Design

The proportionality relation between the first harmonic of the secondary voltages and the applied external field shown in (2.7) constitutes the starting point for the design of a possible countermeasure. It is possible to show [51] that the sensitivity to external fields of the secondary voltages (i.e. the derivative of the voltage with respect to the field) around the generic polarizing field H_{DC}^0, neglecting the minor loops hysteresis, can be evaluated as follows

$$\frac{\Delta V_i^{(1)}}{\Delta H_{DC}} \approx S_{sec} \cdot 2\pi f_0 \cdot H_{ac} \frac{\Delta \mu_{d,i}^{eq}}{\Delta H_{DC}} \left(H_{DC}^0, p\right) \tag{2.10}$$

where $V_i^{(1)}$ denotes the first harmonic of the *i*-th secondary voltage (*i* = 1, 2), $\mu_{d,i}^{eq}$ is the equivalent differential permeability of the secondary circuits, that takes into account the different magnetic materials and the relative volumes, *p* is the core position, H_{ac} is the field produced by the primary at frequency f_0, H_{DC}, S_{sec} have been already introduced in (2.7). Equation (2.10) has been derived by truncating the series expansion of the secondary voltages with the magnetic field after the first term [51] and it is actually assuming that the amplitude of the field produced by the primary, H_{ac}, is purely sinusoidal. In the nominal LVDT functioning, H_{DC}^0 is null, so the sensitivity to the external field depends on the slope of the differential permeability of the different materials around the zero.

Because of the presence of different magnetic materials[6] and the demagnetization effect on the core of the sensor, a relation between the applied field produced by the primary current and the resulting fields H_{ac} and H_{DC} can be established only by means of simulations.

The first countermeasure for the magnetic interference has been designed from (2.10). Actually, the H_{DC} field can be equivalently produced applying a DC component in the primary circuit; in this case, analysing the typical shape of the B-H curve of the used soft magnetic materials [40], it is possible to choose a biasing field, H_{DC}^0, characterized by a reduced sensitivity to the ΔH_{DC} produced by the external field. Of course, applying the additional DC signal would mutate the sensor's

[6] In a Linear Variable Differential Transformer, the core and the external housing may not be the only ferromagnetic materials in the sensor's structure. As a matter of fact, the bobbin on which the coils are wound may be in ferromagnetic steel.

characteristic curves and affect its linearity [60].

The second countermeasure concerns the design of an additional magnetic shielding for the sensor. As already mentioned, commercial LVDTs can present a cylindrical shield integrated in the sensor magnetic circuit. An innovative aspect of the presented solution consists in separating the magnetic circuit of the coaxial cylindrical shield from that of the sensor. By so doing, the design of the shield can be optimized for the rejection without concerning any sensor constraint. Dimensions, materials and distances between the different shielding layers can be adjusted to achieve a given shielding efficiency, depending on the maximum acceptable position drift.

A preliminary simulation has been carried out with the described FEM model, to evaluate the effect of an interfering longitudinal magnetic field, ranging from 0 to 800 A/m (i.e. magnetic flux density ranging from 0 to 1 mT in air), on the measured position. Nevertheless, since this solution should keep broad-spectrum properties in order to be considered for all kind of Linear Variable Differential Transformers, the magnetic properties of ferromagnetic parts have been chosen looking at the curves of 50-50 Iron-Nickel alloys [40] and ferromagnetic steels [61], used as core and housing respectively. In addition, the winding bobbin has been considered as made of ferromagnetic steel, as verifiable in many sensors [24].

The simulations showed that the maximum drift on the measured position is about 1 mm, as well as that the magnetic field has to be reduced to about 35 A/m in order to have a drift not greater than 20 micrometers. Therefore, the shield has to show an attenuation factor of about 23. In a scenario in which a longitudinal interfering field of 800 A/m is considered, the field impinging the cylindrical shield has both longitudinal and transversal components, not uniformly distributed along the length (see Figure 2.17).

Since such a case cannot be handled by means of an analytical handbook approach [62], a simulation approach with a FEM software is necessary in order to design the shield, having as a basis the following guidelines: (i) use of high magnetic permeability materials to reduce the interfering fields; (ii) consideration of a multi-layer shield to prevent the saturation of the inner layer; (iii) optimization of the air gap between the layers and their thicknesses not to oversize the shield with

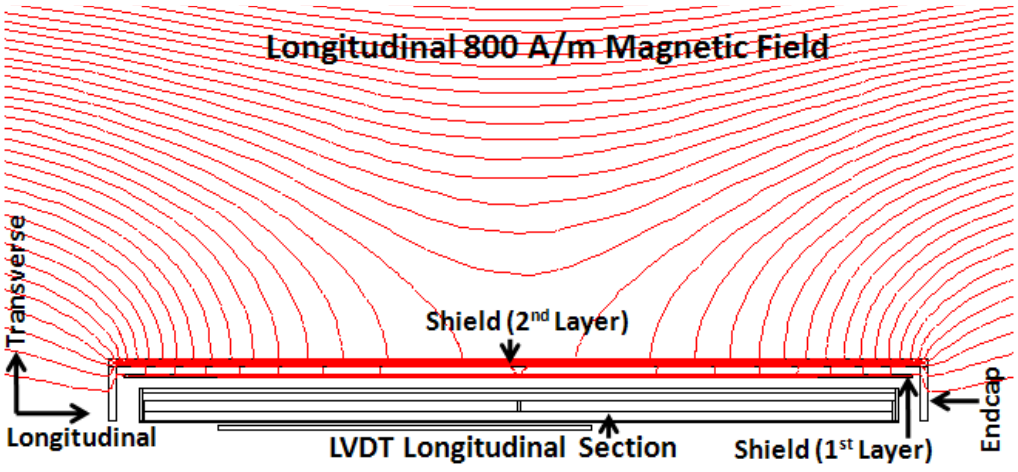

Figure 2.17. Flux density distribution in case of an external longitudinal magnetic field impinging on the LVDT shield. Only one half of the LVDT longitudinal section is displayed, being it symmetric around the axis.

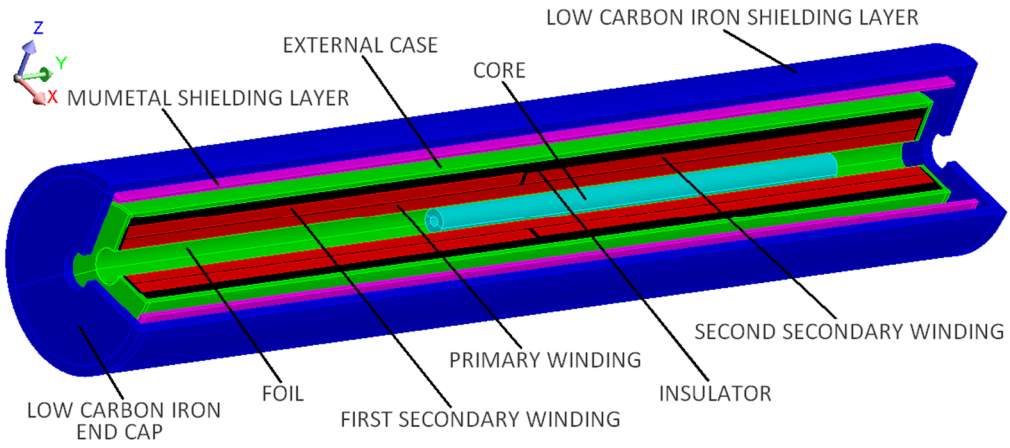

Figure 2.18. LVDT model and shield case. Half of the displayed longitudinal section has been used for 2D simulations. The iron layer exhibits a thin air gap between the cylindrical part and the caps, in order to take into account the actual physical discontinuity between the two pieces

respect to the sensor dimensions.

According to that, a single layer shield with a high permeability material, such as Mumetal [61], has been discarded since a decrease of about 50% of the permeability (from 120000 to 60000) has been observed, meaning a significant saturation. For this reason, the shield has been equipped with an external layer (Figure 2.18). The 1-mm distance between the layers it assures that the Mumetal layer does not saturate and provides an appropriate shunting effect for the flux. The external layer is a low carbon iron cylindrical foil [61], with two end caps which, in particular, assure a very effective binding of the longitudinal flux lines, avoiding a direct impact on the sensor's magnetic circuit, as shown in Figure 2.17. Consequently, additional Mumetal end caps turned out to be not necessary.

A parametric simulation showed that 1 mm of low-carbon iron and 0.4 mm of Mumetal assure both the saturation prevention and the required shield efficiency. In fact, the magnetic field impinging the LVDT results to be about 30 A/m, which should contain the drift of the measured position within 20 micrometers, which has been considered as design goal.

2.4.2. The Validation

The two described countermeasures can be used either alternatively (e.g. the DC polarization can

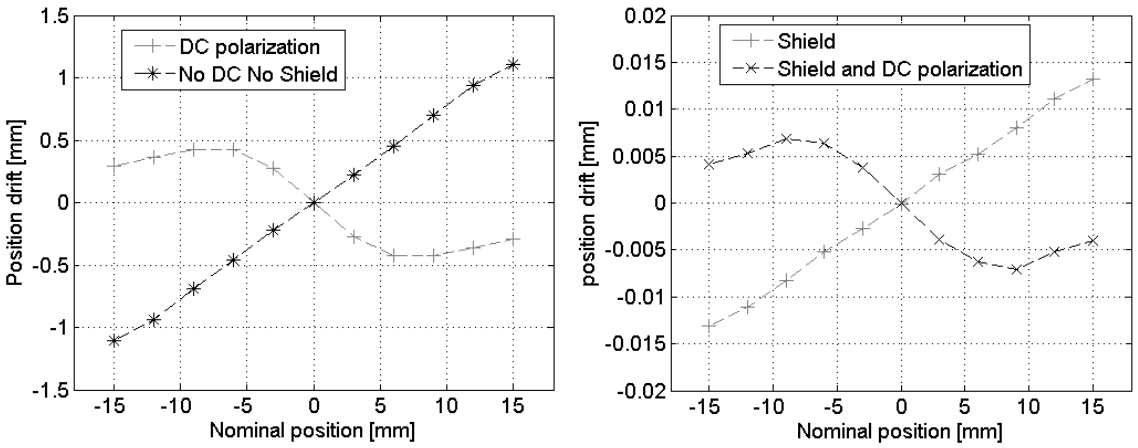

Figure 2.19. Comparison between the position drift of the LVDT model without and with the designed countermeasures.

be used for those cases where a shield is not suitable for mechanical reasons) or simultaneously.

Figure 2.19 shows the simulation results concerning the effectiveness of the proposed solutions. The primary coil is fed by a voltage generator providing a 3.5 V sine waveform at 2000 Hz. The simulations have been carried out in the test range going from -15 mm to 15 mm.

A DC voltage of 10 V has been added to the primary sine-wave input. After evaluation of the calibration curve of the sensor in presence of the DC signal, the maximum position drift due to an external interference of 800 A/m results to be reduced by a factor 2 (Figure 2.19). The inversion of the sign is due to the DC polarization which affects the characteristic curve of the sensor.

However, as main solution strategy, the external magnetic interference can be reduced by means of the shield case described above. Figure 2.19 shows that the only shield reduces the position drift to about 12 micrometers, without deeply affecting the sensor linearity.

Finally, both the shield case and the 10 V-DC polarization have been applied to the LVDT. It can be stated that the benefits of both solutions are kept since the position drift is still reduced by a factor 2 with respect to the case in which the only shield is considered.

2.4.3. The applicability

The proposed two solutions to reduce the magnetic interference on Linear Variable Differential Transformers maintain the aspect of generality, which means that they can be in principle used for existing commercial sensors. Nevertheless, there exist some reasons for which the considered countermeasures cannot find full applicability:

- The shield has been designed considering a specific interfering field. It can be re-designed for different magnetic field strengths, but it cannot be applied when the magnitude of the interfering field is not known *a priori*.
- The value of DC polarization (either a voltage or a current) significantly depends on the sensor's materials and can give different performances for different magnetic properties of the media. In addition, it can be considerably high.
- The shield design leads to physical enlargement of the sensor's overall dimensions. This may results in total unsuitability for applications where dimensional constraints are important.
- Applications where a total magnetic immunity of the position sensors is required cannot benefit from these solutions. Furthermore, they cannot be improved up to guarantee immunity, since the magnetic interference phenomenon on LVDTs depends on the non-linearity of its magnetic materials, which is always present.

Therefore, a sort of definitive countermeasure would be a solution for which all the excellent properties of Linear Variable Differential Transformers are kept, and the immunity to DC/slowly-varying external magnetic fields is added as novel key-property.

Innovative Contribution to the Chapter and Related Publications

A Linear Variable Differential Transformer numerical model has been developed using Finite Element Method software. The model has been used to study and characterize the interference effect due to external DC/slowly-varying magnetic fields on the LVDT position reading. The validation has been carried out with experimental measurements performed on a test bench. The same model has been then used to conceive two first-stage countermeasures to the interference effect: the use of a DC polarization in the primary circuit and the

design of a two-layer magnetic shielding assembly. Both solutions have shown to perform well and reduce the position drift due to the external field under a given threshold. The range of applicability of such solutions has been also discussed.

1. M. Martino, A. Danisi, R. Losito, A. Masi, G. Spiezia: "*Design of a Linear Variable Differential Transformer With High Rejection to External Interfering Magnetic Field*", IEEE Transactions on Magnetics, vol. 46, no. 2, February 2010.

2. A. Masi, A. Danisi, R. Losito, M. Martino, G. Spiezia: "*Study of Magnetic Interference on a LVDT Prototype: FEM Model and Experimental Measurements*", Journal of Sensors, Hindawi Publ. Corp., vol. 2011.

Chapter 3

The Ironless Inductive Position Sensor

Abstract

In this chapter, a novel Ironless Inductive Position Sensor is presented. In the first part, the sensor's configuration and working principle are discussed. In addition, an exhaustive comparison with the Linear Variable Differential Transformer is proposed, highlighting analogies and differences between the two sensors. The core of the chapter is dedicated to the full modelling of the sensor from the electromagnetic and thermal viewpoints. Taking the model as a basis, a novel algorithm for position reading is also presented, together with a complete optimization of the sensor's configuration.

3.1. Sensor's Physics and Properties

In Chapter 2, the unavoidability of the magnetic interference on Linear Variable Differential Transformers due to external DC/slowly-varying magnetic fields has been frequently pointed out. It has also been said that the immunity to external fields would be an interesting added-value if all the good properties of common LVDTs were kept at the same time. The Ironless Inductive Position Sensor (also abbreviated as I2PS), which is presented in this chapter, is the ideal candidate for this purpose. It is a linear position sensing device which is immune by design to external magnetic fields. In addition, being based on magnetic coupling between contactless cylindrical coils, it keeps the same advantages of Linear Variable Differential Transformers.

3.1.1. The Working Principle

In a Linear Variable Differential Transformer, the use of a ferromagnetic core is essential to let the magnetic flux coupled with two secondary coils (and so their voltages) be a function of the position. Nevertheless, as mentioned in Chapter 2, the non-linearity of the relationship between the magnetic flux density and the magnetic field of the materials enables an external field modulating the first harmonic of the coils' voltages, affecting in this way the sensor's reading.

Therefore, a sensing structure, based on inductive coupling, which creates a variable magnetic flux according to the position and, at the same time, presents always a linear relationship between magnetic field and magnetic flux density (i.e. constant differential permeability), would in principle lead to an intrinsic immunity to external fields.

The proposed sensor is shown in Figure 2.1, where its longitudinal section is depicted. It is a 5-winding structure made up of coaxial air-cored cylindrical coils. Two supply and two sense coils are stationary, whereas the moving coil constitutes the movable part of the structure.

The two supply coils have the same number of turns and are wound on the same bobbin, in order to have the same values of resistance and inductance. Nevertheless, the direction of the wiring is opposite for the two coils. They are fed by a sinusoidal signal (either current or voltage) and consequently generate two equal-and-opposite magnetic fields. Actually, the same task can be achieved either imposing opposite wiring directions or feeding the coils in counter-series so as to have equal-and-opposite currents (see Figure 3.2).

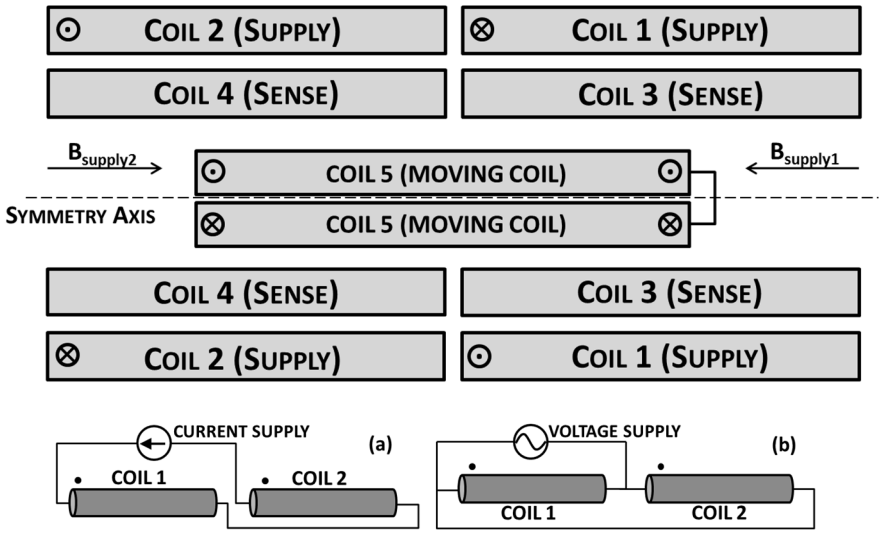

Figure 3.1. (Top) Working principle of the Ironless Inductive Position Sensor. The directions of the current density in the coils and of the flux densities generated by the supply coils are indicated. (Bottom) Example of supply scheme for (a) current and (b) voltage supply. The black dots indicate the winding direction.

As for the supply coils, the sense windings have the same number of turns, equal resistance and inductance, but they are open-circuited. The moving coil is wound on a movable plastic bobbin (i.e. non-magnetic and non-conductive). It is short-circuited, so a current will be induced in this coil. In particular, when the moving coil is at the center, its net induced current is zero, since it is the sum of the induced currents corresponding to two equal-and-opposite magnetic fields. More precisely, the mutual inductances between the moving coil and the two supply coils are equal. For these reasons, the voltages induced on the two sense coils, due to the magnetic coupling with the supply coils, are equal. Comparing the system to an electric bridge, the case in which the moving coil is at the center is the equilibrium condition. As it will be clear in the next sections, the short-circuiting of the moving coil is a necessary condition for the proper functioning of the sensor.

As the moving coil displaces from the center, the equilibrium is broken and the net current induced in the moving coil is non-null, since now the mutual inductance with one of the supply coils is higher than with the other. The non-null induced current leads to a counter-acting magnetic field, which adds up (with its sign) with the supply field. As a result, the net flux concatenated with the sense windings will be affected by the presence of the moving coil's counter-acting field. Therefore, the two sense voltages are different. The position of the moving coil can hence be extracted, as in LVDTs, by a differential reading of the fundamental harmonic of the sense voltages.

Therefore, the structure in Figure 2.1 creates a magnetic flux (on the sense voltages) which is variable with the position (of the moving coil) and, at the same time, does not use ferromagnetic materials (all the windings are air-cored). For this reason, an external DC/slowly varying magnetic field does not affect the main harmonic of the sense voltages as it does for the LVDT secondaries, since air has constant differential permeability.

As mentioned, the supply of the sensor can be either performed with a current or a voltage signal. Nevertheless, as it will be shown, the sensor's functioning is quite different in the two cases and in reality the choice of the feeding signal is an important design step. However, in both supply cases it is important to guarantee two equal-and-opposite magnetic fields generated by the supply

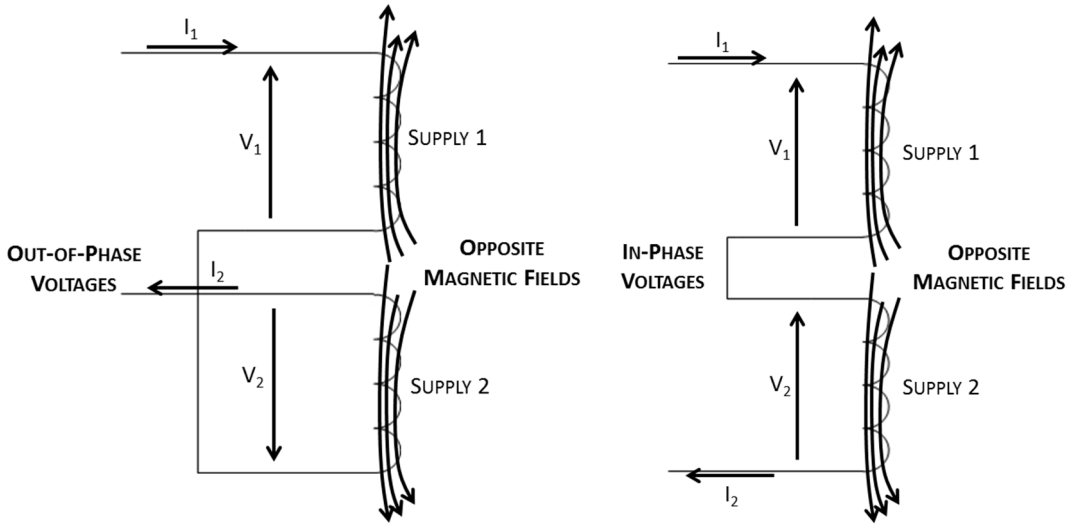

Figure 3.2. Two possible supply schemes for the Ironless Position Sensor in case of current supply. (Left) Counter-series supply with the same wiring direction for the windings. (Right) Series supply with opposite wiring direction for the windings. Both cases guarantee opposite magnetic fields.

windings. This condition improves the sensitivity of the device, since the induced current in the moving coil is a function of the net flux concatenated with it. As a matter of fact, if there was a single supply winding (instead of two), the induced current in the moving coil would generate a magnetic field which counteracts the primary one. Nevertheless, it will decrease the magnetic coupling with both sense windings; obviously, according to the position, the deterioration of the coupling will be more pronounced for one sense winding and less for the other. Therefore, there will still be a spatially-variable magnetic flux, but the sensitivity will be very low (i.e. the difference between the sense windings' voltages will be small). On the contrary, designing a two-winding supply assembly with 180-degree-out-of-phase signals, the induced current in the moving coil generates a magnetic field which decreases the magnetic coupling with one sense winding and increase it with the other. In this way, the difference between the sense voltages is maximized and the sensor exhibits a stronger sensitivity.

For the two supply windings to generate opposite magnetic fields, different arrangements of the signals and the windings can be designed. In case of voltage supply, the voltage signal can be applied with swapped electrodes to the two windings (Figure 2.1). In case of current supply, the windings can be fed in counter-series. Finally, the coils can be wound in two different wiring directions and fed in series. The difference between these solutions is in the signal's phase. As an example, with current supply (see Figure 3.2) the supply in series with opposite wiring direction for the windings gives rise to in-phase supply voltages, whereas the counter-series supply exhibits 180-degree-out-of-phase voltages. The same can be demonstrated for the currents in case of voltage supply. This point is very important in the sensor's design for its manufacturing and supply scheme.

The two sense windings present the same number of turns in order to have symmetry, but since they are directly connected to the readout system (characterized by very high impedance), their wiring direction is not important for the sensor's proper functioning. For the same reason, the assumption of null current in the sense circuits can be made. Finally, the radial order of the windings

(i.e. the supply coils are wound over the sense coils) has to be respected in order to have better coupling between supply and sense windings.

The entire sensor's structure can be housed in a cylindrical sheath, whose material can be chosen so as to have good ruggedness and robustness.

3.1.2. Comparison with the Linear Variable Differential Transformer

Some remarks have to be pointed out when comparing the Ironless Inductive Position Sensor to the Linear Variable Differential Transformer, described deeply in Chapter 2. From the geometrical viewpoint, I2PS and LVDT are similar: both are based on cylindrical coils wound on a common support bobbin.

From the physical viewpoint, in a Linear Variable Differential Transformer, the magnetically permeable core increases the coupling between the primary and secondary winding which is facing it. On the contrary, in the Ironless Inductive Position Sensor, the moving coil acts as a controlled disturbance on the inductive coupling between the supply and the sense coil which is facing. However, the goal of the two sensors is still the same (i.e. to produce a spatially variable magnetic flux). In fact, the spatial modulation of the flux enables the estimation of the position.

Furthermore, Figure 3.1 clearly shows that there is no contact between the moving coil and the fixed coil assembly. Therefore, the contactless sensing (which leads to very long lifetime of the sensor), a known key-property of the LVDTs, is maintained. In addition, as for the magnetic core of Linear Variable Differential Transformers, the moving coil can move smoothly with virtually infinite resolution inside the sensor. Thus, the sensor's resolution is only determined by its conditioning electronics. Being the coils wound on a cylindrical bobbin, the entire structure can be hermetically sealed with proper filling materials or resins, assuring a good robustness (as done for LVDTs). The wires of the coils can be insulated with polyimide and the bobbin supports for the windings can be made of appropriated plastic materials, so as to guarantee radiation hardness. Finally, proper conditioning algorithms can be chosen for the sensor's readout, so as to have position uncertainty below ± 10 micrometers (in principle, as the number of signals acquired is the same as for LVDTs, the ratiometric technique enhanced with the three-parameter Sine-Fit algorithm can be selected, as done with LVDTs).

For what has been said, the properties of contactless sensing, robustness, infinite resolution, good position uncertainty and possibility to have radiation hardness, which are typical advantages of Linear Variable Differential Transformers, are satisfied by the proposed ironless sensor. The added-value of the sensor is the immunity to external magnetic fields, which makes it a suitable choice in case of harsh magnetic environments.

The presence of such added-value underlines the difference between the two sensors regarding the materials. In a common Linear Variable Differential Transformer, many parts are made of ferromagnetic material: the movable core, the support bobbin of the coils and the external magnetic shielding. In an Ironless Inductive Position Sensor, no ferromagnetic material is used, either for the movable parts or for the fixed parts. Nevertheless, a conductive shielding (e.g. aluminium) may be designed in order to protect the sensor from environmental very high-frequency noise which can be

picked up by the coils. If the sensor is to be installed in proximity of ferromagnetic materials with very high permeability, a ferromagnetic housing can also be designed. Nevertheless, in this case the housing will not serve as a magnetic shielding, but rather for keeping the flux lines together and minimizing the leakage flux. Therefore, the specifications regarding magnetic permeability and saturation are not critical, as it is the case of LVDTs.

3.2. Low-Frequency Electromagnetic Model

The Ironless Inductive Position Sensor has been presented as a valid alternative to Linear Variable Differential Transformers. The fundamental following step is the generation of an analytical model that describes the sensor's functioning and demonstrates the variability of the flux linkage with the position and the immunity to magnetic fields. The resulting model would be a powerful tool for the sensor's analysis, study, optimization and design. Therefore, the modelling is the most important step in the whole sensor research: the additional studies regarding optimization, reading technique and prototyping rely on the soundness and consistency of the analytical models.

3.2.1. The Hypotheses

The analytical formulations presented in the following subsections aim at fully describing the functioning of the Ironless Inductive Position Sensor in its standard working conditions (i.e. without external magnetic fields) and justify the magnetic immunity. The proposed model takes into account the following hypotheses as references:

- Time transients are not considered: all the magnitudes are considered to be at their steady state.
- The signals are purely sinusoidal: as the relationship between magnetic flux density and magnetic field is linear in the air, both currents and voltages of all windings are sinusoidal, and so are magnetic fluxes. However, the model equations can also be applied to each harmonic of a multi-tone signal.
- High frequency phenomena are neglected: the high frequency phenomena which can arise in an I2PS are mainly skin, proximity effects in the coil conductors and the presence of parasitic winding capacitances. They are not considered for this model.
- Perfect cylindrical symmetry is assumed: all physical magnitudes are considered independent with respect to the azimuthal coordinate of a cylindrical system with the *z*-axis corresponding to the sensor's longitudinal axis.
- Winding imperfections are neglected: the effects of non-uniform coil density along the winding, as well as crossing wires, are neglected.

Due to the first two hypotheses, it is possible to write the equations directly in the phasors' domain. The use of phasors notation in the model leads to a much more elegant and straight-forward analytical treatment.

In the following calculations, for the sake of simplicity, the supply windings are referred to with the subscripts *1* and *2*, whereas the sense windings are referred with the subscripts *3* and *4*. The moving coil is referred to with the number *5*.

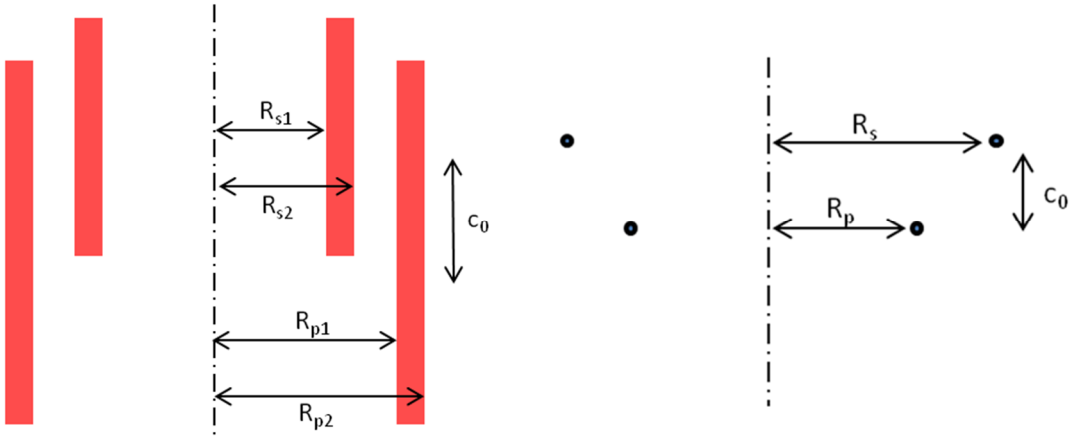

Figure 3.3. Longitudinal scheme of (left) two thick windings and (right) two simple coaxial circular coils made of circular wire. The superposition of the mutual inductance between two simple coils leads to the calculation of the mutual inductance between thick windings.

3.2.2. Computation of Mutual and Self-Inductances

The calculation of the mutual and self-inductances of the different windings is the starting point for the modelling of the Ironless Inductive Position Sensor. Starting from the specified parameters of the windings (number of turns, number of layers, length and winding section) the values of self and mutual inductances can be calculated accurately. Given the absence of magnetic materials, the mutual inductances will be a function of the windings' geometry and their relative position only (i.e. position of the moving coil, being this winding the only movable part).

The mutual inductance between the sensor's thick windings (i.e. windings with several layers) has been calculated adding up the layer-by-layer mutual inductances. The mutual inductance between two single layers of two different windings has been on turn calculated adding up the contribution of elementary mutual inductances between two circular coaxial turns, using the filament method [63-65]. The mutual inductance in the latter case can be expressed as

$$M_l = \frac{2\mu_0\sqrt{R_p R_s}}{k}\left[\left(1-\frac{k^2}{2}\right)K(k) - E(k)\right] = \mu_0\sqrt{R_p R_s}\,\phi(k) \tag{3.1}$$

where $\mu_0 = 4\pi \cdot 10^{-7}\ H/m$, R_s and R_p are the coil radii and

$$\alpha = \frac{R_s}{R_p}, \qquad \beta = \frac{c_0}{R_p}, \qquad k^2 = \frac{4\alpha}{(1+\alpha)^2+\beta^2}$$
$$\phi(k) = \left(\frac{2}{k} - k\right)K(k) - \frac{2}{k}E(k) \tag{3.2}$$

with c_0 being the distance between the turns (see Figure 3.3). K and E are the complete elliptic integrals of first and second kind respectively[7]. Therefore, letting N_{lp}, N_{ls} the number of layers of first and second winding and N_p, N_s the number of turns per layer of first and second winding respectively, the overall mutual inductance for the two coils at distance c_0 is

$$M_T(c_0) = \mu_0\sqrt{R_p R_s}\sum_{i=1}^{N_{lp}}\sum_{j=1}^{N_{ls}}\sum_{n=1}^{N_p}\sum_{l=1}^{N_s}\phi_{i,j,n,l}(k_{i,j,n,l}) \tag{3.3}$$

[7] Elliptic integrals often cannot be expressed with analytical functions. The complete elliptic integral of the first kind is defined as $K(k) = \int_0^{\pi/2}\frac{d\vartheta}{\sqrt{1-k^2 sin^2\vartheta}}$, whereas the complete elliptic integral of the second kind is defined as $E(k) = \int_0^{\pi/2}\sqrt{1-k^2 sin^2\vartheta}\ d\vartheta$. [66]

where

$$k_{i,j,n,l}^2 = \frac{4\alpha_{i,j}}{\left(1+\alpha_{i,j}\right)^2 + \beta_{i,n,l}^2} \tag{3.4}$$

and the geometrical values defined in (3.2) are function of the layer and/or of the distance between the single circular turns, as follows

$$\alpha_{i,j} = \frac{R_{s,j}}{R_{p,i}}, \qquad \beta_{i,n,l} = \frac{c_{n,l}}{R_{p,i}} \tag{3.5}$$

with

$$\begin{gathered} R_{p,i} = R_p + (i-1)\cdot d_p\,, \quad R_{s,j} = R_s + (j-1)\cdot d_s \\ c_{n,l} = c_0 + (z_n - z_l) \\ z_n = -a_p + (n-1)\cdot d_p\,, \quad z_l = -a_s + (l-1)\cdot d_s. \end{gathered} \tag{3.6}$$

In (3.6), a_p and a_s represent the semi-length of the first and second coil respectively, whereas d_s and d_p are the corresponding wire diameters. z_n and z_l are the z-coordinates corresponding to the n-th and the l-th turn of the first and second winding respectively.

In the case of mutual inductance involving the moving coil, c_0 will be proportional to the actual moving coil position and the resulting mutual inductance will also depend on this position. As a first verification of this fact, the mutual inductances between the moving coil and the two supply coils have been computed using (3.3) for different positions in the range [-20 mm, 20 mm] and for sample values of winding parameters. The results are depicted in Figure 3.4. It can be noted that the dependence on the position is linear and that the mutual inductances exhibits obviously the same value when the moving coil is in the center. This preliminary check helps understanding the final shape of the electrical magnitudes as functions of the position.

Regarding the self-inductance, it can be seen as the superposition of the self-inductances of each layer of the thick winding and the mutual inductances between the layers of the same winding. The self-inductance of a layer is computed as [67]:

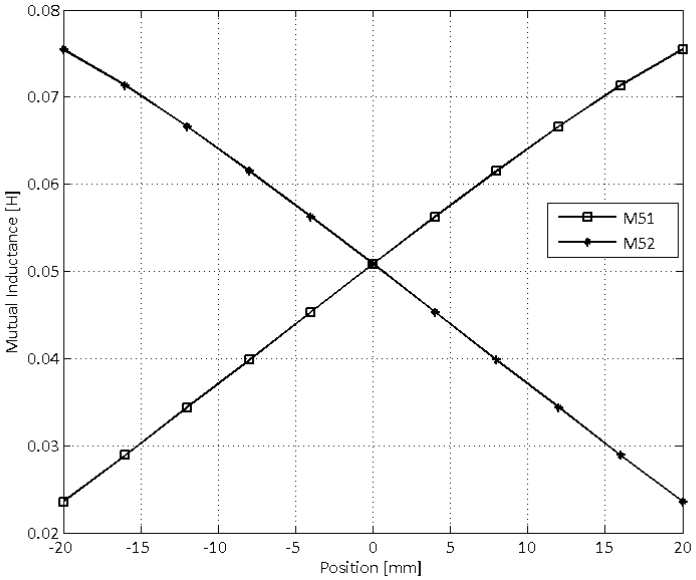

Figure 3.4. Example of mutual inductance computation as a function of relative position between supply and moving coils. N_{lp} = 4, N_{ls} = 5, N_p = 5000, N_s = 3000.

$$L_l = \frac{\mu_0 \pi N^2 R^2}{2s} T(k_l) \tag{3.7}$$

where N is the number of turns, R the layer radius, s the winding semi-length and

$$T(k_l) = \frac{4}{3\pi\beta k_l^3}\left[\left(2k_l^2 - 1\right)E(k_l) + \left(1 - k_l^2\right)K(k_l) - k_l^3\right]$$
$$k_l^2 = (1 + \beta^2)^{-1}, \quad \beta = \frac{s}{R}. \tag{3.8}$$

The mutual inductance between the layers (i.e. the second term to consider to calculate the self-inductance) is computed using (3.1) for each combination of two layers in the same winding (3.3).

The mutual inductance of a thick winding expressed in (3.3) involves the computation of an elementary mutual inductance, expressed in (3.1), for $G = N_{lp} \times N_{ls} \times N_p \times N_s$ times. The computation of such elementary contribution entails on turn the evaluation of complete elliptic integrals (which can be carried out numerically). For the sensor's design, *G* can be a very big number (e.g. order of 10^7), which leads to the possibility of having very high computational time for the mutual inductances. Finally, given the presence of 5 windings, the computation of all the mutual inductances at all the desired position values can be a seriously time-consuming task. In addition, all mutual inductances involved in the 5-winding sensor's arrangement contribute to its functioning, so none of them can be discarded because of the processing burden.

The criticality of such computational time lies also in the fact that the model has to be a valid tool for the sensor's design, which includes repeated evaluations for optimization, fast counterchecks and rapid parametric analysis. The high computational load would thus lead to a weakening of the design tool which the model is intended to provide.

For these reasons, an approximated computation of the total mutual inductances can be adopted, by defining an iteration scaling factor

$$s = \frac{G_{app}}{G_{prec}}. \tag{3.9}$$

where G_{app} and G_{prec} are the number of iterations (i.e. number of evaluations of mutual inductance of two single turns) in the approximated and in the precise calculation respectively. The value of s can be chosen in order to reduce the computational time. The calculation of the mutual inductance can be then performed applying the scaling factor to the number of turns per layer, which means a reduced number of iterations, precisely

$$G_{app} = N_{lp} \times N_{ls} \times \sqrt{s}N_p \times \sqrt{s}N_s \tag{3.10}$$

The resulting mutual inductance can be then divided by s to have an approximate value. This operation is equivalent to first reduce the number of turns per layer (i.e. modify the winding arrangement) and then assume the mutual inductance approximately linear with N_pN_s for big values of this product. The scaling factor has been applied to the number of turns per layer being this the biggest number in the factors forming *G* (e.g. several hundreds or even thousands conductors per layer). By doing so, the winding arrangement is less significantly modified.

Figure 3.5 shows the approximation error in a case study where the computational time is in the order of some hours (N_{lp} = 4, N_{ls} = 5, N_p = 5000, N_s = 3000) as a function of the desired scaling factor. The approximation error is computed as the percentage difference between the values of

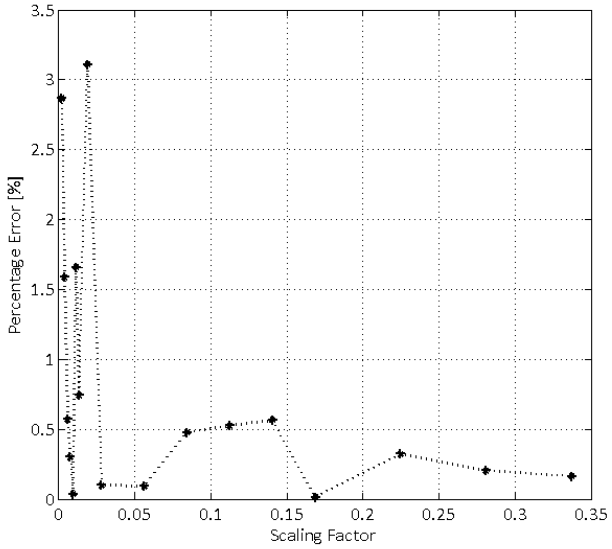

Figure 3.5. Computation error versus scaling factor for the approximated calculation of the total mutual inductance between two thick windings.

mutual inductance obtained with and without the approximation. For very low values (i.e. very pronounced approximation and very high computational time saving) the error is not stable and reaches a maximum of about 3 %, whereas for more reasonable values it stays always under 0.5 %. Therefore, to assure good computational time and at the same time not to make a relevant error, the scaling factor should be the result of a compromise. As an example, choosing a scaling factor of 0.1 has led to a computational time saving of more than 80 %.

In conclusion, using (3.3), adopting approximated computation in case of big processing load, and (3.7), all mutual and self-inductances of the 5-winding structure in Figure 3.1 can be calculated for different values of the moving coil position. The electrical quantities (voltages and currents) have to be determined at the next stage.

3.2.3. Derivation of Electrical Quantities

Since the moving coil is short-circuited, by simply applying the voltage balance on its mesh and considering all the magnetic fluxes coupled with the coil, one can obtain the induced current

$$\underline{I}_5 = -\frac{j\omega}{\underline{Z}_5}\left(M_{51}\underline{I}_1 + M_{52}\underline{I}_2\right) \tag{3.11}$$

where $\underline{Z}_i = R_i + j\omega L_i$ is the winding impedance of the i-th coil (in the case of the moving coil, the impedance of the short-circuited winding), M_{ij} is the mutual inductance between windings *i* and *j* and $\underline{I}_i$ is the current in coil i. Equation (3.11) implicitly assumes that no current is flowing in the sense windings (connected to the high-input-impedance readout system).

The sense voltages are functions of the magnetic fluxes generated by the supply coils and the moving coil (due to the induced current $\underline{I}_5$). As a result, the sense voltages are functions of the supply currents and the current in the moving coil, as follows

$$\begin{aligned}\underline{V}_3 &= j\omega\left(M_{31}\underline{I}_1 + M_{32}\underline{I}_2 + M_{35}\underline{I}_5\right)\\ \underline{V}_4 &= j\omega\left(M_{42}\underline{I}_2 + M_{41}\underline{I}_1 + M_{45}\underline{I}_5\right)\end{aligned} \tag{3.12}$$

Substituting (3.11) into (3.12), the sense voltages can be expressed as

$$\begin{aligned}\underline{V}_3 &= j\omega\left(M_{31}\underline{I}_1 + M_{32}\underline{I}_2 - \frac{j\omega M_{35}}{\underline{Z}_5}M_{51}\underline{I}_1 - \frac{j\omega M_{35}}{\underline{Z}_5}M_{52}\underline{I}_2\right)\\ \underline{V}_4 &= j\omega\left(M_{42}\underline{I}_2 + M_{41}\underline{I}_1 - \frac{j\omega M_{45}}{\underline{Z}_5}M_{51}\underline{I}_1 - \frac{j\omega M_{45}}{\underline{Z}_5}M_{52}\underline{I}_2\right)\end{aligned} \tag{3.13}$$

In (3.13), all mutual inductances involving winding 5 depend on the position. The voltages of the supply coils are

$$\begin{aligned}\underline{V}_1 &= R_1\underline{I}_1 + j\omega L_1\underline{I}_1 + M_{12}\underline{I}_2 + j\omega M_{15}\underline{I}_5\\ \underline{V}_2 &= R_2\underline{I}_2 + j\omega L_2\underline{I}_2 + M_{21}\underline{I}_1 + j\omega M_{25}\underline{I}_5\end{aligned} \tag{3.14}$$

The relations in (3.12), (3.13) and (3.14) are general, since they are valid in any supply condition.

In the case of current supply, it can be stated that $\underline{I}_2 = -\underline{I}_1 = \underline{I}$. In reality, as explained in section 3.1, having two 180-degree-out-of-phase current signals is not the only way for creating two equal-and-opposite supply magnetic fields. Choosing opposite wiring directions for the two windings and feeding them in series lead to the same result with a difference in the phase-shift between the supply voltages. However, choosing opposite wiring directions for the two supply windings corresponds to giving negative values to the mutual inductances between them (and, in general, between all windings with opposite wiring directions, given the opposite directions of the coil cross-section unit vectors [68]). From (3.14) it is evident that the two choices bring to the same voltages amplitude, but different phases. Therefore, since the voltage amplitude (not the phase) is the significant quantity in the model formulation, the two choices can be considered equivalent. Thus, considering $\underline{I}_2 = -\underline{I}_1 = \underline{I}$, the supply voltages become

$$\begin{aligned}\underline{V}_1 &= R_1\underline{I} + j\omega(L_1 - M_{12})\underline{I} + j\omega M_{15}\underline{I}_5\\ \underline{V}_2 &= -R_2\underline{I} + j\omega(M_{21} - L_2)\underline{I} + j\omega M_{25}\underline{I}_5\end{aligned} \tag{3.15}$$

whereas the sense voltages can be obtained starting from (3.13), as follows

$$\begin{aligned}\underline{V}_3 &= j\omega(M_{31} - M_{32})\underline{I} + \omega^2\underline{I}\left(\frac{M_{35}M_{51}}{\underline{Z}_5} - \frac{M_{35}M_{52}}{\underline{Z}_5}\right)\\ \underline{V}_4 &= -j\omega(M_{42} - M_{41})\underline{I} + \omega^2\underline{I}\left(\frac{M_{45}M_{51}}{\underline{Z}_5} - \frac{M_{45}M_{52}}{\underline{Z}_5}\right)\end{aligned} \tag{3.16}$$

Equations (3.16) show that the sense voltages can be seen as the superposition of the induced voltage due to the primary current (first term, attenuated by the cross-coupling between the supply coils), which is independent from the position, and the "perturbing" voltage due to the moving coil counter-flux (second term), which gives the dependence on the position. As a matter of fact, if the moving coil was absent, the second terms in (3.16) would be null. This term would also vanish if the moving coil was open-circuited. Actually, in this case, there would be an induced voltage in such coil, but not an induced current, and therefore the expression for the sense voltage could be derived from (3.16) imposing $|\underline{Z}_5| \to \infty$. The short-circuiting of the moving coil is then demonstrated to be a necessary condition for the sensor to work properly.

Equations (3.15) prove that the voltages of the supply windings depend on turn on the moving coil position. In fact, they can be seen as the superposition of a constant term (due to the resistance, the self-inductance and the mutual inductance between the supply coils) and a variable term (due to

the perturbation of the moving coil flux). This is an interesting result, since in applications where the current supply is a possible option, the supply windings could actually replace the sense windings. In practice, the supply would be performed in current, whereas the reading would be performed in voltage on the same windings. Nevertheless, investigations regarding the thermal behaviour of the sensor should be advanced when adopting this choice, as will be discussed in the following sections.

A more complete expression of the supply voltages can be found substituting (3.11) into (3.15), obtaining

$$\begin{aligned}\underline{V}_1 &= R_1\underline{I} + j\omega(L_1 - M_{12})\underline{I} + \frac{\omega^2 \underline{I}}{\underline{Z}_5} M_{15}(M_{51} - M_{52}) \\ \underline{V}_2 &= -R_2\underline{I} + j\omega(M_{21} - L_2)\underline{I} + \frac{\omega^2 \underline{I}}{\underline{Z}_5} M_{25}(M_{51} - M_{52})\end{aligned} \tag{3.17}$$

In case of voltage supply, $\underline{V}_2 = -\underline{V}_1 = \underline{V}$. In this case the formulation becomes more complicated, since the supply currents are now depending on the position (as the supply voltages were, in case of current supply). In particular, starting from (3.14), the supply currents can be written as

$$\begin{aligned}\underline{I}_1 &= \frac{\underline{V}}{\underline{Z}_1} - j\omega\frac{M_{12}\underline{I}_2}{\underline{Z}_1} - j\omega\frac{M_{15}\underline{I}_5}{\underline{Z}_1} \\ \underline{I}_2 &= \frac{-\underline{V}}{\underline{Z}_2} - j\omega\frac{M_{21}\underline{I}_1}{\underline{Z}_2} - j\omega\frac{M_{25}\underline{I}_5}{\underline{Z}_2}\end{aligned} \tag{3.18}$$

where the first terms are due to the winding impedance, the second terms are due to the coupling between the supply windings and the third terms are due to the coupling with the moving coil. Equations (3.18) and (3.11) constitute a system of three linearly-independent equations with three unknowns (the three currents). Once solved, the moving coil current can be expressed as

$$\underline{I}_5 = \frac{\left(\frac{\underline{V}\cdot M_{52}}{\underline{Z}_2}\underline{A}_2 - \frac{\underline{V}\cdot M_{51}}{\underline{Z}_1}\underline{A}_1\right)\cdot \underline{C}}{1 - \omega\underline{C}\left(\frac{M_{51}}{\underline{Z}_1}\underline{B}_1 + \frac{M_{52}}{\underline{Z}_2}\underline{B}_2\right)} \tag{3.19}$$

where

$$\begin{aligned}\underline{A}_1 &= 1 + j\omega\frac{M_{12}}{\underline{Z}_2}, \qquad \underline{A}_2 = 1 + j\omega\frac{M_{21}}{\underline{Z}_1} \\ \underline{B}_1 &= jM_{15} + \omega\frac{M_{12}M_{25}}{\underline{Z}_2}, \qquad \underline{B}_2 = jM_{25} + \omega\frac{M_{21}M_{15}}{\underline{Z}_1} \\ \underline{C} &= \frac{j\omega}{\underline{Z}_5\left(1 + \omega^2\frac{M_{12}^2}{\underline{Z}_1\underline{Z}_2}\right)}\end{aligned} \tag{3.20}$$

whereas the two supply currents are

$$\begin{aligned}\underline{I}_1 &= \frac{\frac{\underline{V}}{\underline{Z}_1}\underline{A}_1 - \frac{\underline{V}}{\underline{Z}_1}\omega\cdot\underline{C}\frac{M_{52}}{\underline{Z}_2}\left(\underline{A}_1\underline{B}_2 + \underline{A}_2\underline{B}_1\right)}{\frac{j\omega}{\underline{Z}_5\underline{C}}\left[1 - \omega\cdot\underline{C}\left(\frac{M_{51}}{\underline{Z}_1}\underline{B}_1 + \frac{M_{52}}{\underline{Z}_2}\underline{B}_2\right)\right]} \\ \underline{I}_2 &= \frac{\frac{-\underline{V}}{\underline{Z}_2}\underline{A}_2 + \frac{\underline{V}}{\underline{Z}_2}\omega\cdot\underline{C}\frac{M_{51}}{\underline{Z}_1}\left(\underline{A}_1\underline{B}_2 + \underline{A}_2\underline{B}_1\right)}{\frac{j\omega}{\underline{Z}_5\underline{C}}\left[1 - \omega\cdot\underline{C}\left(\frac{M_{51}}{\underline{Z}_1}\underline{B}_1 + \frac{M_{52}}{\underline{Z}_2}\underline{B}_2\right)\right]}\end{aligned} \tag{3.21}$$

Simple considerations can be done concerning equations (3.21) and (3.19) in order to verify their consistence. If all mutual inductances were null (i.e. no magnetic coupling between windings), the terms $\underline{A}_j$ and $\underline{B}_j$ would approach zero, the term $\underline{C}$ would tend towards $j\omega/\underline{Z}_5$ and then the currents would be given by the following quantities

$$\underline{I}_1 = \frac{\underline{V}}{\underline{Z}_1}, \qquad I_2 = \frac{-\underline{V}}{\underline{Z}_2}, \qquad \underline{I}_5 = 0 \tag{3.22}$$

which is consistent with the hypothesis. In practice, this situation would describe the currents of three independent electrical circuits. Once again, if the moving coil was not open-circuited, $\underline{I}_5$ would vanish in (3.18) and there would be no dependence on the position. In (3.21), the first term of the numerator is the current which is due to the self-inductance and the mutual inductance between the supply coils (independent from the position), whereas the other terms take into account the influence of the magnetic coupling with the moving coil (which depends on the position).

The two sense coils' voltages can be finally found by substituting (3.19) and (3.21) into the general expression (3.12), obtaining

$$\begin{aligned}
\underline{V}_3 = j\omega \Bigg(& \frac{\underline{V}\left(\frac{\underline{A}_1}{\underline{Z}_1}M_{31} - \frac{\underline{A}_2}{\underline{Z}_2}M_{32}\right) - \frac{\omega \cdot \underline{C} \cdot \underline{V}}{\underline{Z}_1\underline{Z}_2}\left(\underline{A}_1\underline{B}_2 + \underline{A}_2\underline{B}_1\right)\left(M_{31}M_{52} - M_{32}M_{51}\right)}{\frac{j\omega}{\underline{Z}_5\underline{C}}\left[1 - \omega \cdot \underline{C}\left(\frac{M_{51}}{\underline{Z}_1}\underline{B}_1 + \frac{M_{52}}{\underline{Z}_2}\underline{B}_2\right)\right]} \\
& + M_{35}\frac{\underline{V}\left(\frac{\underline{A}_2}{\underline{Z}_2}M_{52} - \frac{\underline{A}_1}{\underline{Z}_1}M_{51}\right) \cdot \underline{C}}{1 - \omega \cdot \underline{C}\left(\frac{M_{51}}{\underline{Z}_1}\underline{B}_1 + \frac{M_{52}}{\underline{Z}_2}\underline{B}_2\right)}\Bigg) \\
\underline{V}_4 = j\omega \Bigg(& \frac{\underline{V}\left(\frac{\underline{A}_1}{\underline{Z}_1}M_{41} - \frac{\underline{A}_2}{\underline{Z}_2}M_{42}\right) - \frac{\omega \cdot \underline{C} \cdot \underline{V}}{\underline{Z}_1\underline{Z}_2}\left(\underline{A}_1\underline{B}_2 + \underline{A}_2\underline{B}_1\right)\left(M_{41}M_{52} - M_{42}M_{51}\right)}{\frac{j\omega}{\underline{Z}_5\underline{C}}\left[1 - \omega \cdot \underline{C}\left(\frac{M_{51}}{\underline{Z}_1}\underline{B}_1 + \frac{M_{52}}{\underline{Z}_2}\underline{B}_2\right)\right]} \\
& + M_{45}\frac{\underline{V}\left(\frac{\underline{A}_2}{\underline{Z}_2}M_{52} - \frac{\underline{A}_1}{\underline{Z}_1}M_{51}\right) \cdot \underline{C}}{1 - \omega \cdot \underline{C}\left(\frac{M_{51}}{\underline{Z}_1}\underline{B}_1 + \frac{M_{52}}{\underline{Z}_2}\underline{B}_2\right)}\Bigg)
\end{aligned} \tag{3.23}$$

The first terms of the numerators of (3.23) depend on the coupling between the sense and supply windings (independent from the position), whereas the remaining terms depend on the coupling between supply, sense and moving coils (which gives the dependence on the position).

To make a comparison with the current supply case, it is evident that in voltage supply the effect of the moving coil on the sense coils acts in two manners: it perturbs the flux linkage between supply and sense coils (as for current supply) but it modulates also the supply currents, which on turn affects the sense voltages. On the other hand, the analysis of current supply shows that the effect of the moving coil acts both on the sense and supply coils' voltages. Nevertheless, there is no direct relation between supply and sense voltages in current supply, so the two effects are separated. Figure 3.6 shows the computation of the sense voltages with current supply and the supply currents with voltage supply for illustrative values of winding parameters. It is evident that with voltage supply the supply currents exhibit dependence with the position, as from (3.21). A complete analysis concerning also the sense voltages in the two supply cases will be addressed in Chapter 4.

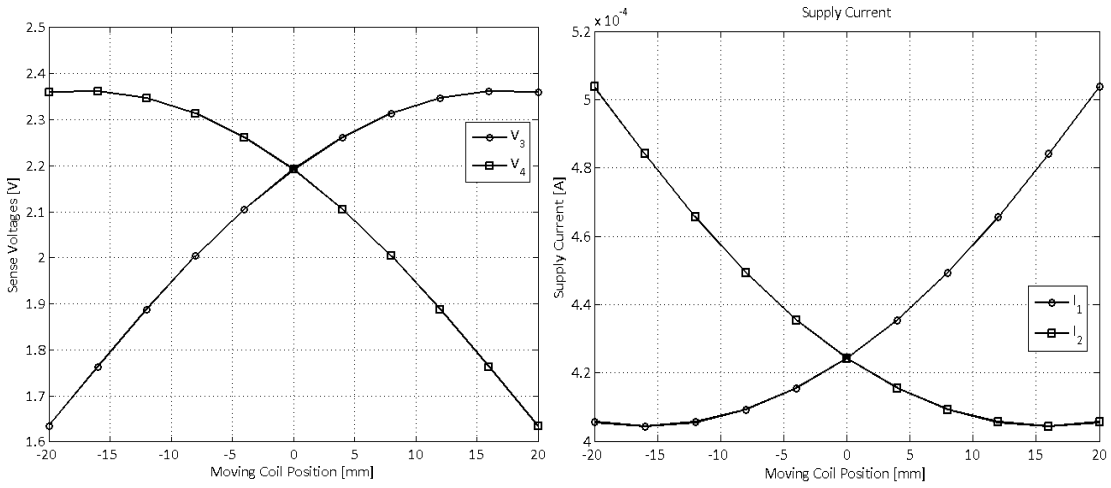

Figure 3.6. Computation through the electromagnetic model of (Left) sense voltages with current supply and (Right) supply current with voltage supply for illustrative values of winding parameters and dimensions.

It has to be pointed out that in the presented general formulation the two supply windings parameters (i.e. number of turns and dimensions) have not been considered necessarily equal (in general, this has not been considered for any couple of the 5 windings). In the case when the two coils are identical, the two impedances $\underline{Z}_1$ and $\underline{Z}_2$ exhibit the same value and the terms $\underline{A}_1$ and $\underline{A}_2$ in (3.20) coincide. $\underline{B}_1$ and $\underline{B}_2$ do not coincide (unless the moving coil is in the center) since the mutual inductances M_{15} and M_{25} are reciprocal (i.e. when the moving coil moves towards positive positions, M_{15} increases whereas M_{25} decreases and vice versa). In general, the following identities are valid

$$\begin{aligned} \underline{Z}_1 = \underline{Z}_2 = \underline{Z}_s, \qquad & \underline{A}_1 = \underline{A}_2 = \underline{A} \\ M_{31} = M_{42} = M_{ssd}, \qquad & M_{32} = M_{41} = M_{ssc} \end{aligned} \tag{3.24}$$

adding to the general relationship $M_{ij} = M_{ji}$ given by the reciprocity theorem [69], which is always valid. In (3.24), the mutual inductances have been renamed with M_{ssd} and M_{ssc} to indicate the direct (the winding are facing each other) or crossed coupling (the windings are one on each side of the sensor) between sense and supply windings. Taking into account there relations, the sense voltages in case of voltage supply can be written as

$$\begin{aligned} \underline{V}_3 = j\omega \Bigg(& \frac{\frac{\underline{A}}{\underline{Z}_s}\underline{V}(M_{ssd} - M_{ssc}) - \frac{\omega \cdot \underline{C} \cdot \underline{V} \cdot \underline{A}}{\underline{Z}_s^2}\left(\underline{B}_2 + \underline{B}_1\right)(M_{ssd}M_{52} - M_{ssc}M_{51})}{\frac{j\omega}{\underline{Z}_5\underline{C}}\left[1 - \omega \cdot \frac{\underline{C}}{\underline{Z}_s}\left(M_{51}\underline{B}_1 + M_{52}\underline{B}_2\right)\right]} \\ & + M_{35}\frac{\frac{\underline{A}}{\underline{Z}_s}\underline{V}(M_{52} - M_{51}) \cdot \underline{C}}{1 - \omega \cdot \frac{\underline{C}}{\underline{Z}_s}\left(M_{51}\underline{B}_1 + M_{52}\underline{B}_2\right)} \Bigg) \\ \underline{V}_4 = j\omega \Bigg(& \frac{\frac{\underline{A}}{\underline{Z}_s}\underline{V}(M_{ssc} - M_{ssd}) - \frac{\omega \cdot \underline{C} \cdot \underline{V} \cdot \underline{A}}{\underline{Z}_s^2}\left(\underline{B}_2 + \underline{B}_1\right)(M_{ssc}M_{52} - M_{ssd}M_{51})}{\frac{j\omega}{\underline{Z}_5\underline{C}}\left[1 - \omega \cdot \frac{\underline{C}}{\underline{Z}_s}\left(M_{51}\underline{B}_1 + M_{52}\underline{B}_2\right)\right]} \\ & + M_{45}\frac{\frac{\underline{A}}{\underline{Z}_s}\underline{V}(M_{52} - M_{51}) \cdot \underline{C}}{1 - \omega \cdot \frac{\underline{C}}{\underline{Z}_s}\left(M_{51}\underline{B}_1 + M_{52}\underline{B}_2\right)} \Bigg) \end{aligned} \tag{3.25}$$

Equations (3.25) better highlight in brackets the terms which give the dependence on the position and points out the reciprocity of the sense voltages, evident in the formulation. The relations that concern the sense voltages, supply currents and voltages in the two supply cases do not experience relevant formulation changes when including (3.24).

Table 3.1 summarizes the results of the model in terms of formulas (referring to the numeration) and the position-dependence of each of the analysed magnitudes.

The immunity to external DC magnetic fields is intrinsic to the design of the sensor's working principle and coil assembly, since such a field would not yield any voltage contribution. From the point of view of the model, a DC field cannot have influence on the analysed magnitudes, since they are sinusoidal waves (as a consequence, the analysis has been performed in the phasors' domain). On the other hand, an ultra-low-frequency interfering sinusoidal field would actually give rise to sinusoidal voltages on the windings, according to Faraday's law. Nevertheless, such components would also have no effect on the sensor's reading, since this is performed selecting the specific harmonics of the windings' voltages at the excitation frequency (i.e. some kHz). Therefore, the low-frequency components will be filtered out and no cross-effect on the main harmonics will be present, being linear the whole system described in the model. The same principle applies for very high frequency sine-waves (e.g. coming from electromagnetic emission of switching amplifiers), which do not influence the main harmonic of the signal.

The validation of the presented model, performed on a Finite Element geometry of the sensor and on a custom I2PS prototype, will be addressed in Chapter 4.

Magnitude	Current Supply	Voltage Supply
Supply Coils' Voltage	(3.17) – Position-dependent	Position-independent
Supply Coils' Current	Position-independent	(3.21) – Position-dependent
Sense Coils' Voltage	(3.16) – Position-dependent	(3.23) – Position-dependent
Moving Coil Current	(3.11) – Position-dependent	(3.19) – Position-dependent

Table 3.1. Position dependences and formula summary for the Ironless Position Sensor electromagnetic model.

3.3. Modelling of Skin and Proximity Effects

In Section 3.2, the hypotheses of the low-frequency electromagnetic model have been listed and among them is the assumption that high-frequency phenomena are negligible so that they are not considered in the analytical formulations. In reality, given the presence of multiple-layer windings and the possibility to have a high number of turns per layer, the skin and proximity effects [70-72] may play an important role in the definition of the impedance at a certain frequency. In this section, an accurate model of skin and proximity effect for air-cored cylindrical coils made of round conductors is proposed and its integration with the low-frequency counterpart is also addressed.

3.3.1. The importance of a High-Frequency Model

As already mentioned, the main phenomena taking place at high frequency are the skin and proximity effects, together with the presence of parasitic capacitances. The limit of validity of the low-frequency model presented in Section 3.2 is the frequency at which these phenomena become

significant. The stray capacitances of a single coreless winding made of one or a few layers has been calculated in [73]. However, the Ironless Position Sensor is made of 5 different windings (which on turn can be made of several layers). Therefore, more complicated expressions and the need to define cross-winding capacitances (i.e. capacitances between 2 or more windings) are likely to foresee. On the other hand, a simple experimental frequency characterization (which can be carried out with an impedance analyser) can immediately locate the resonance frequency f_r of the device, therefore individuating a region in which the effects of parasitic capacitances are not significant and the impedances are predominantly inductive (i.e. below f_r).

On the contrary, the skin and proximity effects play an important role in defining the values of resistance and inductance of a multi-layer winding even below the resonance frequency (e.g. for inductors with several layers and/or thick wire diameter, as for the I2PS). Therefore, the conception of a dedicated electromagnetic model to describe such phenomena is needed. As a matter of fact, an experimental characterization (desirable to determine the resonance frequency) is here less advisable, since it should be performed separately for each winding, a hard task for an already-assembled sensor. In addition, an impedance analyser is capable to return the value of real and imaginary part of the impedance of the device under test, without distinguishing resistance, inductance and capacitance contributions.

The results of this dedicated analysis can be then merged with the low-frequency model, by foreseeing frequency-dependent resistance and inductance for each winding. It will be shown that the influence of this phenomenon is considerable especially on the winding resistance.

The availability of such a model will translate in a tool for the sensor's design, just as for the low-frequency model, with the difference that this analysis will be useful to determine the criticality of a winding resistance or inductance at a certain frequency.

3.3.2. The Hypotheses

The skin effect is due to the finite penetration of the magnetic field inside the wire cross section, which causes a non-uniform distribution of the current density. The proximity effect also leads to a concentration of the current density towards the edges of the cross section, but it is due to the magnetic field generated by the wires belonging to different layers (therefore, this effect will be more and more relevant as the number of layers increases).

An interesting study regarding skin and proximity effects is performed in [74] for planar foil conductors and [75] for ferrite inductors. The expression of the resistance as a function of the frequency is presented adopting the Dowell's approximation [74, 76]. The important hypotheses which are made in the mentioned papers are:

- The winding is made of planar current foils, so the curvature of the foil is not considered;
- Edge effects due to finite dimensions of the foils are not considered;
- The winding presents an ideal ferromagnetic core (i.e. a core made with a material with infinite relative permeability and null resistivity)[8];

[8] This hypothesis affects the boundary conditions of the problem and the solution in terms of magnetic and electric fields, but not the expression of the resistance as a function of the frequency.

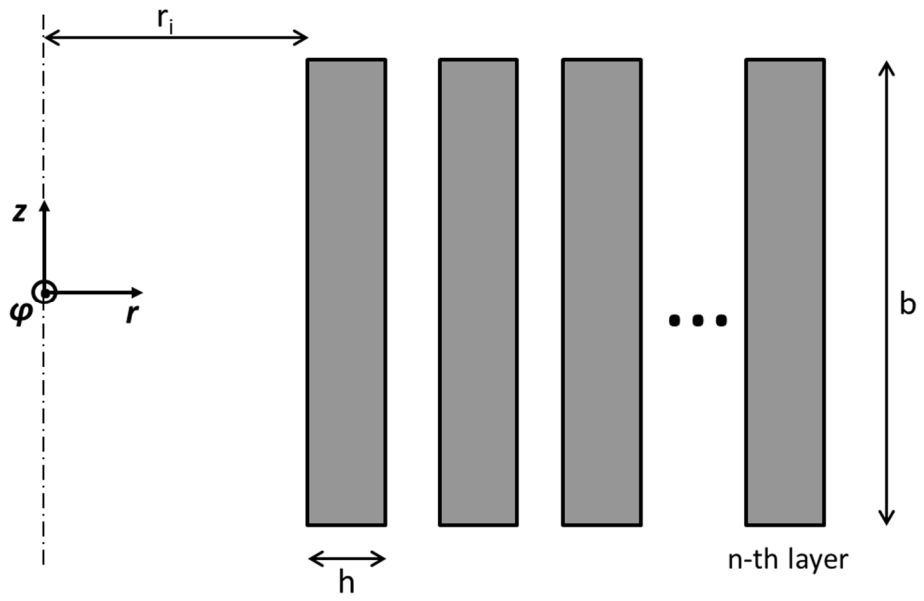

Figure 3.7. Two-dimensional geometry of a multi-layer foil winding for the skin and proximity effect electromagnetic treatment. In fact, the figure depicts half of the longitudinal cross section of the winding.

- The system is in magneto-quasi-static conditions (i.e. the displacement currents are considered negligible);
- The net charge density of the foil conductors is null;
- The system is under sinusoidal excitation.

Under these assumptions, the formulation of the electric and magnetic fields inside the foil conductors, as well as the current density, can be obtained developing the Maxwell's equations in a Cartesian coordinate system.

Nevertheless, this problem formulation cannot be suitable for the description of the skin and proximity effects taking place in a cylindrical winding with small radius (e.g. the moving coil of an Ironless Inductive Position Sensor), since the first hypothesis cannot be satisfied. In addition, the analysis has to be adapted also for air-cored windings of this type.

The analysed configuration is depicted in Figure 3.7. The following hypotheses are made to develop the analysis:

- The winding is made of cylindrical continuous current foils.
- The aspect ratio of the winding is high enough to consider the magnetic field always oriented axially and constant over the winding cross section. In symbols, referring to Figure 3.7:

$$\frac{h}{b} \ll 1 \tag{3.26}$$

- The net charge density of the conductors is null.
- The winding is air-cored.
- The system is in magneto-quasi-static conditions, therefore

$$\omega \varepsilon \rho \ll 1 \tag{3.27}$$

where ω is the angular frequency, ε is the dielectric constant, ρ is the wire resistivity. This assumption allows neglecting the displacement currents.

- The system is under sinusoidal excitation.

For the first hypothesis, the geometrical structure can be reduced to a two-dimensional problem, given the cylindrical symmetry. A cylindrical coordinate system can be set as in Figure 3.7. The second hypothesis and the device symmetry brings to the following identities in the time domain

$$\begin{aligned} H_r = 0, \quad H_z \neq 0, \quad H_\varphi = 0, \quad H = H(r) \\ E_r = 0, \quad E_z = 0, \quad E_\varphi \neq 0, \quad E = E(r) \end{aligned} \tag{3.28}$$

where E and H denote the electric and magnetic fields respectively. In addition, in (3.28) the general term A_k denotes the projection of the vector $\boldsymbol{A}$ onto the axis k. Therefore, all magnitudes listed in (3.28) are scalar values. For the last hypothesis, the electromagnetic analysis can be carried out in the phasors' domain. The current which is flowing in the windings can be written as

$$i(t) = I_m \cos(2\pi f_0 t) \tag{3.29}$$

3.3.3. The Electromagnetic Analysis

In the air region ($r < r_i$), given the absence of electrical currents, the second Maxwell's equation can be written as

$$\nabla \times \underline{\boldsymbol{H}} = 0 \tag{3.30}$$

Developing the equation on the axes and taking into account (3.28), one can find

$$\begin{aligned} \nabla \times \underline{\boldsymbol{H}} &= \left(\frac{1}{r}\frac{\partial \underline{H_z}}{\partial \varphi} - \frac{\partial \underline{H_\varphi}}{\partial z}\right)\boldsymbol{i_r} + \left(\frac{\partial \underline{H_r}}{\partial z} - \frac{\partial \underline{H_z}}{\partial r}\right)\boldsymbol{i_\varphi} + \frac{1}{r}\left(\frac{\partial\left(r\underline{H_\varphi}\right)}{\partial r} - \frac{\partial \underline{H_r}}{\partial \varphi}\right)\boldsymbol{i_z} \\ &= \left(-\frac{\partial \underline{H_z}}{\partial r}\right)\boldsymbol{i_\varphi} = 0 \;\rightarrow\; \underline{H_z} = const \end{aligned} \tag{3.31}$$

Therefore, in the air region, the magnetic field is oriented axially and is constant over the cross section, consistently with the hypotheses.

In the generic winding layer ($r_{n-1} < r < r_n$), the Maxwell's equations can be written as

$$\begin{aligned} \nabla \times \underline{\boldsymbol{E}} &= j\omega\mu\underline{\boldsymbol{H}} \\ \nabla \times \underline{\boldsymbol{H}} &= \sigma\underline{\boldsymbol{E}} \end{aligned} \tag{3.32}$$

with

$$\begin{aligned} \underline{\boldsymbol{E}} &= \underline{E_\varphi}(r)\boldsymbol{i_\varphi} \\ \underline{\boldsymbol{H}} &= \underline{H_z}(r)\boldsymbol{i_z} \end{aligned} \tag{3.33}$$

Before proceeding further, a clarification on the sign of the first equation in (3.32) has to be done. Usually, this Maxwell's equation is written with the 'minus' sign after the equal sign, according to Lenz law. Nevertheless, in an energized inductor the characteristic equation that links the voltage with the current is $\underline{V} = j\omega L\underline{I}$, where $L\underline{I}$ is the self-coupled magnetic flux generated by the energizing current. Manipulating this equation and applying the Stokes' theorem [77], it is possible to extract the first Maxwell's equation. The substantial difference stays in the fact that in an energized inductor the voltage is self-induced, so the 'minus' sign is absent and the Maxwell's equation can be written as in (3.32).

Developing the equation on the axes and taking into account (3.28), one can find

$$\nabla \times \underline{\boldsymbol{E}} = \frac{1}{r}\frac{\partial}{\partial r}\left(r\underline{E_\varphi}\right)\boldsymbol{i_z} = \left(\frac{\underline{E_\varphi}}{r} + \frac{\partial \underline{E_\varphi}}{\partial r}\right)\boldsymbol{i_z} = j\omega\mu\underline{H_z}\boldsymbol{i_z} \tag{3.34}$$

The equations in (3.32) can be then written in their scalar equivalent

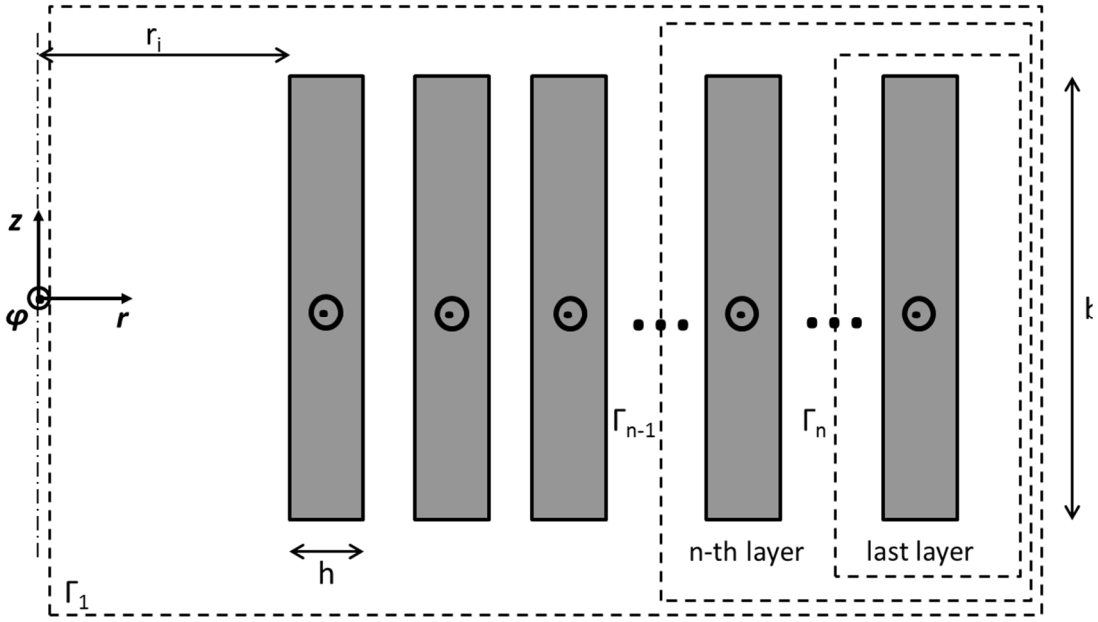

Figure 3.8. Two-dimensional geometry of a multi-layer foil winding with highlighted the current density direction and the curves for the application of Ampere's law, defining the boundary conditions.

$$\frac{\underline{E_\varphi}}{r} + \frac{\partial \underline{E_\varphi}}{\partial r} = j\omega\mu\underline{H_z}$$
$$-\frac{\partial \underline{H_z}}{\partial r} = \sigma\underline{E_\varphi} \tag{3.35}$$

In particular, deriving the second equation in (3.35) and substituting in the first, one can find

$$\frac{\partial^2 \underline{H_z}}{\partial r^2} + \frac{1}{r}\frac{\partial \underline{H_z}}{\partial r} + j\omega\sigma\mu\underline{H_z} = 0 \tag{3.36}$$

which corresponds to the scalar Helmholtz equation in cylindrical coordinates for H_z

$$\nabla^2 \underline{H_z} + k^2 \underline{H_z} = 0 \tag{3.37}$$

with $k^2 = j\omega\sigma\mu$. Multiplying (3.36) by r^2, the following Bessel's equation in cylindrical coordinates is obtained

$$r^2\frac{\partial^2 \underline{H_z}}{\partial r^2} + r\frac{\partial \underline{H_z}}{\partial r} + k^2 r^2 \underline{H_z} = 0 \tag{3.38}$$

The general solution of this equation is

$$\underline{H_z}(r) = A \cdot J_0(\underline{k}r) + B \cdot Y_0(\underline{k}r) \tag{3.39}$$

where $\underline{k} = \sqrt{j\omega\sigma\mu} = (1+j)/\delta$ with $\delta = \sqrt{2\rho/\omega\mu}$ being the penetration depth of the field in the layer[9]. J_0 and Y_0 are the zero-order Bessel's functions of first and second kind respectively. To find the constants A and B, the boundary conditions have to be imposed.

The boundary conditions can be found applying the Ampere's law on the curves Γ_{n-1} and Γ_n depicted in Figure 3.8 and assuming that the magnetic field outside the solenoid winding is null. Therefore, the values of magnetic field at the layer's boundaries are

$$\underline{H_z}(r_{ni}) = m\underline{H}^*, \qquad \underline{H_z}(r_{no}) = (m-1)\underline{H}^* \tag{3.40}$$

[9] The penetration depth is defined as the depth at which the field inside the material falls to 1/e (about 37%) of its original value at the surface.

where $m = N_l - n + 1$ with n being the layer number (starting from inner to outer) and N_l being the total number of layers. The quantity $\underline{H}^*$ is equal to I_m/b with I_m being the amplitude of the current, as in (3.29).

Therefore, applying (3.40) to the general solution (3.39), the two integration constants are

$$\begin{aligned}\underline{A} &= \underline{H}^* \frac{(m-1)\cdot Y_0(\underline{k}r_{ni}) - m\cdot Y_0(\underline{k}r_{no})}{Y_0(\underline{k}r_{ni})\cdot J_0(\underline{k}r_{no}) - Y_0(\underline{k}r_{no})\cdot J_0(\underline{k}r_{ni})} \\ \underline{B} &= \underline{H}^* \frac{m\cdot J_0(\underline{k}r_{no}) - (m-1)\cdot J_0(\underline{k}r_{ni})}{Y_0(\underline{k}r_{ni})\cdot J_0(\underline{k}r_{no}) - Y_0(\underline{k}r_{no})\cdot J_0(\underline{k}r_{ni})}\end{aligned} \tag{3.41}$$

For the sake of simplicity, the following notation will be followed henceforth

$$\underline{J}_0^i = J_0(\underline{k}r_{ni}),\ \ \underline{J}_0^o = J_0(\underline{k}r_{no}),\ \ \underline{Y}_0^i = Y_0(\underline{k}r_{ni}),\ \ \underline{Y}_0^o = Y_0(\underline{k}r_{no}) \tag{3.42}$$

Therefore, the magnetic field inside the n-th layer of a cylindrical winding made of N_l foils is

$$\underline{H_z}(r) = \underline{H}^* \left[\frac{(N_l-n)\underline{Y}_0^i - (N_l-n+1)\underline{Y}_0^o}{\underline{Y}_0^i\underline{J}_0^o - \underline{Y}_0^o\underline{J}_0^i}\cdot J_0(\underline{k}r) + \frac{(N_l-n+1)\underline{J}_0^o - (N_l-n)\underline{J}_0^i}{\underline{Y}_0^i\underline{J}_0^o - \underline{Y}_0^o\underline{J}_0^i} \cdot Y_0(\underline{k}r) \right] \tag{3.43}$$

From (3.35) and taking into account the following derivation properties of Bessel's functions [78]

$$\frac{\partial}{\partial x}\Big(J_p(\alpha x)\Big) = -\alpha J_{p+1}(\alpha x) + \frac{p}{x}J_p(\alpha x),\quad \frac{\partial}{\partial x}\Big(Y_p(\alpha x)\Big) = -\alpha Y_{p+1}(\alpha x) + \frac{p}{x}Y_p(\alpha x) \tag{3.44}$$

the electric field is also obtained

$$\underline{E_\varphi}(r) = \rho\underline{k}\cdot\underline{H}^* \left[\frac{(N_l-n)\underline{Y}_0^i - (N_l-n+1)\underline{Y}_0^o}{\underline{Y}_0^i\underline{J}_0^o - \underline{Y}_0^o\underline{J}_0^i}\cdot J_1(\underline{k}r) + \frac{(N_l-n+1)\underline{J}_0^o - (N_l-n)\underline{J}_0^i}{\underline{Y}_0^i\underline{J}_0^o - \underline{Y}_0^o\underline{J}_0^i}\cdot Y_1(\underline{k}r) \right] \tag{3.45}$$

Both (3.43) and (3.45) are valid in the interval $[r_{ni},\ r_{no}]$ and take into account the high-frequency effects (the factor $\underline{k}$ is affecting the magnetic and electric field distributions in different ways according to the considered layer). Finally, the expression of the current density is

$$\underline{J_\varphi}(r) = \underline{k}\cdot\underline{H}^* \left[\frac{(N_l-n)\underline{Y}_0^i - (N_l-n+1)\underline{Y}_0^o}{\underline{Y}_0^i\underline{J}_0^o - \underline{Y}_0^o\underline{J}_0^i}\cdot J_1(\underline{k}r) + \frac{(N_l-n+1)\underline{J}_0^o - (N_l-n)\underline{J}_0^i}{\underline{Y}_0^i\underline{J}_0^o - \underline{Y}_0^o\underline{J}_0^i}\cdot Y_1(\underline{k}r) \right] \tag{3.46}$$

Equation (3.46) takes into account the effect of the finite field penetration depth and the proximity with the other nearby conductors.

Figure 3.9 shows the trends of the normalized amplitudes of magnetic fields and current density for a case study. The graphs refer to the first layer, which is the most affected by the proximity effect. The trend of the electric field is not shown, since it coincides with the one of the current density, as from (3.45) and (3.46). It is possible to notice that the current density distribution exhibits a bigger sensitivity with respect to the frequency variations: at 1 kHz, it is already distributed around the edges of the section and in the center it reaches the 70 % of the maximum value. When the

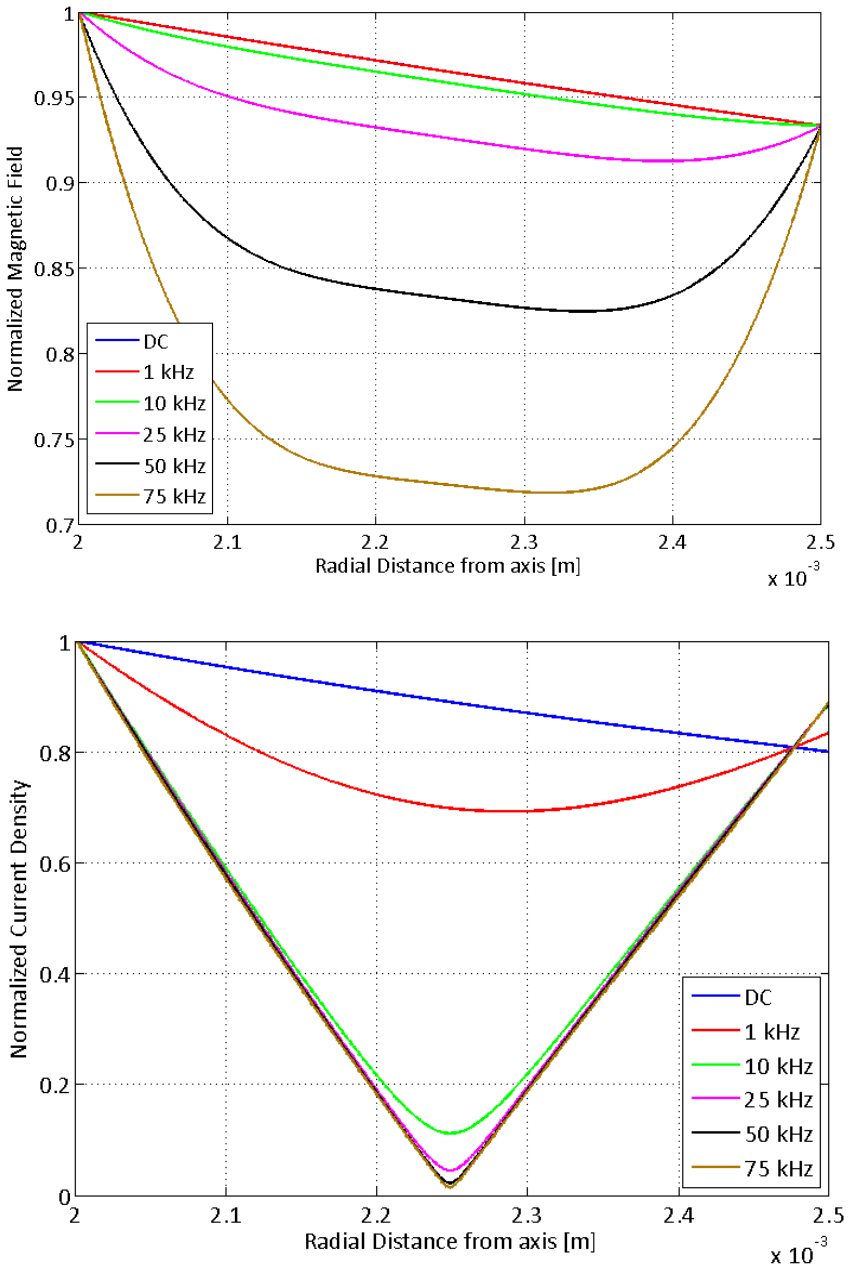

Figure 3.9. Normalized amplitude at different frequencies of (Top) magnetic field and (Bottom) current density in the first layer of a 15-layer winding made of 0.5-mm-thick copper wire foils. The inner radius of the coil is 2 mm. The electric field has the same behavior of the current density, as by the equations.

frequency rises at 10 kHz and more, the current density is almost entirely distributed along the edges of the section. It is interesting to notice that in static conditions the current density is anyway not constant across the section, due to the cylindrical geometry.

On the other hand, the magnetic field distribution does not change significantly from DC to 1 kHz (the two traces are practically superposed on the graph in Figure 3.9). At higher frequencies instead (i.e. above 10 kHz) the field concentrates along the edges, but in the center of the layer the magnetic field is still at more than 70 % of its maximum value.

This difference in the sensitivity of the distribution to the frequency already suggests that the parameter that is most influenced by the skin and proximity effects is the winding resistance

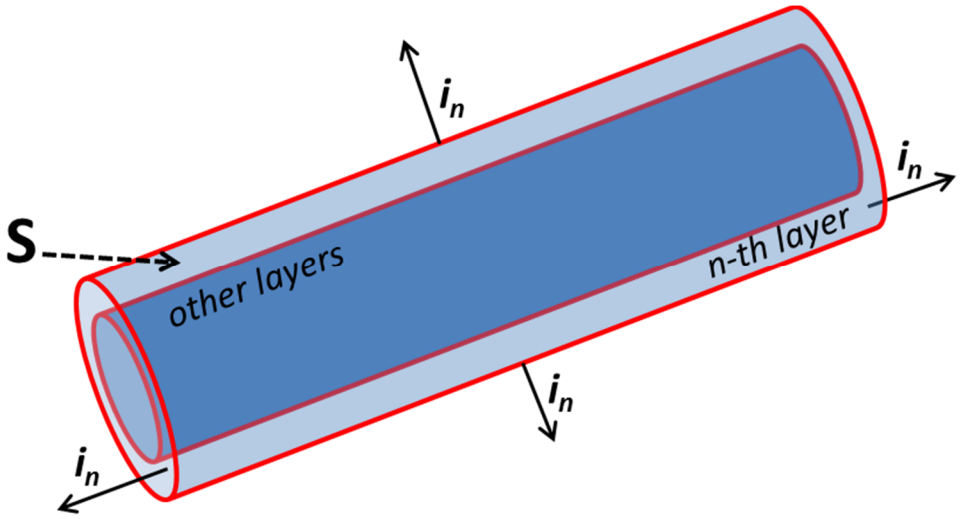

Figure 3.10. Surface of the n-th layer (individuated by the red lines). The blue volume corresponds to the layers from 1 to n-1. The light blue volume is the n-th layer. The layers from n+1 to N_l are not displayed. The arrows highlight the direction of the surface unit vectors.

(dependent on the electric field distribution), rather than the inductance (dependent on the magnetic field distribution).

3.3.4. Derivation of the Electrical Resistance

The analysis performed in the last sub-section draws the line on the electromagnetic phenomena which are taking place at high frequency inside the foil conductors that form the multi-layer winding. To embed the results of such important analysis in the low-frequency model described in Section 3.2, the electrical resistance of the winding has to be found. Once the dependence of the resistance on the frequency is formalized, the terms involving the winding resistances in the model's equations can be made frequency-dependent.

The electric and magnetic fields inside the foil conductors are given by (3.43) and (3.45). The active power associated with the n-th layer can be found calculating the Poynting's vector and recalling that the real part of the flux of this vector through the layer's surface corresponds to the active power dissipated in the volume described by the same surface (as from the Poynting's theorem [79, 80]). The active power can be then written as

$$P_n = Re\left\{\oint_S \underline{\boldsymbol{S}} \cdot \boldsymbol{i_n} dS\right\} = Re\left\{\oint_S \frac{1}{2}\left(\underline{\boldsymbol{E}} \times \underline{\boldsymbol{H}}^*\right) \cdot \boldsymbol{i_n} dS\right\} \tag{3.47}$$

where $\underline{\boldsymbol{H}}^*$ denotes the complex conjugate of $\underline{\boldsymbol{H}}$ and $\boldsymbol{i_n}$ is the unit vector pointing outside the surface S, which individuate the layer (Figure 3.10). Since the electric field is exclusively along φ and the magnetic field exclusively along z, the Poynting vector will have its only component along r. Therefore, the flux contributions associated to the sidewalls of the layer are null. The only significant contributions come from the vertical walls of the layer (i.e. the surfaces confining with the n-1-th and n+1-th layers). Referring to the notation in Figure 3.7, the active power then becomes

$$P_n = \frac{1}{2} \cdot Re\left\{2\pi b \cdot \left(r_{ni} \cdot \underline{E}_\varphi(r_{ni}) \cdot \underline{H}_z^*(r_{ni}) - r_{no} \cdot \underline{E}_\varphi(r_{no}) \cdot \underline{H}_z^*(r_{no})\right)\right\} \tag{3.48}$$

Taking into account the expressions of electric and magnetic fields (3.45) and (3.43) and substituting

them in (3.48), one can find (it is possible to demonstrate [74] that $\underline{H_z^*}(r) = \underline{H_z}(r)$ both in r_{ni} and r_{no})

$$P_n = Re\left\{2\pi\underline{k}b\cdot\rho\underline{H}^{*2}\left(r_{ni}\cdot\frac{(m^2-m)\left(\underline{Y_0^i}\underline{J_1^i}-\underline{J_0^i}\underline{Y_1^i}\right)-m^2\left(\underline{Y_0^o}\underline{J_1^i}-\underline{J_0^o}\underline{Y_1^i}\right)}{\underline{Y_0^i}\underline{J_0^o}-\underline{Y_0^o}\underline{J_0^i}}-r_{no}\right.\right.$$
$$\left.\left.\cdot\frac{[(m-1)^2]\left(\underline{Y_0^i}\underline{J_1^o}-\underline{J_0^i}\underline{Y_1^o}\right)-(m^2-m)\left(\underline{Y_0^o}\underline{J_1^o}-\underline{J_0^o}\underline{Y_1^o}\right)}{\underline{Y_0^i}\underline{J_0^o}-\underline{Y_0^o}\underline{J_0^i}}\right)\right\}\cdot\frac{1}{2} \tag{3.49}$$

Equation (3.49) relates the active power of the n-th layer with the frequency, the electromagnetic properties of the wire (i.e. its resistivity and permeability, through the factor $\underline{k}$) and the dimensions. The same calculation can be iterated for all the N_l layers of the winding (taking into account that the Bessel's functions will be defined in different points, so the factors introduced in (3.42) are different for each layer). Therefore, the total active power dissipated by the winding is then

$$P_{AC} = \sum_{n=1}^{N_l} P_n = \frac{1}{2}R_w I_m^2 = R_w I_{eff}^2 \tag{3.50}$$

where R_w denotes the resistance of the winding at the frequency chosen for the calculation and I_m is defined by (3.29). On the other hand, the dissipated power in DC is also known

$$P_{DC} = R_w^0 I_{DC}^2 \tag{3.51}$$

where R_w^0 is the value of the winding resistance at null frequency (static conditions). Therefore, assuming $I_{eff} = I_{DC}$, the resistance factor due to skin and proximity effect can be easily calculated as

$$F_R = \frac{P_{AC}}{P_{DC}} = \frac{R_w}{R_w^0} \tag{3.52}$$

The factor F_R describes how much the resistance of a foil winding of N_l layers is affected by the described high-frequency effects. It is frequency-dependent and is always greater than 1: as a matter of fact, since the current density distributes along the edges of the cross section (Figure 3.9), this can be seen as a decrease of the effective surface through which the current is flowing, therefore leading to an increase of the value of resistance. Figure 3.11 shows that the value of resistance can grow up to 10 times its DC value in a limited frequency range (from DC to 40 kHz) for common values of foil thickness and coil diameter. This highlights the criticality of this phenomenon for the correct modelling of the coil resistance of the Ironless Inductive Position Sensor up to several tens of kHz.

When the frequency becomes higher (hundreds of kHz), the evaluation of the Bessel's function and their differences (as from (3.49)) can be critical from the numerical point of view, since their products are much greater than their difference (e.g. the order of magnitude of the absolute value of the product between Bessel's functions can be of 10^{30}, whereas their difference can be of the order of 10^{-5}). In addition, as mentioned, at very high frequency the capacitance effects play the most important role. Therefore, the presented electromagnetic analysis and study on the winding resistance is useful for the sensor's model up to several tens of kHz (e.g. below 50/100 kHz according to the wire diameter). Above those frequencies, there is no more interest in modelling the sensor's functioning, since it will deviate from the principle of magnetic induction.

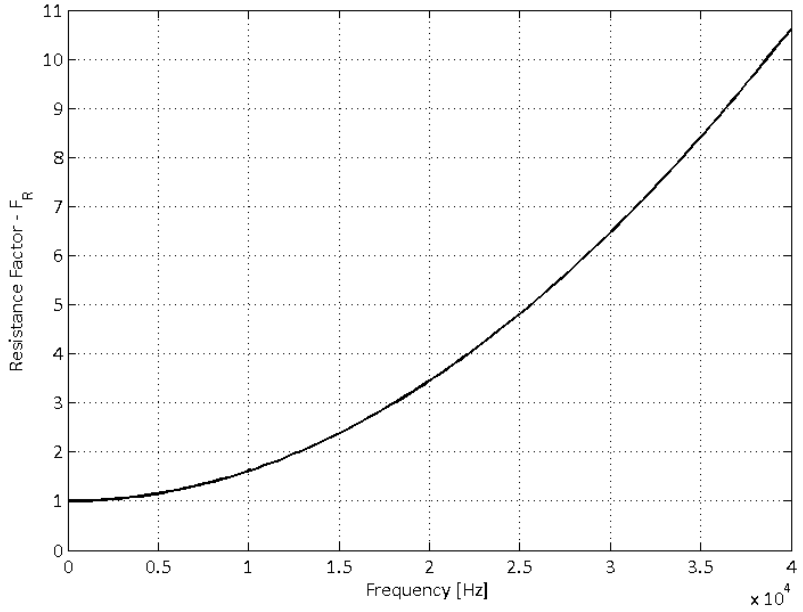

Figure 3.11. Resistance factor due to skin and proximity effects on a foil winding of 15 layers. The inner radius of the coil is 2 mm and the copper foils are 0.5 mm-thick.

On the other hand, the skin and proximity effects do not affect in a significant way the inductance of the foil layers for this frequency range. Figure 3.12 shows the reactive power (obtained as the imaginary part of the flux of the Poynting vector across the foil surface) associated to a winding with the same illustrative parameters as for Figure 3.11. It exhibits linear behaviour (i.e. the inductance is not changing significantly with the frequency). As a confirmation, the reactive power spectral density (i.e. the reactive power normalized to the value of frequency) decreases of less than 1.5 %.

These results confirms that for frequencies up to some tens of kHz, the low-frequency model can be used for predicting the voltages of the Ironless Inductive Position Sensor with the appropriate value of winding resistances given by the presented high-frequency model. The value of inductances can be calculated as explained in sub-section 3.2.2.

3.3.5. Approximation for Circular-wire Coils

The derivation of the electrical resistance has been made in the case of a winding made of several foil layers. The value of resistance of a winding made of circular coils wound in several layers can be found using an approximation [74]. Henceforth, the conductors' diameter will be indicated with d and the thickness of the insulator will be t, so that the quantity

$$p = d + 2t \tag{3.53}$$

can be used as the total diameter of the wire. The approximation process first defines a new foil layer, different from the original one (Figure 3.13), having the same thickness, but different length. The new length b_w is given by

$$b_w = h \cdot N_{cl} \tag{3.54}$$

where h is the side of the square conductors in Figure 3.13 and N_{cl} is the number of conductors in a single layer. The new foil has also a different resistivity, in order to exhibit the same resistance of the original foil. Therefore, the ratio between the two lengths coincides with the ratio between the two resistivities

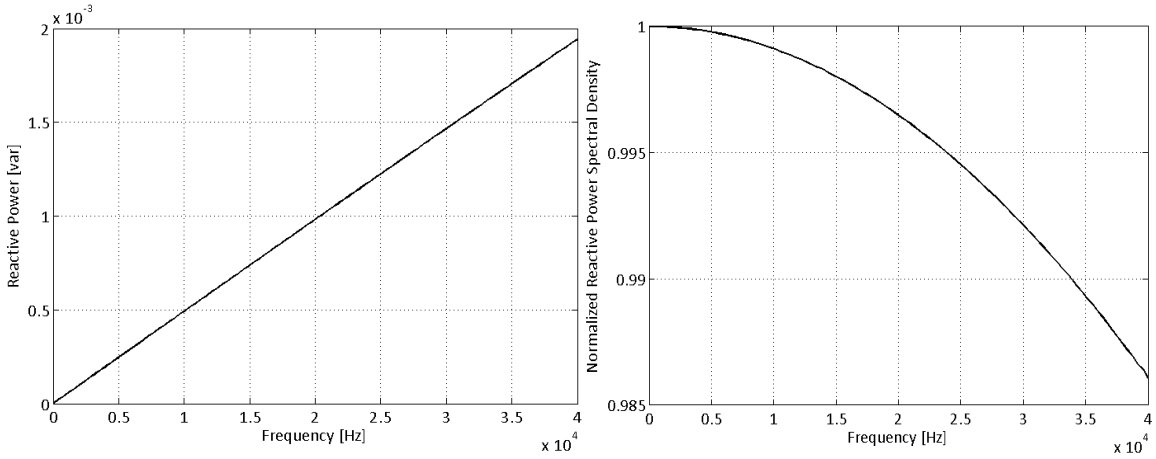

Figure 3.12. (Left) Reactive power associated with a foil winding for different frequencies. (Right) Reactive power spectral density normalized to its value at the lowest frequency. The inner radius of the coil is 2 mm and the copper foils are 0.5 mm-thick.

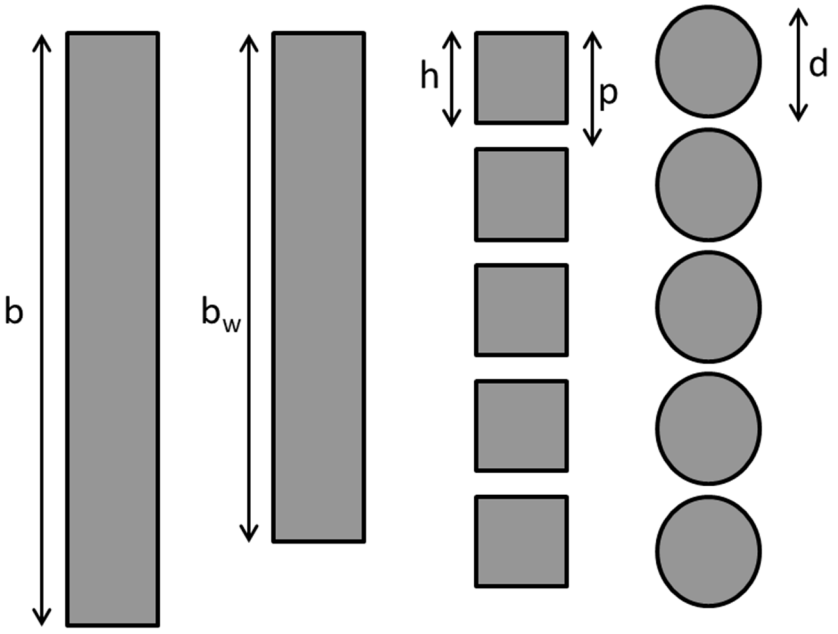

Figure 3.13. Approximation on the foil geometry for the determination of the resistance of a winding made of circular conductors.

$$\frac{\rho_w}{\rho} = \frac{b_w}{b} = \frac{h \cdot N_{cl}}{p \cdot N_{cl}} = \frac{h}{p} = \eta \tag{3.55}$$

The quantity η is known as the porosity factor, or fill factor [74]. To pass from square to round conductors, an equivalence between the surface areas of the square and the round conductors has to be imposed. By doing so, the diameter d can be written as

$$d = \frac{2h}{\sqrt{\pi}} \tag{3.56}$$

The process here presented should be reversed when the aim is to calculate the resistance of a winding made of circular conductors: the layer of N_{cl} round conductors should be first converted to a layer of N_{cl} square conductors with the same surface area and then convert it again to a rectangular foil layer with adjusted resistivity. Once this is done, equations (3.49), (3.50) and (3.52) can be used to calculate the resistance and the factor F_R.

At very high frequencies (e.g. hundreds of kHz), the porosity factor gives a good approximation only when the conductors are closely packed [74, 81, 82].

3.4. Modelling of Thermal Effects

The electromagnetic model described in Section 3.2 and the high-frequency analysis in Section 3.3 explain the working principle of the Ironless Inductive Position Sensor at a certain temperature (e.g. room temperature). As a matter of fact, no temperature dependence is considered in the presented equations. However, it is known that the value of resistivity of the wires is a function of its temperature, often approximated with a linear relation [83]. Thus, the value of resistance of each winding is in principle temperature-dependent.

The wire temperature depends on the ambient temperature and on the electrical current flowing in it (which acts as a heat generation). Therefore, the expression of the winding resistance and consequently the formulation of the temperature dependence of the sensor's position reading are not trivial. However, the presented modelling approach will demonstrate that for the Ironless Inductive Position Sensor the dependence of the winding resistance can be considered linear with the ambient temperature and the internal heat generation due to the electrical current can be neglected.

3.4.1. Temperature Distribution on the Winding Cross Section

The wire overheating can be avoided by limiting the current density flowing through it [84]. Finite-Element (FEM) simulations (Figure 3.14) also show that even taking into account the contact points between adjacent wires of the same winding layer, the temperature distribution in the wire cross section can be considered constant and approximated with the temperature of the surrounding air (in Figure 3.14 the difference from the ambient temperature is only 0.3 °C and the distribution is practically uniform along the wire section). The same results can be observed taking into account more contact points (e.g. between wires of different layers) and the presence of insulators.

These results allow considering the winding cross section as one continuous region (i.e. not subdivided into all the wires cross sections and air surfaces), as depicted in Figure 3.15. However, even if the temperature can be reasonably considered constant over the wire cross section, it is not obvious that it is also constant over the winding cross section.

As a matter of fact, adopting a cylindrical coordinate system and assuming high aspect ratio of the winding (i.e. the length of the winding is much larger than the diameter), the thermal exchange problem depicted in Figure 3.15 presents the following characteristics:

- Internal heat generation (due to the current flowing in the winding) influencing the temperature distribution;
- Dependence on the radius coordinate only (given the symmetry and the high aspect ratio);
- Dependence on the ambient temperature (the temperature distribution changes according to the temperature of the space outside the coil, the temperature of the space inside the coil and their difference).

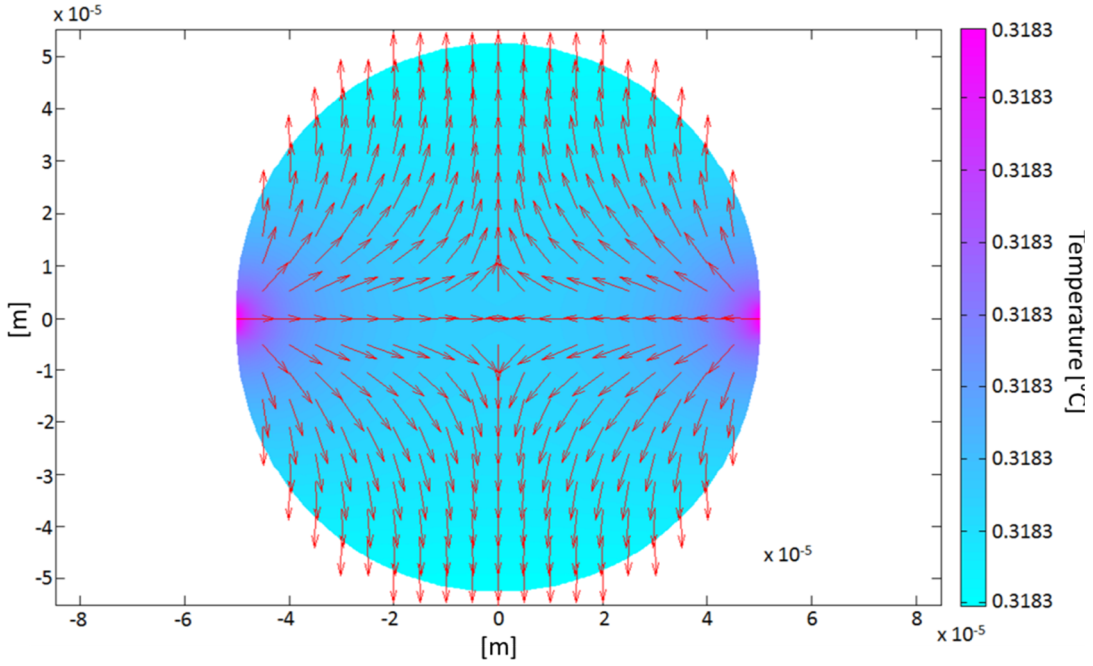

Figure 3.14. Effect of contact points on the temperature difference distribution (with respect to surrounding air) on a 0.1 mm-thick wire. The two contact points represent the regions where two adjacent wires of the same winding layer physically touch each other. The electrical current flowing in the nearby conductors is 50 mA_{RMS}. The arrows indicate the heat flow direction. Convective boundary conditions are imposed. The resolution of the heat partial differential equation has been performed with MATLAB.

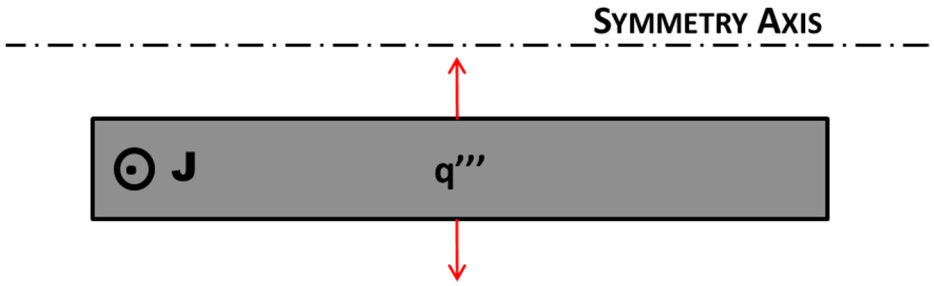

Figure 3.15. Half longitudinal cross section of a winding (the structure is symmetric around the axis). The direction of the current density is perpendicular to the plane. The arrows specify the thermal exchange with the environment. q''' represents the heat generation per unit volume due to the electrical current.

If the internal generation did not play a relevant role in defining the temperature distribution, the latter would be considered as exclusively dependent on the variations of the ambient temperature. Therefore, the associated value of resistance will be dependent on that temperature only. To demonstrate that, the effect of the internal heat generation on the temperature distribution has to be singled out. For this reason, the resolution of the heat equation in the structure depicted in Figure 3.15 has been performed keeping equal the temperatures of the two confining walls. In symbols,

$$\begin{gathered} \nabla \cdot (k_T \cdot \nabla T) + q''' = 0 \quad in\ [r_1, r_2] \\ T(r_1) = T(r_2) = T_f \end{gathered} \tag{3.57}$$

where r_1 and r_2 are the inner and outer winding radii and k_T is the thermal conductivity. The solution of (3.57) will provide the temperature distribution in the winding cross section given by the

internal heat generation only. The general solution of this partial differential equation in a cylindrical coordinates system is

$$T(r) = -\frac{q'''}{4k_T}r^2 + Alnr + B \tag{3.58}$$

Imposing the boundary conditions given in (3.57), it is possible to find

$$A = -\frac{\frac{q'''}{4k_T}(r_2^2 - r_1^2)}{ln\left(\frac{r_1}{r_2}\right)} \tag{3.59}$$

It is not necessary to determine the other constant B. In fact, it is just relevant to understand how much the temperature distribution given by (1.1) is far from being a constant. For this purpose, the knowledge of B is not crucial. To determine the range of variation of (1.1), its maximum can be calculated and compared to its minimum, to have the total temperature variation. The conditions to impose are

$$\frac{\partial T(r)}{\partial r} = 0 \;\; and \;\; \frac{\partial^2 T(r)}{\partial r^2} < 0 \quad in\,[r_1, r_2] \tag{3.60}$$

The first two derivatives of (1.1) are

$$\begin{aligned} \frac{\partial T(r)}{\partial r} &= -\frac{q'''}{2k_T}r + \frac{A}{r} \\ \frac{\partial^2 T(r)}{\partial r^2} &= -\frac{q'''}{2k_T} - \frac{A}{r^2} \end{aligned} \tag{3.61}$$

which automatically satisfy the second of the (3.60), being A always a positive quantity. Imposing the first condition in (3.60), the radius at which the temperature is maximal is

$$r_{max} = \sqrt{\frac{2k_T A}{q'''}} = \sqrt{\frac{r_2^2 - r_1^2}{2 \cdot ln(r_2/r_1)}} \tag{3.62}$$

To have an idea of the rough position of this maximum, the logarithm at the denominator can be approximated. Introducing the quantity

$$\frac{r_2}{r_1} = 1 + \left(\frac{r_2}{r_1} - 1\right) = 1 + y \tag{3.63}$$

and noticing that $y \ll 1$ since r_2 and r_1 are very close to each other for the I2PS windings, the logarithm can be expanded in its McLaurin series. Truncating at the first order, eq. (3.62) becomes

$$r_{max} \approx \sqrt{\frac{r_1(r_1 + r_2)}{2}} \tag{3.64}$$

It is interesting to notice that the maximum temperature does not occur at the midpoint between the radii, due to the cylindrical geometry. From (3.62) the maximum temperature in the winding's cross section can be calculated

$$T_{max} = T(r_{max}) = -\frac{q'''}{4k_T}r_{max}^2 + \frac{\frac{q'''}{4k_T}(r_2^2 - r_1^2)}{ln\left(\frac{r_2}{r_1}\right)}ln(r_{max}) + B \tag{3.65}$$

whereas its value on one of the borders (for $r = r_1$), where it can be graphically demonstrated that the minimum occurs, is

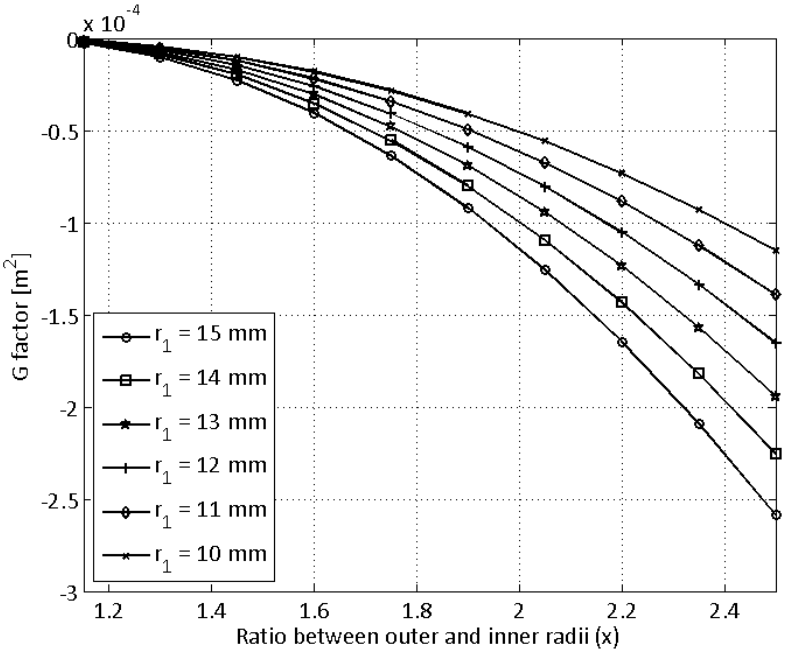

Figure 3.16. Geometrical factor *G* affecting the temperature distribution on the cross section of the winding.

$$T_{min} = T(r_1) = -\frac{q'''}{4k_T} r_1^2 + \frac{\frac{q'''}{4k_T}(r_2^2 - r_1^2)}{ln\left(\frac{r_2}{r_1}\right)} ln(r_1) + B \tag{3.66}$$

The difference between (3.65) and (3.66) gives the total temperature variation inside the winding cross section

$$\Delta T_{max} = -\frac{q'''}{4k_T}\left[\frac{r_1^2(x^2-1)}{2\,ln(x)} - r_1^2 - \frac{r_1^2(x^2-1)}{ln(x)} ln\left(\sqrt{\frac{(x^2-1)}{2\,ln(x)}}\right)\right] \tag{3.67}$$

where $x = r_2/r_1$. The quantity between square brackets is purely geometrical and depends on x and r_1, therefore

$$\Delta T_{max} = -\frac{q'''}{4k_T} \cdot G(x, r_1) \tag{3.68}$$

The factor G and its dependence on the geometrical parameters of the winding are shown in Figure 3.16. Multiplying G by the non-geometrical quantity in (3.67), the total temperature variation over the winding cross section can be obtained. It can be shown that limiting the current density in the wire (i.e. limiting the internal heat generation), just as it is done for avoiding the wire overheating, the temperature variation given by (3.67) is always under 0.5 °C (e.g. the non-geometrical factor in (3.67) is of the order of 10^3 for a current of 50 mA_{RMS} in a 0.1-mm-thick copper wire). For small values of x (which is the case for the supply and sense windings in the Ironless Inductive Position Sensor) the temperature variation becomes even more negligible.

For what has been said, the temperature distribution in the winding cross section is not significantly affected by the internal heat generation for typical values of radial dimensions of the Ironless Position Sensor's coils. Therefore, the temperature can be considered equal to the ambient temperature at steady state.

3.4.2. Temperature Dependence of the Position Reading

For what has been shown, the value of winding resistance depends on the variation of ambient temperature only, which modulates copper's resistivity. In this work, the temperatures of inner and outer spaces of the windings will be considered equal and the thermal steady state will be analysed.

A significant difference in the sensor's thermal behaviour is predictable according to the supply signal type (i.e. voltage or current). From (3.13) it is evident that with current supply, the two sense voltage amplitudes depend on the moving coil resistance only, whereas with voltage supply they are also function of the supply coils' resistances. All these quantities are affected by ambient temperature. For this reason, the current supply is a strongly favoured design choice and will be henceforth adopted. In addition, in Section 3.1 the possibility to sense the voltages directly on the supply coils has been advanced. However, in this case the voltage will also depend on the supply coils' resistances, so this solution is not adopted either.

In these conditions, the sense voltages can be expressed as (from (3.16))

$$\begin{aligned}\underline{V_3} &= j\omega(M_{31}-M_{32})\underline{I} + \omega^2\underline{I}\left(\frac{M_{35}M_{51}}{\underline{Z}_5(T)} - \frac{M_{35}M_{52}}{\underline{Z}_5(T)}\right)\\ \underline{V_4} &= -j\omega(M_{42}-M_{41})\underline{I} + \omega^2\underline{I}\left(\frac{M_{45}M_{51}}{\underline{Z}_5(T)} - \frac{M_{45}M_{52}}{\underline{Z}_5(T)}\right)\end{aligned} \tag{3.69}$$

In (3.69), the temperature dependence is highlighted. In particular, the dependence of the moving coil resistance with the temperature is linear, as follows

$$R_5 = R_5^0(1+\gamma\Delta T) \tag{3.70}$$

where $R_5^0 = \rho_0 l/S$ is the resistance of the winding at room temperature (e.g. 20 °C), γ is the temperature coefficient of resistivity and ΔT is the temperature deviation.

Eq. (3.69) relates the sense coils' voltages with the position and the temperature. In Figure 3.17 (Left), the variation is shown at different positions for illustrative values of dimensions and number of turns. The temperature range is [20 °C, 40 °C], in order to consider consistent variation from the room temperature. The trend is linear for both voltages. In particular, the voltage of the sense winding which is facing the moving coil increases and exhibits a more pronounced variation with respect to the voltage of the winding which is not facing the moving coil, which on the other hand decreases. This dual behaviour creates ambiguity with the normal sensor's functioning: the observed voltage variation can be either due to temperature or to an actual position change of the moving coil. Furthermore, as evident from Figure 3.17 (Left), the voltage drift can attain several millivolts, which often cannot be tolerated.

The effect on the position reading can be also computed. To read the position starting from the voltage amplitudes, the ratiometric reading technique can be used in order to guarantee high-precision reading (the properties of the ratiometric technique have been discussed in Chapter 2). The sensitivity of the ratiometric ratio (often referred to as simply "ratiometric") to the temperature is depicted in Figure 3.17 (Right) for different positions. Once again, the relation is rather linear and the slope depends on the current position.

To calculate the measured position from the ratiometric, a multiplication by the sensor's gain (i.e. the slope of the position-ratiometric curve) has to be computed. Typical values of gain for the I2PS

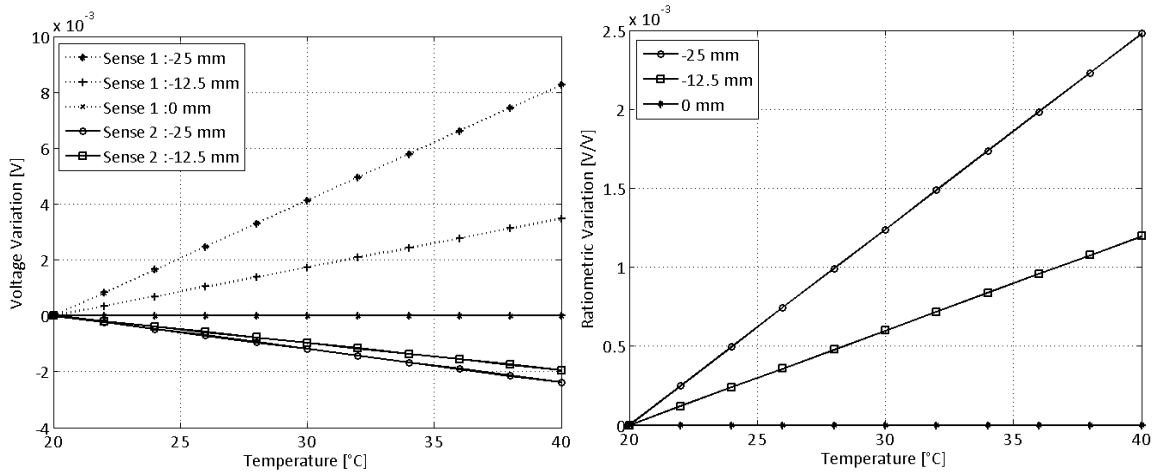

Figure 3.17. Model evaluation of (Left) sense voltage variations and (Right) ratiometric variations due to ambient temperature change at different positions of the moving coil.

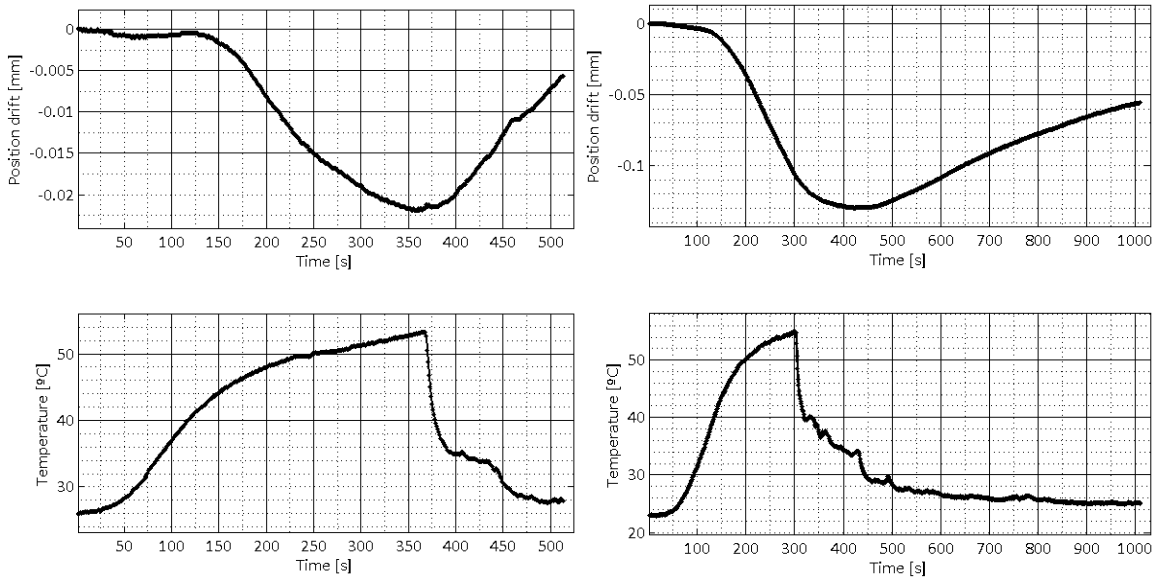

Figure 3.18. Thermal drifts of the position reading for (Left) 2 mm and (Right) 10 mm positions. The position drifts follow the temperature cycles.

are of the order of 200. Therefore, the position sensitivity to ambient temperature can reach values of 500 micrometers over 20 degrees, as clear from Figure 3.17 (Right). This value is unacceptable for high-accuracy applications [15].

Figure 3.18 also shows the results of some experimental measurements which have been performed in a climatic chamber in order to point out the I2PS temperature sensitivity. It can be noticed that the position reading follows the temperature cycle (i.e. the ratiometric is linear with the temperature). The only point where this is not clearly evident is when the temperature drops too fast (i.e. the spatial transient cannot be neglected). In any case, the thermal drifts are quite relevant (e.g. more than 100 micrometers).

It is interesting to notice that even if large variations of the ratiometric with temperature are predicted by the thermal model, the total normalized variation of the ratiometric per unit degree is expected to experience little dependence with the position. In fact, for positions of 25 mm and 12.5

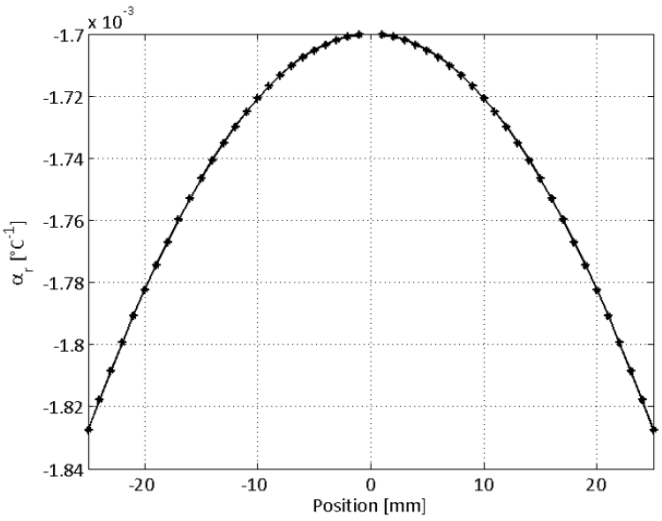

Figure 3.19. Ratiometric normalized variation per unit degree for different moving coil positions. In the null position, the value is not defined.

mm, these values are $-1.83 \cdot 10^{-3}$ °C^{-1}and $-1.73 \cdot 10^{-3}$ °C^{-1} respectively. A more complete overview of this concept is proposed in Figure 3.19, where the factor

$$\alpha_r(p) = \frac{\Delta r}{r_0 \cdot \Delta T} = \frac{r(p, 40°C) - r(p, 20°C)}{r(p,\ 20°C) \cdot \Delta T} \tag{3.71}$$

is calculated for different positions. It can be noticed that the variation of this factor is limited in the moving coil position range (in this case, as an example, [-25 mm, 25 mm]) and the deviation from its maximum value is only 7 %.

The proposed thermal model for the Ironless Inductive Position Sensor points out that the position reading can be seriously affected by ambient temperature variations. This study is a starting point for a compensation algorithm (which will be presented in the next sections) whose aim is to reduce the thermal position drift magnitude and keep it to a small level (compared to the sensor's specifications). The property of the ratiometric normalized variation to experience little dependence with the position has been here shown since it will be the key-assumption for the algorithm development.

3.5. The Reading Technique: Noise Suppression

To demodulate the sense voltages of the Ironless Inductive Position Sensor, the three-parameter Sine Fit algorithm can be used (just as it can be done for Linear Variable Differential Transformers), given its good signal-to-noise ratio and precision [85].

Nevertheless, simulations and experimental measurements (to be presented in this section) have shown that in presence of another sine-wave, the Sine Fit algorithm experiences errors in estimating the main signal amplitude. This algorithm effect (i.e. given by the signal processing, not by the sensor's physics), depends on the second sine-wave amplitude and its frequency and will be addressed here in more detail.

This phenomenon has not been observed in LVDTs since the presence of a second sine-wave gives rise to magnetic phenomena (i.e. dynamic change of the working point on the BH curve of the

materials, hysteresis effects etc., as detailed in Chapter 2) which have totally different origins and play a dominant role for sensors made of magnetic materials, such as LVDTs. On the contrary, being completely free of ferromagnetic materials, this effect becomes important for the I2PS.

The additional sinusoidal signal can be the result of the coupling with the sense winding of an electromagnetic signal coming from the environment (i.e. a low-frequency magnetic field from a current cable or an electro-magnet).

To avoid this disturbing effect, a novel algorithm has been designed, merging the Sine Fit principle with a windowing function, which has been chosen considering the desired specification of reading accuracy and single-tone immunity.

3.5.1. The Sine-Fit Algorithm and the Windowing Technique

The use of the Sine Fit algorithm to demodulate position sensors' voltages is not new [85, 86] and is being used in critical installations [15]. The use of such an algorithm is suggested (compared to a DFT-based one) for better precision [87], even if in coherent sampling conditions, the two algorithms show very similar performances [87]. In general, the three-parameter Sine Fit (3PSF) is preferred to the four-parameter one (4PSF) when the frequency can be easily estimated, since when the number of samples is sufficiently high (e.g. more than 512 with a sampling rate of 100 kS/s), the two algorithms show practically the same precision [88, 89]. Therefore, since the processing burden of the three-parameter algorithm is much less important, this is preferred.

The application of windowing functions on the signal to analyse is also a well-known technique for DFT-based processing, even if such functions result in affecting the signal's amplitude and uncertainty [90]. The design of a proper windowing function, according to the required specifications, is a fundamental step for DFT-based processing. Linearly tapered (e.g. the Bartlett window [91]) or non-linearly tapered (e.g. Blackman or Hann windows [92, 93]) can be used and their parameters can be tuned when possible. The choice of the window type is often the result of a compromise between minimizing the influence of the windowing function on the signal to be processed and maximizing its frequency selectivity [94].

The design and the use of time windows with Sine-Fit-based algorithms are also common in applications like ADC characterization and dynamic testing [95-97].

The three-parameter Sine-Fit algorithm in Linear Variable Differential Transformers' reading is an effective solution in harsh environments, given the good properties of noise-suppression [98, 99] and cross-talk reduction between nearby sensors, as mentioned in Chapter 2. It is possible to derive the amplitude frequency response of the 3PSF algorithm by applying it to a unity sine-wave at different frequencies. An example of such a response is depicted in Figure 3.20 (continuous line), where the specified frequency is f_0 = 1000 Hz, the number of samples is N = 2000 and the sampling frequency is f_s = 250 kS/s. The amplitude is given in the percentage value of the amplitude of the input signal. When the input signal frequency is f_0, the amplitude estimation is correct, whereas it decreases quite rapidly when the input frequency is below or above f_0. The zeros of the main side-lobes are spaced by f_s/N, which is, in this case, 125 Hz. This frequency corresponds to the inverse of the acquisition time. The only exception is at very low frequencies, where the spacing reduces to

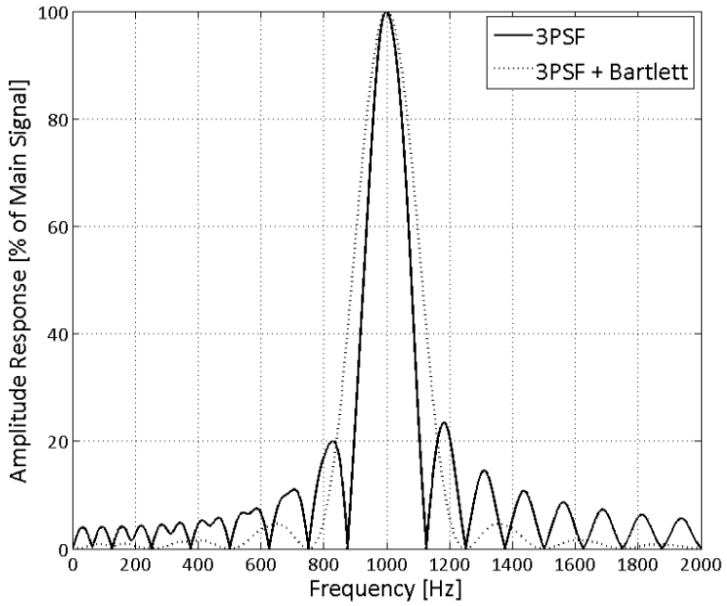

Figure 3.20. Amplitude frequency response of the three-parameter Sine-Fit algorithm and its implementation with a Bartlett windowing function.

half: in this case, the input signal does not accomplish a full period inside the acquisition time window. Analytical expressions of the 3PSF algorithm frequency response can be found in [99].

3.5.2. Amplitude Estimation Error with Multi-Tone Signals

The problem of the performance degradation of the three-parameter Sine-Fit algorithm with additional frequency tones can be verified for several values of number of samples or sampling rate. However, in this section, the problem is shown for a case study in which the number of samples is 2000, the main signal frequency is 1000 Hz and the sampling rate is 250 kS/s. These parameters are good candidates for a real-time position reading on the Ironless Inductive Position Sensor. In practice, this choice is the result of a compromise between algorithm precision and real-time implementation. As a matter of fact, Figure 3.21 shows that the standard deviation of the 3PSF amplitude estimation exhibits smaller values for higher numbers of samples, especially for low signal-to-noise ratios. On the other hand, an acquisition time window that is too large results in greater survey time. With the chosen parameters, a good precision of the 3PSF amplitude estimate is guaranteed even with low Signal-to-Noise Ratio (SNR) and at the same time a survey frequency constraint of at least 100 Hz is respected (one position readout every 10 ms). In addition, the standard deviation of the amplitude estimation is also a function of the signal's amplitude; nevertheless, the value normalized with respect to the amplitude remains constant. However, the analysis can be adapted and repeated also with different values of this parameter set, according to the application.

The presence of an additional frequency tone on the signal to analyse can be easily detected when the two frequencies are harmonically related [100]. Nevertheless, when the frequency of the (one or more) additional sinusoidal signals is not known (i.e. in principle, the ratio between the frequency values can also be non-integer), the 3PSF algorithm can experience important precision degradation when evaluating the frequency tone at f_0.

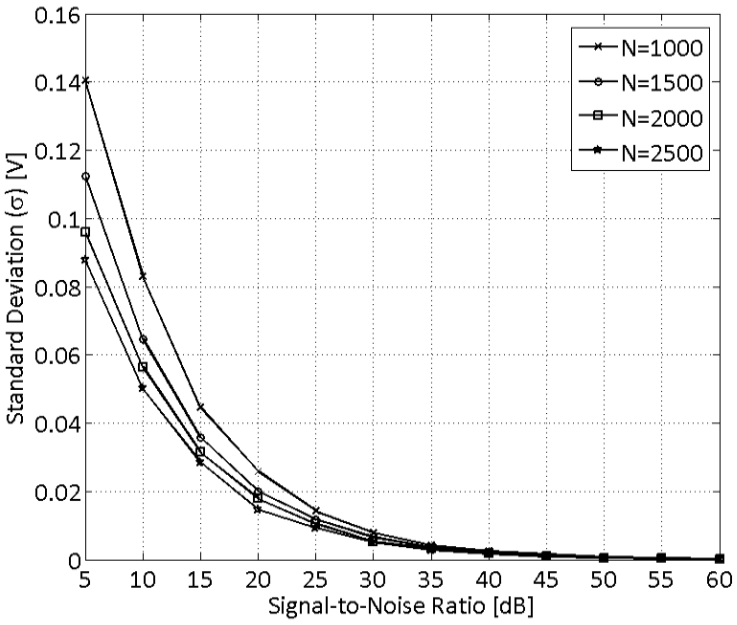

Figure 3.21. Standard deviation of 3PSF amplitude estimate as a function of the input signal SNR for different acquisition buffer size. The sampling rate is 250 kS/s. The standard deviation is computed on 100 repeated estimations. The signal amplitude is 8 V.

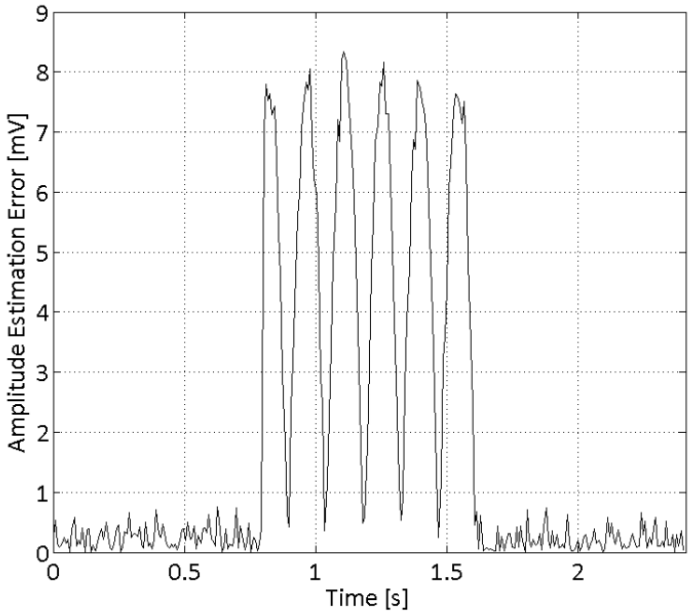

Figure 3.22. Amplitude error (absolute value) of the three-parameter Sine Fit algorithm applied in simulation to an 8-V-peak sinusoid with a superposed 0.1 V sine-wave at 59 Hz between 0.8 s and 1.6 s. A white Gaussian noise (signal-to-noise-ratio of 56 dB) has been added to the signal as well.

Figure 3.22 shows an example where the 3PSF algorithm has been applied on a simulated voltage signal at a frequency of 1 kHz with a superposed second sine-wave at 59 Hz between 0.8 s and 1.6 s. The amplitude of the 1 kHz sine-wave is 8 V (typical value for the Ironless Inductive Position Sensor's or Linear Variable Differential Transformer's applications), whereas the amplitude of the additional 59 Hz disturbing sine-wave is 0.1 V. As mentioned, the 3PSF algorithm has been applied to slices of 2000 samples of the signal. It is evident that when the disturbing sine-wave is not present (i.e. until 0.8 s and after 1.6 s) the amplitude error of the Sine Fit stays around its nominal uncertainty (i.e.

tenths of millivolts, as is predictable from Figure 3.21), whereas when the 59 Hz additional sine-wave is present the estimated amplitude experiences an important drift (i.e. up to 8 millivolts). Such a significant error on the sense voltage amplitudes translates to a drift on the sensor's measured position.

Such a phenomenon has different effects according to the frequency of the disturbing sine-wave and its phase. To characterize these dependencies and trace a starting point for the novel algorithm proposal, a complete analysis has been performed in simulation, sweeping these parameters.

Henceforth, the Sine-Fit amplitude frequency response is intended to be the output of the three-parameter Sine-Fit algorithm when the frequency of the input signal is changing and the disturbing sine-wave is not present (i.e. the continuous line depicted in Figure 3.20). On the other hand, the amplitude frequency response to the disturbance is intended to be the output of the three-parameter Sine-Fit algorithm when the input amplitude and frequency are constant and the frequency of the disturbing sine-wave is changing. In addition, the initial phase of the disturbing sinusoidal signal can also be changed.

Figure 3.23 shows the results of the parametric analysis which gives the amplitude frequency response to the disturbance of the 3PSF algorithm. The graphs show the amplitude error as a percentage of the disturbing sine-wave amplitude. The upper graph shows that for two different phase values the amplitude error distributes differently against the sinusoidal disturbance frequency. This result shows how significantly the phase affects the 3PSF frequency response to the disturbance. The bottom graph shows that the different phases modify the amplitude error response of the 3PSF giving rise to an asymmetric sinc-like envelope. The envelope actually corresponds to the combination of frequency and phase of the disturbance which gives the biggest amplitude error; therefore, it represents the worst case.

The important results coming from this graph are that the amplitude error is globally more relevant when the sinusoidal disturbance frequency is low, rather than for high frequencies; in addition, the envelope produced by the different curves corresponding to the different phase values is characterized by a discrete set of zeros, where the error is null. The interval between the zeros is constant and corresponds to the inverse of the acquisition time (i.e. 125 Hz for the parameters of this case study). Finally, when the sinusoidal disturbance frequency coincides with the main signal one, the amplitude error is maximum.

The results coming from this study show that a frequency tone superposed on the main signal generates, in almost all cases, an amplitude estimation error by the 3PSF algorithm applied at the main signal frequency. The aspect of most significance is the sensitivity to especially low frequency tones as well as frequencies which are far from the main signal one. As a matter of fact, the sensitivity around the main signal frequency is not a big concern, since the sensor's operational frequency can be previously fixed according to the electromagnetic environment.

3.5.3. The Windowed Sine-Fit Algorithm Design

A novel processing algorithm for Ironless Inductive Position Sensor reading is proposed to overcome the described problem of single-tone numerical interference. Since the three-parameter

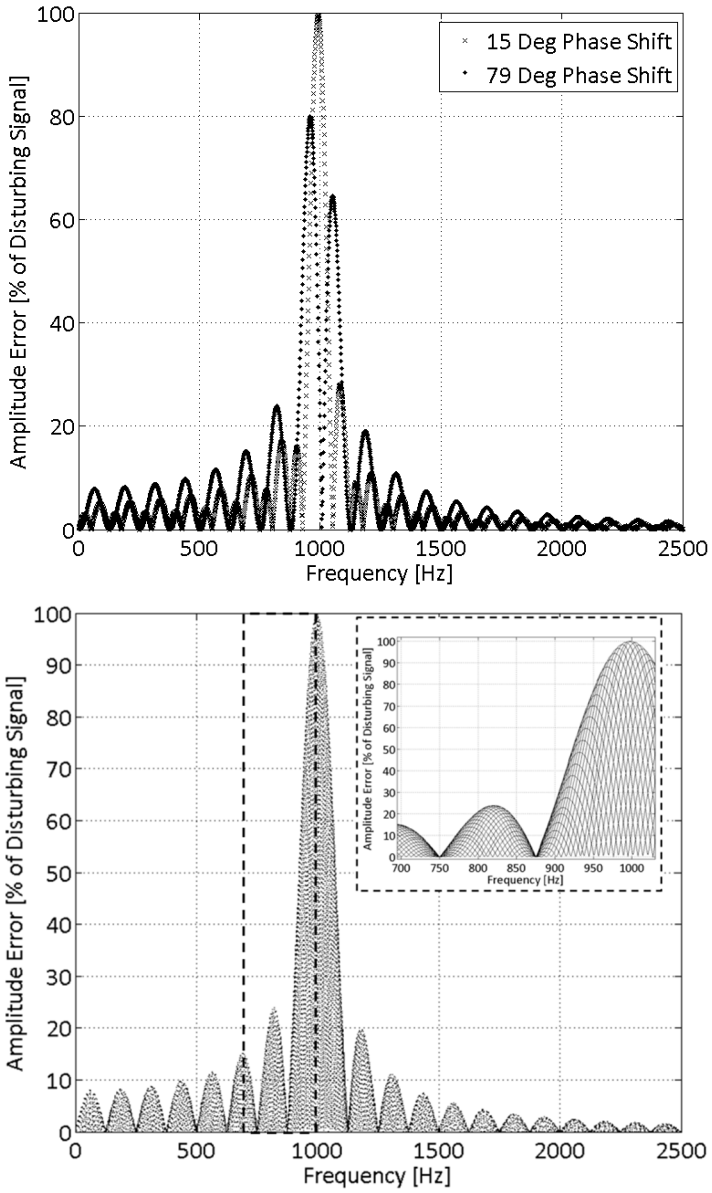

Figure 3.23. Three-parameter Sine-Fit algorithm response to the frequency of the disturbance for (Top) two different phase values (15 and 79 degrees) and for (Bottom) several phase values between 0 and 180 degrees. The dotted square in the bottom graph highlights a part of the traces.

Sine-Fit algorithm exhibits already good white noise immunity, the presented technique remains Sine-Fit-based. Where not specified, the design process has been carried out in simulation.

The novelty of the algorithm is in the use of a combination of the 3PSF algorithm and a designed windowing function for the position reading of the Ironless Inductive Position Sensor. The signal coming from the I2PS sense windings is actually multiplied by the windowing function prior to being processed by the Sine-Fit algorithm. The amplitude of the signal is then adjusted taking into account the gain correction factor of the window [101]. The solution of adopting a windowing function can be justified by looking at Figure 3.23, where it is possible to notice that the frequencies which do not considerably affect the 3PSF amplitude estimation are integer multiples of the inverse of the acquisition time (i.e. 125 Hz). Therefore, a signal with its harmonics placed in these frequency spots would not influence the 3PSF amplitude estimation.

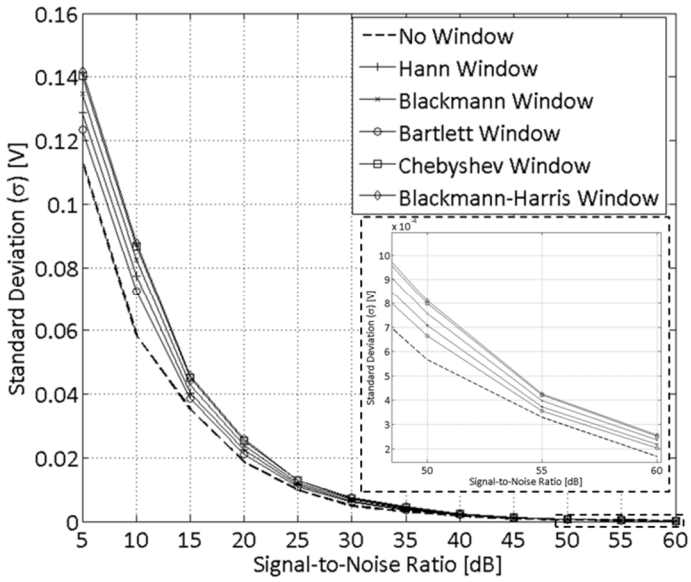

Figure 3.24. Standard deviation of windowing + 3PSF amplitude estimation as a function of the input signal SNR for different windowing function choices. The parameters are given by the case study. The standard deviation is computed over 100 repeated estimations. The dotted square in the bottom highlights a part of the graph for high SNR ratios. The signal amplitude is 8 V.

For very low frequency sine-waves (i.e. signals that does not accomplish an entire period inside the acquisition time), introducing a time window that smoothly connects the endpoints of the signal in the acquisition time renders the signal periodic. Obviously, the multiplication by the time window introduces harmonic distortion of the main signal as well, but its harmonic will be placed in the null spots of the frequency response to the disturbance of the 3PSF. In addition, the more pronounced side-lobe decay of the windows contributes to the rejection of the higher frequency single-tone components as well.

The crucial point of the algorithm design is the choice of the appropriate time window. The final algorithm has to guarantee a limited precision degradation with respect to the standard 3PSF, assure single-tone rejection and at the same time respect the real-time survey frequency constraint. Five different windowing functions have been tested here (Blackman, Hann, Chebyshev, Bartlett and Blackman-Harris windows) and the best-performing (in terms of single-tone rejection and precision) has been chosen.

To compare the algorithm performances with the standard 3PSF one, the same graph type as in Figure 3.21 has been built when different windowing functions are used before the 3PSF. The results are in Figure 3.24, where it is possible to observe the precision achieved by the algorithm using the different windowing choices. In particular, the Bartlett window is shown to be the choice that leads to the least precision degradation (with respect to the standard 3PSF). This result is also summarized in Table 3.2 (precision degradation).

To further stress the algorithm's precision with an additional frequency tone, the standard deviation of the amplitude estimation has been computed with and without a 0.1 V-peak sinusoidal voltage at 7 Hz. White noise (56 dB signal-to-noise ratio) has been also added to the main signal. The choice of the low frequency is justified by the fact that, as is evident from Figure 3.23, the 3PSF is more sensitive to low-frequency single tones, rather than high-frequency ones. In addition the

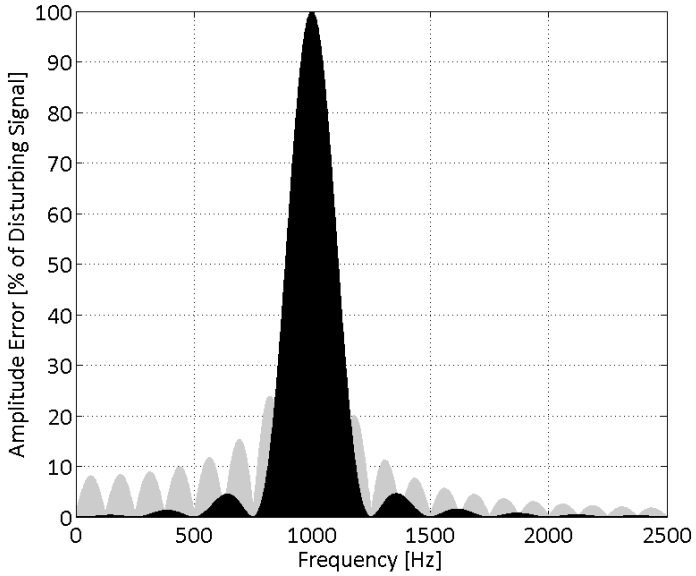

Figure 3.25. Frequency response to the disturbance in the worst case (envelope of the curves at different initial phase values) of (grey) standard 3PSF and (black) proposed Bartlett-windowed 3PSF.

frequency ratio with the main signal is non-integer. The results are summarized in Table 1.1 for the different windowing functions. Once again, the Bartlett window shows the best results, both for standard conditions (i.e. no disturb) and with additional frequency tone.

Finally, the real-time criticality of the algorithm has been investigated by measuring the computational time of the algorithm with the different windows. The result showed that no significant time increase is introduced by any of the windowing functions. Therefore, the 5 windows are equivalent from the real-time implementation viewpoint.

For what has been observed, the Bartlett window is the best-performing solution of the proposed 5 windowing functions. The chosen window has been tested with a sine-wave disturbance at different frequencies, in order to carry out the amplitude frequency response to the disturbance of the whole proposed algorithm, and compare it to Figure 3.23. The results are depicted in Figure 3.25, where it is noticeable that the most concerning components (i.e. very low frequencies and higher frequency with respect to the main signal one) are strongly attenuated, improving the rejection to both low-frequency and high-frequency disturbances. The amplitude frequency response of the chosen algorithm is compared with the standard 3PSF in Figure 3.20 (dotted line), where the side-lobes exhibit a faster decay. However, as a drawback, the signal windowing (with

Window Type	Sigma without disturbance	Sigma with disturbance	Precision Degradation
Hann	60 µV	87 µV	19.6 %
Blackman	63 µV	90 µV	27.6 %
Bartlett	55 µV	80 µV	13.3 %
Blackman-Harris	68 µV	97 µV	37.0 %
Chebyshev	68 µV	97 µV	34.9 %

Table 3.2. Algorithm uncertainty with different windows. The precision degradation is calculated with respect to the standard three-parameter Sine-Fit (i.e. without windowing function).

whatever type of windowing function) always leads to an enlargement of the main lobe of the frequency response (both to the input and to the disturbance), due to the harmonic signal distortion. Nevertheless, as already mentioned, this is not a big concern, given the possibility to choose the sensor's operational frequency.

As a conclusion, the proposed noise-suppression reading algorithm, based on a three-parameter Sine-fitting enhanced with a properly designed window, allows high-precision position reading on the Ironless Inductive Position Sensor even in presence of additional sinusoidal disturbances.

3.6. The Reading Technique: Temperature Compensation

In this section, the temperature compensation algorithm, designed to strongly reduce the thermal drifts caused by the ambient temperature variations on the Ironless Inductive Position Sensor, is presented. The algorithm is designed taking the thermal model described in Section 3.4 as guideline. The complete validation of such an algorithm on a sensor's prototype will be addressed in detail in Chapter 4.

The compensation algorithm presented in this section is based on the following assumptions

- The normalized ratiometric variation per unit degree (i.e. the factor α_r defined in Section 3.4) is constant with the position. It will be shown that this approximation does not significantly affect the algorithm performances.
- The temperature changes are smooth and slow (as in the majority of cases when considering ambient temperature variations), so that the spatial transients can be neglected.
- The effect of thermal expansion on the coils and supports are neglected. Actually, taking into account the values of thermal expansion coefficients for copper (around $17 \cdot 10^{-6}$ °C^{-1}) and radiation-hard plastics (of the order of 10^{-5} °C^{-1}), the thermal expansion would be only of some micrometers each 100 mm over a temperature variation of 20°C.

3.6.1. Smart Temperature Sensing

To solve the ambiguity problem due to the temperature sensitivity of the Ironless Inductive Position Sensor reading and exploit at best the model results discussed in Section 3.4, a temperature reading has to be performed. In particular, a measure of the average temperature along the entire coil assembly would be the best option, since it will represent the sensor's current operational temperature. A temperature sensor (e.g. a PT100 [18]) could in principle be a first solution, but this approach presents serious drawbacks as

- Increase of sensor's radial dimensions, due to the presence of one (or more) temperature probes. This is a crucial point for applications where limited space is available for the sensor's installation.
- Increase of sensor's wire terminals, since each temperature sensor would need 2 (or even 4) wires to work properly. This can represent a serious drawback when multiple sensors are installed in the same environment [14, 15].
- Measurement of a punctual value of temperature, whereas a global mean value of temperature along the sensor's length would be ideal.

For these reasons, this solution is discarded as inefficient. A more effectual way to sense the mean temperature can be obtained by superposing a DC offset to the AC supply current. In this way, the DC part of the consequent supply voltage will be directly proportional to the mean temperature along the sensor, since it will be proportional to the supply coils' resistance, which is affected by the temperature according to a relation similar to (3.70), giving

$$V_{DC} = R_s I_{DC} = R_S^0(1 + \gamma \Delta T) I_{DC} = V_{DC}^0 + g_{DC} \Delta T \tag{3.72}$$

where I_{DC} is the DC current superposed to the AC supply signal, R_s is the supply resistance and R_S^0 its value at room temperature (e.g. 20°C). Furthermore, the DC signal on the supply coils would not be reflected on any of the other windings (as a consequence of Faraday's law). In this way, a measurement of the average temperature is performed with no influence on sensor's dimensions, wire terminals and proper electromagnetic functioning. Finally, even though the temperature measurement is performed on the supply windings, the value can be considered as a mean temperature along the entire sensor, since spatial transients are absent by hypotheses.

3.6.2. Compensation Algorithm

Assuming α_r to be a constant with the position (i.e. accepting a slight compensation error), the following relations are valid

$$\begin{gathered} \frac{\Delta r}{r_0 \cdot \Delta T} = \alpha_r = const \\ r(T) = r_0 + \Delta r(T) = r_0 + \alpha_r r_0 \Delta T \end{gathered} \tag{3.73}$$

where r_0 is the value of ratiometric at the room temperature (e.g. 20 °C). Eq. (3.72) can be substituted in (3.73)

$$r(T) = r_0 + \alpha_r r_0 \frac{\Delta V_{DC}(T)}{g_{DC}} = r_0(1 + \zeta \cdot \Delta V_{DC}(T)) \tag{3.74}$$

where $\zeta = \alpha_r / g_{DC}$ $[V^{-1}]$ is the correction factor (expected to be negative) and $\Delta V_{DC} = V_{DC}(T) - V_{DC}^0$ is the variation of the DC voltage due to the temperature. Finally, the compensation relation can be extracted from (3.74), giving

$$r_0 = \frac{r(T)}{(1 + \zeta \cdot \Delta V_{DC}(T))} \tag{3.75}$$

Therefore, applying (3.75) on the acquired ratiometric $r(T)$ under the abovementioned hypotheses, a compensation of the thermal effects due to ambient temperature variations can be performed. To extract the position, the compensated ratiometric has to be multiplied by the gain

$$p = \frac{g}{(1 + \zeta \cdot \Delta V_{DC})} \cdot r \tag{3.76}$$

The compensation process can thus be seen as a correction of the sensor's gain, whose deflection is due to the temperature variation. The value of g in (3.76) is calculated from the sensor's calibration at the reference temperature.

It is now clear that the first of the two hypotheses mentioned at the beginning of the section is crucial and mandatory for the compensation to be actually feasible. This assumption is actually possible since it has been shown in Section 3.4 that α_r exhibits little dependence with the position. Nevertheless, if the position dependence of α_r had been taken into account, this would certainly

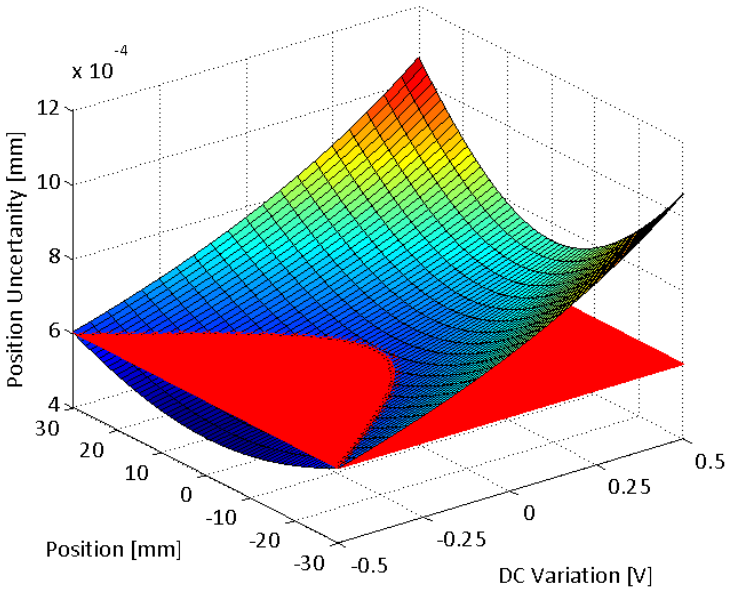

Figure 3.26. Position uncertainty after temperature compensation with different values of DC voltage and for different moving coil positions. The red plateau is the default position uncertainty (supposed to be constant for sake of simplicity), dependent just on the ratiometric. The default ratiometric uncertainty adopted is 10^{-6}, the value of ζ is -0.4.

have led to a more accurate compensation, but on the other hand would have necessitated the knowledge of the current position (to return the correct value of α_r to apply). Nevertheless, this information cannot come from the sensor's position reading (since it is on turn affected by temperature) and therefore an additional position sensor would be necessary, nullifying the need of the compensation algorithm itself.

3.6.3. Position Uncertainty

The proposed compensation algorithm involves the reading of an additional signal: the DC voltage on the supply windings. Therefore, the position reading uncertainty does not depend anymore just on the sense voltages' reading precision, but also on the reading uncertainty of this new signal. From (3.76), the sensitivity coefficients associated to the ratiometric and the DC voltage can be calculated as

$$\frac{\partial p}{\partial r} = \frac{g}{1+\zeta\cdot\Delta V_{DC}},\quad \frac{\partial p}{\partial V_{DC}} = -g\cdot\frac{r\cdot\zeta}{(1+\zeta\cdot\Delta V_{DC})^2} \tag{3.77}$$

Therefore, the uncertainty propagation law can be applied in order to find the position reading uncertainty after applying the compensation algorithm, as follows

$$u(p) = g\cdot\sqrt{\frac{1}{(1+\zeta\cdot\Delta V_{DC})^2}\cdot u^2(r) + \frac{r^2\cdot\zeta^2}{(1+\zeta\cdot\Delta V_{DC})^4}\cdot u^2(\Delta V_{DC})} \tag{3.78}$$

where $u(r)$ and $u(\Delta V_{DC})$ are the uncertainties associated with the ratiometric and the DC signal on the supply windings. Figure 3.26 shows the position reading uncertainty calculated above as a function of the DC voltage variation (which can be positive or negative, according to the temperature gradient) and moving coil position for illustrative valued of ζ and ratiometric uncertainty. The resulting function is compared to the nominal reading uncertainty (red plateau), which depends just on the ratiometric and on the sensor's gain. It is evident that the uncertainty

does not experience tremendous deviations even with unlikely DC voltage variations. Regarding the design, the DC signal to apply on the supply windings has to be chosen in order to have remarkable DC signal amplitude (so as to have better uncertainty on the reading of V_{DC}).

The effectiveness of the proposed compensation algorithm will be discussed in detail in Chapter 4, where experimental measurement campaigns will be performed to extract the values of α_r and ζ.

3.7. Design Optimization

In Sections 3.2, 3.3 and 3.4 the modelling of electromagnetic and thermal phenomena taking place on the Ironless Inductive Position Sensor has been presented in detail. Such models are useful tools for the study and the design of the sensor: they actually explain the physics of the Ironless Inductive Position Sensor functioning, but they also can give important feedbacks in terms of design choices (e.g. supply type, dimensions etc.) and act as basis for the optimization.

In this section, the design optimization process of the sensor is drawn, having the models equations as reference. The optimization of an actual I2PS prototype will be performed in Chapter 4.

3.7.1. The Design Parameters and Constraints

From the electromagnetic model (in particular, from equations (3.16) and (3.23)), it is possible to extract the design parameters for the sensor, defined as those quantities (geometrical, physical or dimensionless) that can be tuned in order to achieve a certain performance of the device.

For the Ironless Inductive Position Sensor, since all the operational specifications listed in Chapter 2 are already met, the required performance would be to maximize the sensitivity, keeping the sensor's dimensions under the limits of common Linear Variable Differential Transformers' ones. This requirement translates to the maximization of the ratiometric swing (i.e. the value of the ratiometric at one of the two extreme positions), since the ratiometric reading technique is used to perform the position reading.

The design parameters are:

- r_c : inner radius of the moving coil. The limits of variation for this parameter are given by the maximum radial space occupancy of the moving coil.
- a_C : moving coil semi-length. The limits of variation of this parameter are in principle open.
- a_P : supply winding semi-length. The limits of variation of this parameter are given by the desired maximum total length of the sensor.
- a_S : sense winding semi-length. The limits of variation of this parameter are given by the desired maximum total length of the sensor.
- N_c : number of turns of the moving coil. It can be decomposed in number of turns per layer (N_{ec}) multiplied by the number of layers (N_{lc}).
- N_p : number of turns of the supply coils. It can be decomposed in number of turns per layer (N_{ep}) multiplied by the number of layers (N_{lp}).
- N_s : number of turns of the sense coil. It can be decomposed in number of turns per layer (N_{es}) multiplied by the number of layers (N_{ls}).

- d_{wc} : diameter of the moving coil wire. The limits of variation of this parameter are given by the maximum radial dimensions of the sensor and by thermal stability.
- d_{wp} : diameter of the supply coil wire. The limits of variation of this parameter are given by the maximum radial dimensions of the sensor and by thermal stability.
- d_{ws} : diameter of the sense coil wire. The limits of variation of this parameter are given by the maximum radial dimensions of the sensor.
- f_0 : operational frequency. The limits of variation of this parameter depend on the wire diameters and on the number of turns and they are given by high-frequency phenomena.
- I or V : supply signal amplitude (either current or voltage). The limits of variation of this parameter are given by the acquisition and readout system and by thermal stability.

In practice, the choice of these parameters completely defines the sensor. In addition, given that all of them play a role in the electromagnetic characteristics, their choice also defines the sensor's performances.

Regarding the supply type, the main constraint for this choice is given by the thermal stability (as explained in Section 3.4). Basically, given the sensitivity of electrical resistance to ambient temperature variations, the supply signal should be a current sine-wave. This is anyway a design choice that can be adapted to the environment (it can be changed whether the expected operational conditions of the sensor are not critical from the thermal point of view, for example in closed spaces with very little temperature variations).

3.7.2. The Optimization Procedure: parameters sub-set

The number of design parameters listed in the last subsection makes the optimization process non-trivial. Some of them are even inter-dependent, so that the influence on the objective function (i.e. the magnitude to maximize/minimize in the optimization process) cannot be in principle estimated considering them one by one (e.g. if the winding length is fixed, the number of turns per layer will depend on the wire diameter and vice versa). In addition, as explained in Section 3.2, the evaluation of the objective function involves the numerical computation of elliptic integrals of first and second kind, as well as non-linear operations (as the complex modulus, or the ratiometric computation). Last but not least, several parameters are not defined in the entire real (or complex) axis, but they rather admit only integer values (e.g. the number of layers), leading to integer optimization problems, which are hard to solve [102, 103]. All these circumstances make a simple optimization run (i.e. an automatic algorithm that searches for the maximum or minimum of the objective function [104]) an ineffective and time-consuming choice.

Anyway, an optimization procedure can be prepared by inter-linking some of the design parameters (e.g. imposing equal length for the supply and sense coils) for geometrical or linearity reasons, so as to decrease the number of unknown, or imposing first the most critical constraints (e.g. thermal stability) and then optimizing the new parameters sub-set.

The optimization procedure which is here presented considers the current supply case and takes as objective function the ratiometric of the sensor at one of its extreme positions. This method is not the only one which can be used for optimizing the device structure. For what has been said, the first

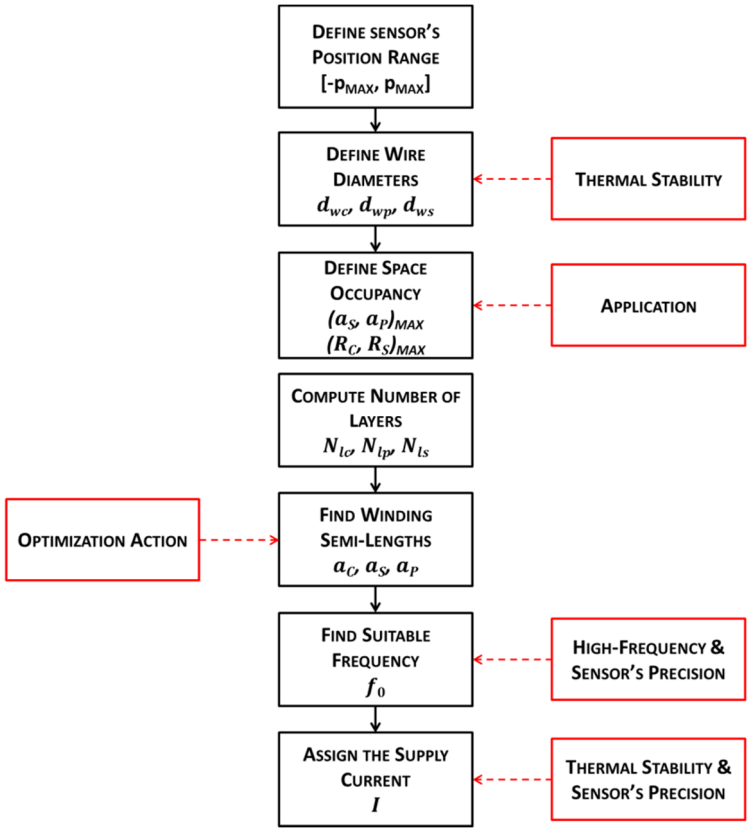

Figure 3.27. Optimization procedure adopted for the Ironless Inductive Position Sensor.

specification to fix for the device's optimization is the position range [$-p_{MAX}$, p_{MAX}] (as in Figure 3.27).

As second step, the wire diameters should be chosen, in order to have good thermal stability of the windings (i.e. as explained in Section 3.4). In particular, in the case of the moving coil, the wire diameter should be chosen in order to have the least resistance (i.e. maximize the induced current in the coil) according to the space constraints.

As successive step, the radial and longitudinal dimensional constraints (which depend on the application) have to be considered to determine the upper bounds of the windings' radii and lengths. From the electromagnetic model's equations, one can notice that the sensor's performances increase when the windings' cross section areas increase, so the target radial dimensions should be as close as possible to the bounds. Therefore, knowing the coil radii and the wire diameters, the number of layers can be computed.

At this point, the initial parameters' set listed in the last sub-section has been significantly reduced. The crucial parameters for the sensor's design reveal to be the winding lengths (which will set the number of turns per layer, and therefore the total number of turns for each winding).

3.7.3. The Optimization Procedure: optimal winding lengths

The optimization action deals with the winding length of the three coil types (i.e. moving coil, supply and sense coils). The main objective of this action is to reduce the number of parameters of the optimization problem, exploiting the electromagnetic model.

From Figure 3.6 it is evident that there exists a position for which the sense voltage exhibits a maximum. The presence of this maximum inside the moving coil position range leads to an increase

of the non-linearity of the device (i.e. the voltages are not always dual and monotonic). For this reason, such a maximum should be kept as far as possible from the null point. The ideal would be to relegate it outside the desired position range. To do that, the derivative of the modulus of the sense voltages has to be computed. Referring to equations (3.16), writing $\underline{Z}_5$ as $R_5 + j\omega L_5$ and taking the supply current $\underline{I}$ as reference for the phases, the modulus of one of the sense voltages is

$$\left|\underline{V}_3\right| = \\ = \sqrt{\left[\omega \underline{I}(M_{31} - M_{32}) - \frac{\omega^3 \underline{I} \cdot L_5}{\left|\underline{Z}_5\right|^2} \cdot M_{35}(M_{51} - M_{52})\right]^2 + \left[\frac{\omega^2 \underline{I} \cdot R_5}{\left|\underline{Z}_5\right|^2} \cdot M_{35}(M_{51} - M_{52})\right]^2} \tag{3.79}$$

whereas the derivative with respect to the position, taking into account that all mutual inductances involving the moving coil (i.e. winding *5*) are position-dependent, is

$$\frac{\partial \left|\underline{V}_3\right|}{\partial p} = \frac{\frac{\partial f(M)}{\partial p} \cdot \frac{\omega^3}{\left|\underline{Z}_5\right|^2}[f(M) - L_5(M_{31} - M_{32})]}{\sqrt{\left[(M_{31} - M_{32}) - \frac{\omega^2 L_5}{\left|\underline{Z}_5\right|^2} \cdot f(M)\right]^2 + \left[\frac{\omega R_5}{\left|\underline{Z}_5\right|^2} \cdot f(M)\right]^2}} \tag{3.80}$$

where $f(M) = M_{35}(M_{51} - M_{52})$. To find the maximum of $\left|\underline{V}_3\right|$, one of the following relations has to be satisfied in (3.80)

$$\frac{\partial f(M)}{\partial p} = 0 \\ f(M) = L_5(M_{31} - M_{32}) \tag{3.81}$$

The second condition in (3.81) is impossible. In fact, $f(M)$ is by definition the product between two factors which are position dependent (M_{35} and the difference between M_{51} and M_{52}). In particular, as seen in Section 3.2 (in Figure 3.4), the mutual inductances involving the moving coil exhibit linear dependence with the position. Therefore, $f(M)$ should exhibit a quadratic dependence on the position. On the other hand, the second condition in (3.81) says that $f(M)$ should be a constant function (none of the parameters in the second term is position-dependent), which is an absurd.

Therefore, the first condition in (3.81) has to be satisfied in order to find the maximum of the sense voltage. This means that the following relation has to be imposed (the position dependence is highlighted)

$$\frac{\partial [f(M)]}{\partial p} = \frac{\partial}{\partial p}[M_{35}(p) \cdot (M_{51}(p) - M_{52}(p))] = 0 \tag{3.82}$$

Given the linear dependence of the mutual inductances with respect to the position and their symmetry with respect to the null-point, they can be generically written as

$$M_{35}(p) = a + bp, \qquad M_{51}(p) = c + dp, \qquad M_{52}(p) = c - dp \tag{3.83}$$

where a, b, c and d are constants. Imposing (3.82), one can find that the position at which the sense voltage exhibits its maximum value is

$$p^* = -\frac{a}{2b} \tag{3.84}$$

Thus, this value depends just on the mutual inductance M_{35} and on its position dependence.

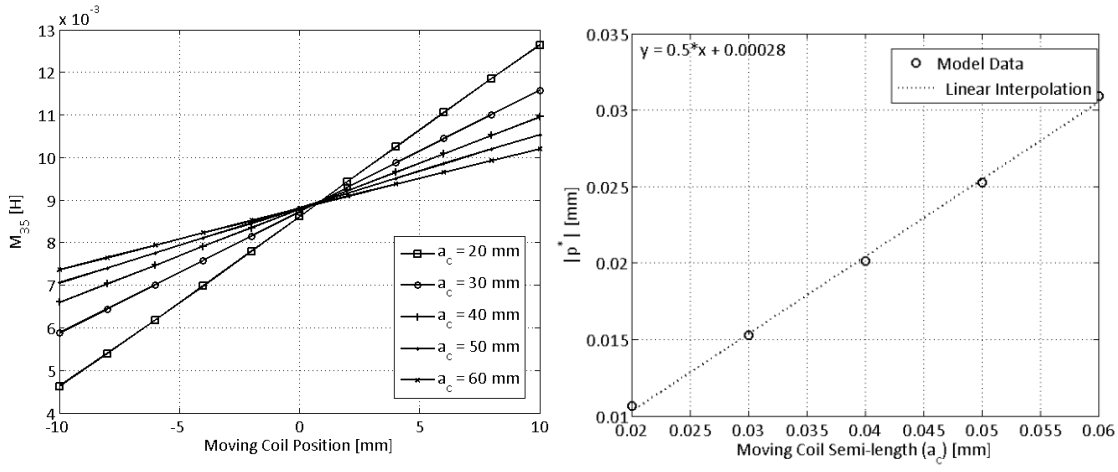

Figure 3.28. (Left) Computation of the mutual inductance M_{35} and (Right) its ratio between the polynomial factors for different values of the moving coil semi-length a_c. The value of a_s and a_p is 40 mm. A 1-mm spacer between the windings has been considered. The number of turns is 3150, 4500, 1400 for the moving, sense and supply coils respectively. The equation on the graph on the right highlights the equation of the linear interpolation.

The value of p^* can be related to the moving coil semi-length a_C. If p^* is calculated for several values of a_C, it is possible to observe that the voltage maximum always occurs in the position

$$p^* \approx -\frac{a_C}{2} \tag{3.85}$$

The demonstration is shown in Figure 3.28, where the mutual inductance M_{35} and the value of (3.84) without sign are computed for different values of a_C and illustrative values of other parameters. Figure 3.28 (Right) also shows the linear interpolation of the model data, which gives a slope of 0.5 and a negligible offset, confirming (3.85).

Therefore, once (3.85) has been demonstrated, the following design rule can be followed in order to keep the voltage maximum away from the desired position range

$$a_C \geq 2p_{MAX} \tag{3.86}$$

Values of a_C smaller than $2p_{MAX}$ but anyway not far from the limit given by (3.86) may be also chosen for space occupancy reasons and accepting a slightly more pronounced non-linearity.

Regarding the supply and sense coils, the design choice

$$a_S = a_P \tag{3.87}$$

can be adopted for symmetry and manufacturing purposes. The design process thus focuses on a_C and a_S (the number of turns per layer can be computed afterwards). The optimal values can be found following two techniques

- Calculate the ratiometric at p_{MAX} from (3.16) and run an automatic optimization process (e.g. using genetic algorithms, in order not to find local maxima [105]) to maximize the value of the ratiometric.
- Calculate the ratiometric at p_{MAX} from (3.16) for different values of a_C and a_S in their boundaries and plot it as a surface. Identify the area of maximum sensitivity.

Both techniques give the same result, even though the second is faster. The dependence of the ratiometric on a_C and a_S is shown in Figure 3.29. It is clear that the locus which gives the maximum sensitivity (i.e. maximum absolute value of the ratiometric) is around the line

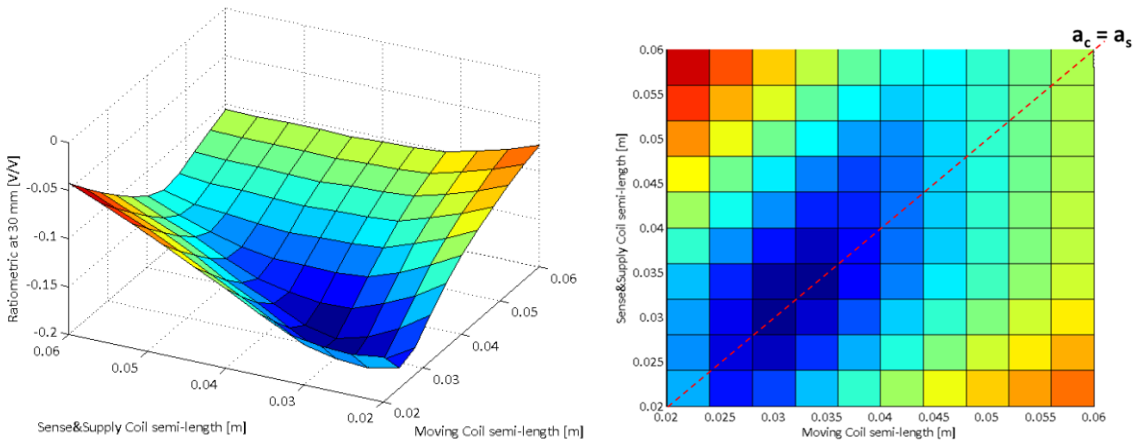

Figure 3.29. Computation of the ratiometric at 30 mm for different values of a_c and a_s. (Left) 3D surface plot. (Right) Projection from the top. The area around the dotted line individuating the choice $a_c = a_s$ gives the best sensitivity.

$$a_S = a_C \tag{3.88}$$

as also highlighted in the top view in Figure 3.29 (Right). Nevertheless, for big values of a_S, a_C can be chosen smaller, since the optimum slightly deviates from (3.88) in this region. In addition, it is worth noticing that the ratiometric exhibits big values (in modulus) for small winding semi lengths (< 35 mm). Nevertheless, when the semi-lengths become too small, the calibration curve of the sensor is not monotonic (i.e. it is not possible to extract the position).

In conclusion, at this stage all the dimensional parameters of the optimization problem can be found and their values optimized within the boundaries.

3.7.4. The Optimization Procedure: experimental tuning

At this point of the design, all the parameters of the coils are found (the number of turns per layer can be calculated knowing the winding length and the wire diameter). The only missing magnitudes are the operational frequency and the supply signal's amplitude. The former can be found with an experimental campaign on a prototype with the optimized dimensions, in order to determine the resonance frequency and choose a frequency which is below this value. In addition, a preliminary study has to be performed in order to determine from which frequency the skin and proximity effects starts affecting the moving coil's resistance[10]. Last but not least, it has to be pointed out that with higher frequencies the precision gets higher, since the acquired samples present more periods of the signal sine-wave, leading to a better amplitude estimation by the three-parameter Sine-fit algorithm.

Finally, the supply current amplitude can be chosen taking into account the thermal stability (current densities smaller than 4 A/mm^2 are preferred, in order not to give rise to much internal heat generation) and the precision (with higher amplitudes, the signal-to-noise ratio increases, and so the uncertainty on the signal's amplitude estimation, as explained in Section 3.5).

The amplitude of the sense voltages is increasing as both the operational frequency and the supply current's amplitude increase. Therefore, these two parameters are interconnected with a common constraint: they have to be chosen not to have a sense voltage amplitude which outgoes

[10] With current supply, that of the moving coil is the only resistance which enters the model's equations.

the limits of the readout system (often, this means an amplitude not bigger than 10 V) in any of the positions of the desired range.

3.7.5. Other optimization methods

The proposed optimization procedure for the Ironless Inductive Position Sensor is a useful tool to design the device. However, it assumes current supply and ratiometric reading technique for extracting the position. In addition, the objective function is the device's sensitivity. For these reasons, it is not the only method which can be adopted.

Other optimization techniques may be focused on the maximization of the voltage swing (i.e. the maximum difference between the sense voltages) or the position range. Therefore, the proposed optimization procedure has to be taken as an example of smart design based on the sensor's electromagnetic and thermal models.

In the next Chapter, the optimization procedure described in this Section will be used to design a sensor's prototype for a specific application.

Innovative Contribution of the Chapter and Related Publications

The Ironless Inductive Position Sensor is presented as an alternative solution to Linear Variable Differential Transformers when external magnetic fields are present. The complete model of the sensor is described, from the low-frequency analysis of the working principle to the high-frequency electromagnetic effects modelling (skin and proximity effects). A thermal model of the sensor is also presented, together with an effective algorithm to compensate the position drifts due to ambient temperature variation. An innovative high-precision reading technique to extract the measured position avoiding classical Sine-fit issues is also described in detail. Finally, an optimization procedure is drawn in order to perform the optimal design of the sensor, maximizing the sensitivity taking into account the space, thermal and high-frequency constraints.

1. A. Danisi, A. Masi, R. Losito, Y. Perriard: "*High-Frequency Electromagnetic Effects Modelling of an Ironless Inductive Position Sensor*", submitted to IEEE Transactions on Magnetics, October 2012.

2. A. Masi, A. Danisi, M. Di Castro, R. Losito: "*Real-Time High-Precision Reading Algorithm for an Ironless Inductive Position Sensor*", submitted to IEEE Transactions on Nuclear Science, July 2012.

3. A. Danisi, A. Masi, R. Losito, Y. Perriard: "*Electromagnetic Analysis and Validation of an Ironless Inductive Position Sensor*", submitted to IEEE Transactions on Instrumentation and Measurement, June 2012.

4. A. Danisi, A. Masi, R. Losito, Y. Perriard: "*Modelling and Compensation of Thermal Effects on an Ironless Inductive Position Sensor*", proceedings of ECCE 2012, Rayleigh, North Carolina, September 2012.

5. A. Masi, A. Danisi, M. Di Castro, R. Losito: "*High Accuracy Reading Algorithm for Ironless Linear Position Sensor*". Proceedings of IEEE Real Time Conference 2012, Berkeley, California, June 2012.

6. A. Danisi, A. Masi, R. Losito, Y. Perriard: "*Electromagnetic Modeling of an Ironless Position Sensor*". Proceedings of IEEE I2MTC 2012, Graz, Austria, May 2012.

Chapter 4

Numerical and Experimental Validation

Abstract

In this chapter, the complete validation of the sensor's models and reading techniques is discussed. The electromagnetic model of the working principle is fully validated in simulations and also compared to the results of experimental measurements on the optimized prototype. The high-frequency model is verified with experimental measurements. The reading techniques are experimentally tested in a climatic chamber (for the temperature compensation) and on a real-time target (for the noise-suppression). Finally, the optimization of the sensor is performed taking into account the operational constraints of the CERN's LHC Collimators application and the results are shown.

4.1. The Validation Means

The models presented in Chapter 3 have been validated both with numerical and experimental techniques. In this Section, a brief description of these techniques is proposed.

4.1.1. The Sensor's Finite Element Model

A Finite-Element (FE) model of the Ironless Inductive Position Sensor has been built using the simulator FLUX® [55] in the 2D environment: given the cylindrical symmetry of the geometry in terms of magnetic and electrical fields, this environment is ideal for performing the analysis.

FE simulations are the best mean to perform the validation of the low-frequency electromagnetic model, since in the simulated structure there is no influence from other physical quantities (e.g. temperature). Of course, the simulator takes into account the parasitic effects due to capacitances, therefore the supposition (advanced in the model) to neglect them can be also verified. Finally, Finite Element Method (FEM) is widely used for validation of theoretical models and design of electromagnetic position sensors [106, 107], since it allows the investigation on physical quantities which are otherwise difficult to measure (e.g. the induced current in the moving coil, in the case of an I2PS). For these reasons, the validation through FEM simulations will concern mainly the currents in the windings (especially the moving coil) and the supply voltages, basically to validate the soundness and reliability of the model.

For the geometry and dimensions, no optimization has been done yet, since the only aim of the simulations is to validate the analytical model. The optimization is a later stage. Half of the longitudinal section (Figure 4.1) has been simulated. The longitudinal axis of the device represents the simulation domain boundary (together with the infinite), in which a condition of symmetry has to be imposed (in this case, tangential magnetic field). The open space is reconstructed with an infinite box (already introduced in Chapter 2), where the conditions of null field are assigned.

Since the geometry of the device is mainly along the axis (high ratio between length and diameter), a fine mesh has been set up. In principle, the number of mesh elements can be reasonably high, since in the solving process the non-linear solver will be bypassed (all B-H curves are linear) and thus the computational time is not a significant concern.

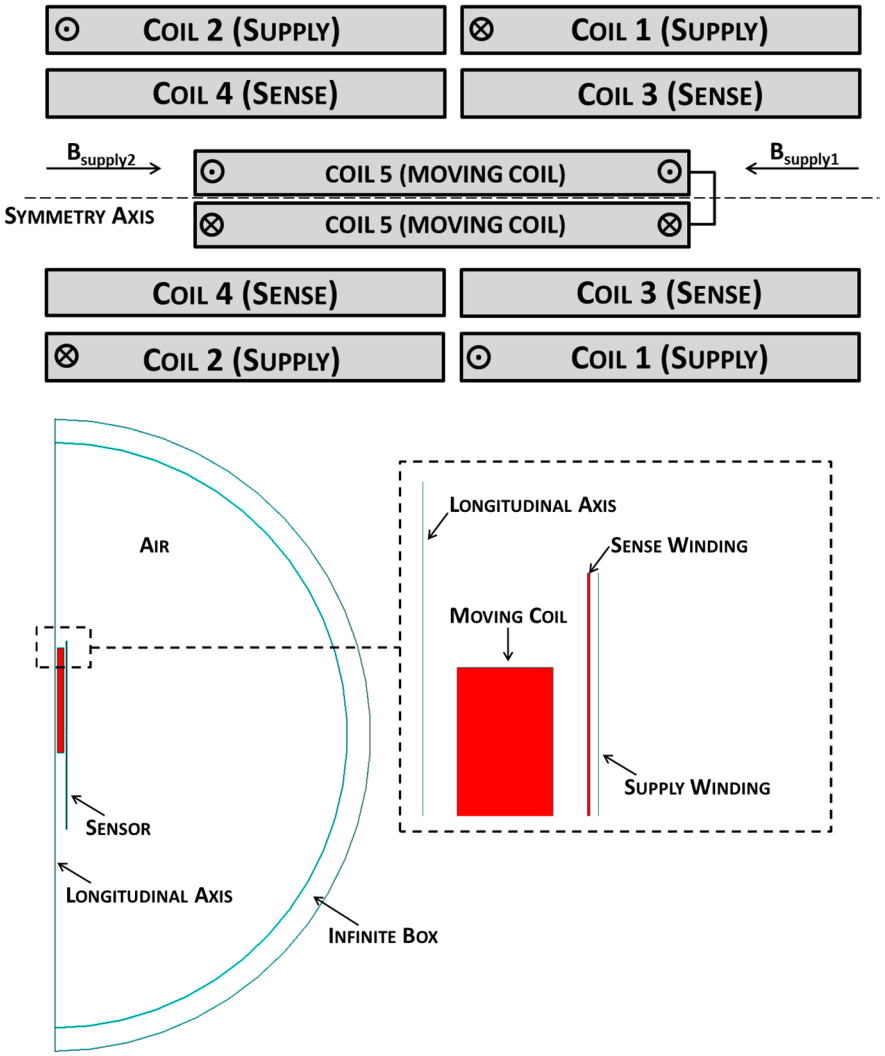

Figure 4.1. (Top) Longitudinal section of the Ironless Inductive Position Sensor with indicated the directions of the flux densities produced by the supply windings. (Bottom) 2D axisymmetric reconstruction of the sensor for the FEM simulations (on one side, a zoom of the upper part is depiced).

The windings' sections have been modelled with solid rectangular windows, without taking into account the single wire cross sections. However, a fill factor can be specified [55]. The coils support has been modelled with non-magnetic and non-conductive materials. Among all the elements of the simulation structure, the only electrically conducting materials are the 5 windings, as required for the validation of the model.

The supply of the sensor has been performed through an electrical network simulator, coupled with the FEM software and embedded in it. The supply circuits have been described in Chapter 3 and are depicted in Figure 3.1.

4.1.2. The Sensor's Prototype and the Test Bench

For the experimental validation, a prototype of Ironless Inductive Position Sensor has been manufactured and tested on a proper test bench. The winding parameters and dimensions have been optimized using the procedure described in Chapter 3 and based on the application requirements of the LHC Collimators (already described in Chapter 2); the optimization process will be discussed in detail in the next sections. However, the validation of the high-frequency model and

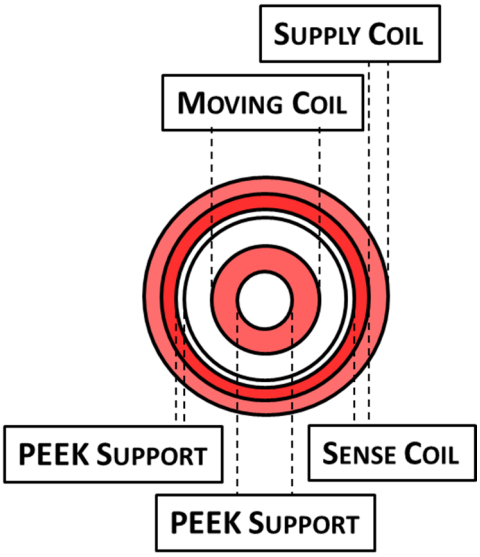

Figure 4.2. Transversal view of the winding and arrangement of the Ironless Position Sensor Prototype.

the reading techniques has been carried out on a sensor prototype with non-optimized parameters, since the validation of the theoretical part has been performed before the optimization step and anyway does not require an optimization.

The winding support of the coils is made of Polyether ether ketone (PEEK) [108], a non-magnetic and non-conductive material which is suitable for radiation environments [109]. The two supply windings have been wound in opposite directions, so as to give rise to opposite magnetic fields. The winding assembly is shown in Figure 4.2. The coils have been insulated with Kapton polyimide. The prototype presents 8 wires for the connections (2 per coil), but the number can be reduced to 6 if current supply is adopted (the two supply coils are then connected in series).

In principle, the prototype can be enclosed in a cylindrical case made of high-resistivity steel (as in Figure 4.3). To strengthen the structure from the mechanical viewpoint, resin can be used to coat the moving coil and fill the space between the coils and the case. If this last operation is done, it is not possible anymore to remove the prototype from the case. For the experimental validation, the

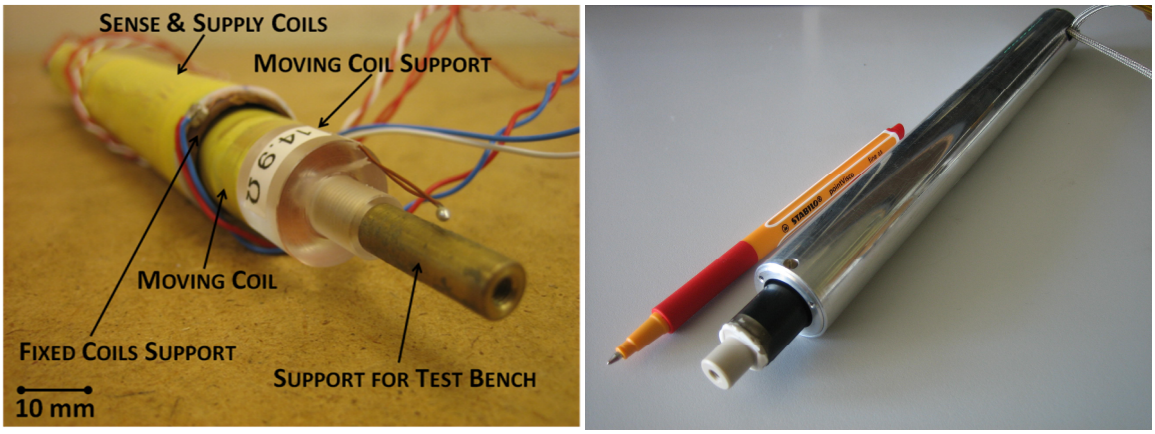

Figure 4.3. (Left) Ironless Inductive Position Sensor prototype structure. In this photograph, the moving coil support is made of plastics. (Right) Example of final assembly of the prototype. The external case is made of steel and the moving coil is coated with resin in order to strengthen the structure.

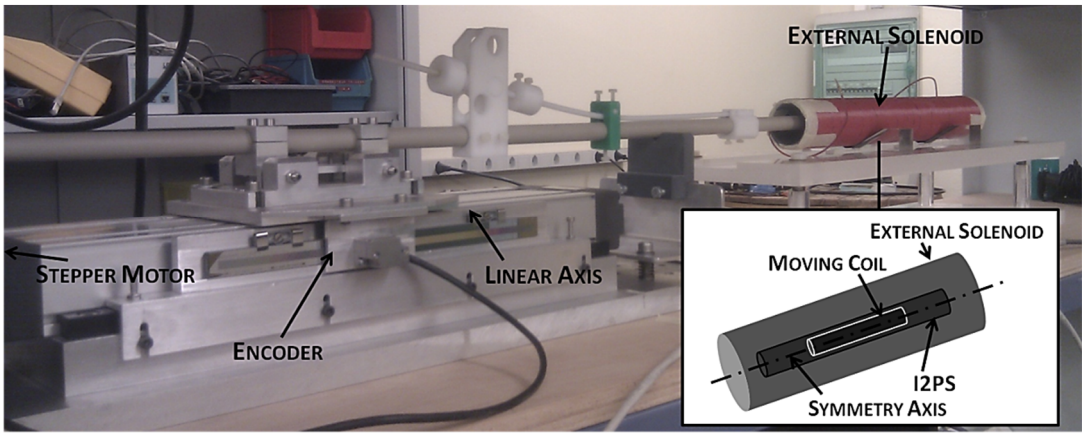

Figure 4.4. The automated test bench used to test the Ironless Inductive Position Sensor prototype.

prototype has been tested without an external case and therefore no resin has been used to seal it.

The sensor's manufacturing gave another constraint to take into account during the design. Since the supply coils are wound over the sense coils, the regularity of the winding (which depends on the winding step variation, the roughness of the surface which the wire is wound on and the number of layers to produce) is a critical factor. As a matter of fact, if the sense coils present several layers, the winding regularity for the supply coils is not *a priori* guaranteed. As a consequence, the number of layers of the fixed windings (i.e. supply and sense) should be small (the numerical value will depend on the manufacturing process, but in general after 10 layers the regularity is difficult to achieve).

The sensor has been tested using an automated test bench, whose details and performances are addressed in detail in [58]. This test bench has been already used to characterize the magnetic interference on Linear Variable Differential Transformers (as explained in Chapter 2). Nevertheless, its data acquisition part has been revised and some mechanical parts replaced in order to host the I2PS prototype. The test bench is shown in Figure 4.4. The moving coil is fixed on a plastic movable support. Acting on a stepper motor, connected with a linear axis, the moving coil can be placed at different positions inside the sensor. The sensor itself is located in an external solenoid (aligned with the linear axis), used to generate an interfering magnetic field, in case it is needed. A linear encoder measures the reference position.

4.2. Validation of the Electromagnetic Models

In this section, the FEM model of the sensor and experimental measurements are used to validate the low-frequency and high-frequency models (regarding the skin and proximity effects), which have been presented in Chapter 3. The dimensions and parameters of the structure are not yet optimized, given that the objective is the confirmation of theoretical models, rather than the design.

4.2.1. Low-Frequency Model Validation

To test the soundness of the low-frequency electromagnetic model, the theoretical calculations have been performed for illustrative values of dimensions and winding parameters on a position range going from -30 mm to 30 mm. For both model and simulations, the excitation is purely sinusoidal at 1 kHz and the fundamental harmonics of the signals have been computed in the

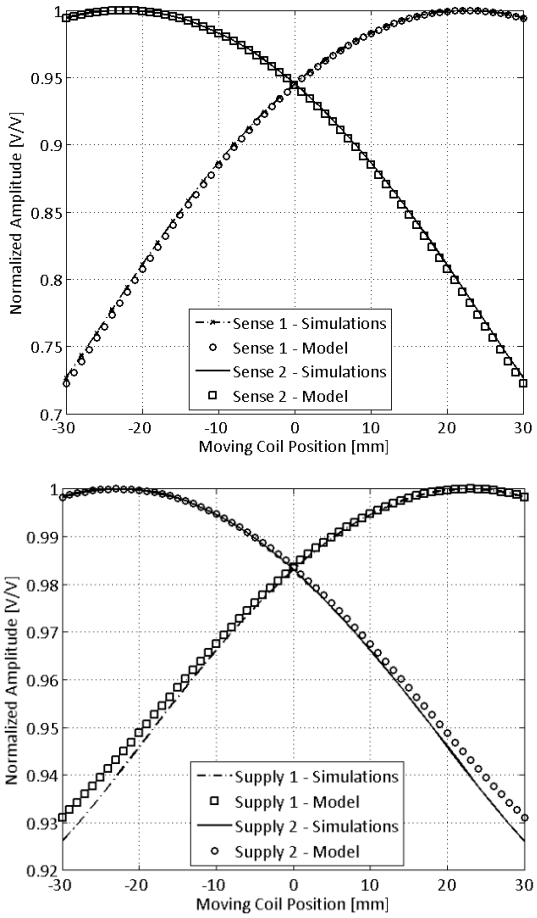

Figure 4.5. (Top) Comparison between normalized amplitudes of sense voltages in case of current supply. (Bottom) Comparison between normalized amplitudes of supply voltages for current supply.

analysis. The computational time for the simulations has been around 8 hours on a Windows-based 64-bit 3 GHz quad-core system with 4 GB RAM. On the other hand, the calculation of the mutual inductances for the model's equations along the entire position range took around 5 minutes without approximations, 30 seconds adopting a scaling factor of 0.1. The number of evaluations of elliptic integrals has been of the order of 10^9 for each position value in the non-approximated computation.

The results are depicted in Figure 4.5 for current supply and in Figure 4.6 for voltage supply. The magnitudes have been normalized to their maximum value to better highlight the signal dynamics on the position range and to have a direct percentage comparison with respect to the model. However, the percentage agreement regarding the actual values will also be cited. By doing so, two types of agreement are pointed out: the agreement on the magnitudes (obtained by comparing the values) and on the trends (obtained comparing the normalized magnitudes). A comparison including the numerical values will be finally proposed in the experimental tests on the optimized prototype, since in that case the measurements are done on an actual sensor (i.e. with fixed parameters).

Figure 4.5 shows the simulation results regarding the sense and supply voltages and their comparison with the model in case of current supply. As predicted by the model, the supply voltages with current supply are also a function of the position. Both graphs describe a non-linear and

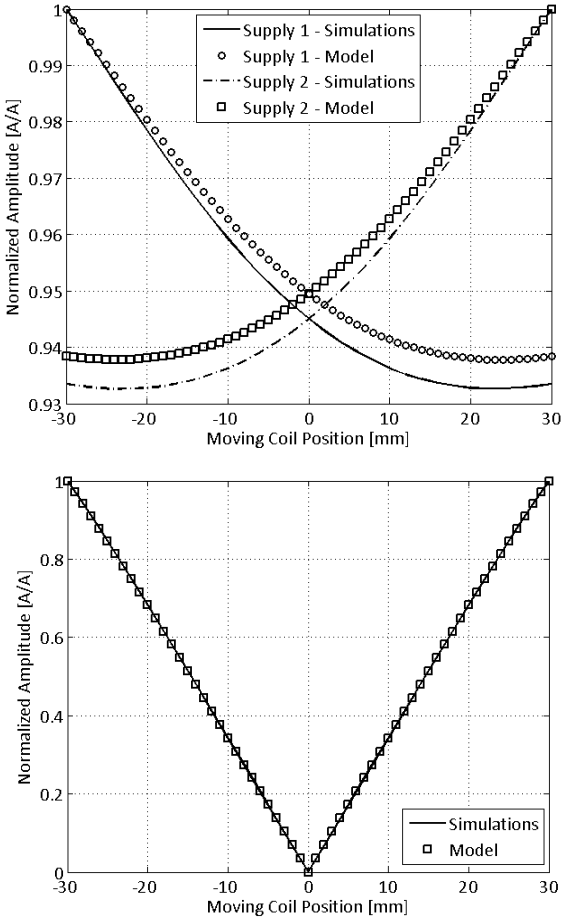

Figure 4.6. (Top) Comparison between normalized amplitudes of the supply currents for voltage supply (Bottom) Comparison between normalized amplitudes of the moving coil induced current for voltage supply.

symmetric dependence of the first harmonics with respect to the moving coil position. In particular, the graphs show very good agreement on the voltage values (more than 97 %) and on the voltage dynamics (always above 95 %). The voltage swing (i.e. the difference between the sense voltage values at the limits of the position range) can be designed to be of some volts. In these simulations, a value of 1.1 V has been observed. It is important to notice that the dynamics of the signals is much more relevant on the sense voltages (27.5% amplitude change in the considered position range) rather than on the supply voltages (7 % amplitude change in the position range).

The graphs of Figure 4.6 illustrate the simulation results regarding the currents in the supply windings and in the moving coil with voltage supply. It is preferable to look at these quantities with voltage supply, rather than at the voltages, since with voltage supply the position dependence is present also in the supply currents. In addition, these currents, together with the induced current in the moving coil, build the sense voltages, as evident from the model's equations (Chapter 3). Therefore, the agreement between model and simulations regarding the sense voltages strongly depends on the corresponding agreement on these magnitudes.

The supply currents behave in a non-linear way and the match between simulations and model is very good in this case too (more than 98 % for the values, more than 93 % for the dynamics). Once again, the symmetry of the device is evident in the curves. The induced current in the moving coil is

a linear function of the position though. In particular, as the model predicted and the working principle of the sensor required, the current is null when the moving coil is in the center of the structure. The agreement with the model is excellent in this case (more than 98 %).

Both supply cases exhibit a non-linear behaviour of the electrical magnitudes with the moving coil position. This non-linearity can be studied and justified by looking at the model's equations (3.16) and (3.21). If the single mutual inductances of the windings are evaluated in the position range, through (3.3), their dependence with the position will reveal to be linear, as moreover explained and demonstrated in Chapter 3. Nevertheless, in (3.16) and (3.21) the expressions involve products between mutual inductances. Therefore, the overall relationship between voltages (in current supply) or currents (in voltage supply) and the position on turn involve such products of linear functions, leading to a parabola-like behaviour.

The comparison between model and simulations with voltage supply has been also performed on the sense voltages, reporting the same agreement.

For what has been observed, the validation of the proposed analytical model showed an agreement between model and simulations always around 96 % both for values and dynamics. The least agreeing cases are reported for magnitudes which exhibit the smallest dynamics, as the supply voltages for current supply and the supply currents for voltage supply. In addition, the hypothesis of neglecting the effects of parasitic capacitances is also justified, since as mentioned the FEM simulator takes them into account.

4.2.2. High-Frequency Model Validation

The high-frequency electromagnetic model has been introduced in order to describe the skin and proximity effects on the Ironless Position Sensor's nominal functioning. In particular, in Chapter 3 it has been pointed out that these high-frequency effects play an important role in defining the electrical resistance of a coil.

In terms of sensor's modelling, these phenomena can also be of primary importance and have significant effect on the definition of the sensor's currents and voltages. Figure 4.7 displays the percentage variation of the moving coil current and that of the sense voltages for illustrative values of winding parameters. This figure shows that the value of moving coil current and sense voltage can be significantly different when the high-frequency effects are considered, generating a big percentage deviation with respect to the "low-frequency" computation. In particular, as the frequency rises up to 10 kHz, differences of about 14 % regarding the moving coil current and more than 10 % regarding the sense voltages are observed for this case. These variations obviously depend on the dimensional parameters and on the sensor's design, but they demonstrate the usefulness of the high-frequency model described in Chapter 3.

The Finite-Element structure used to validate the low-frequency electromagnetic model cannot take into account the high-frequency phenomena regarding skin and proximity effects. As a matter of fact, the simulated geometry of the coils should include every single conductor in order to calculate such contributions. This task is not feasable, since it would create serious problems in the meshing (or even making it impossible, given the enormous amount of tight spaces between the

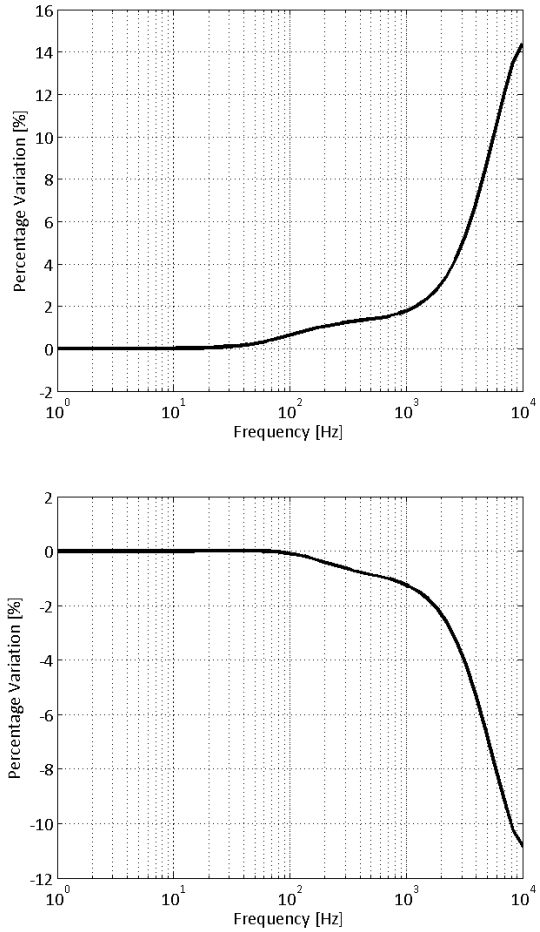

Figure 4.7. Percentage variation of (Top) the moving coil current and (Bottom) the sense voltages when the skin and proximity effects are taken into account (illustrative values of winding parameters are considered). The computation has been carried out with current supply at 30 mm.

conductors that would be present), involve a great number of elements in the electrical circuit and dramatically increase the computational time (or, at worst, prevent the solving process from converging).

Therefore, the validation of the high-frequency model (in particular, the dependency of the electrical resistance on the frequency) has to be performed through experimental measurements. In particular, an impedance analyser has been used to measure impedance's real and imaginary parts. The measurements have been performed on three different coils, which have been manufactured explicitly for this purpose. In fact, it is not possible to perform the measurements on the coils of an

Parameter	Coil A	Coil B	Coil C
Internal Coil Diameter	4 mm	4 mm	4 mm
Wire Diameter	0.335 mm	0.335 mm	0.335 mm
Number of Turns/Layer	250	250	250
Number of Layers	6	14	20
Total Number of Turns	1500	3500	5000
Resistance at 27 °C	5.7 Ω	18.3 Ω	31.0 Ω

Table 4.1. Winding parameters of three different coils for the high-frequency model validation.

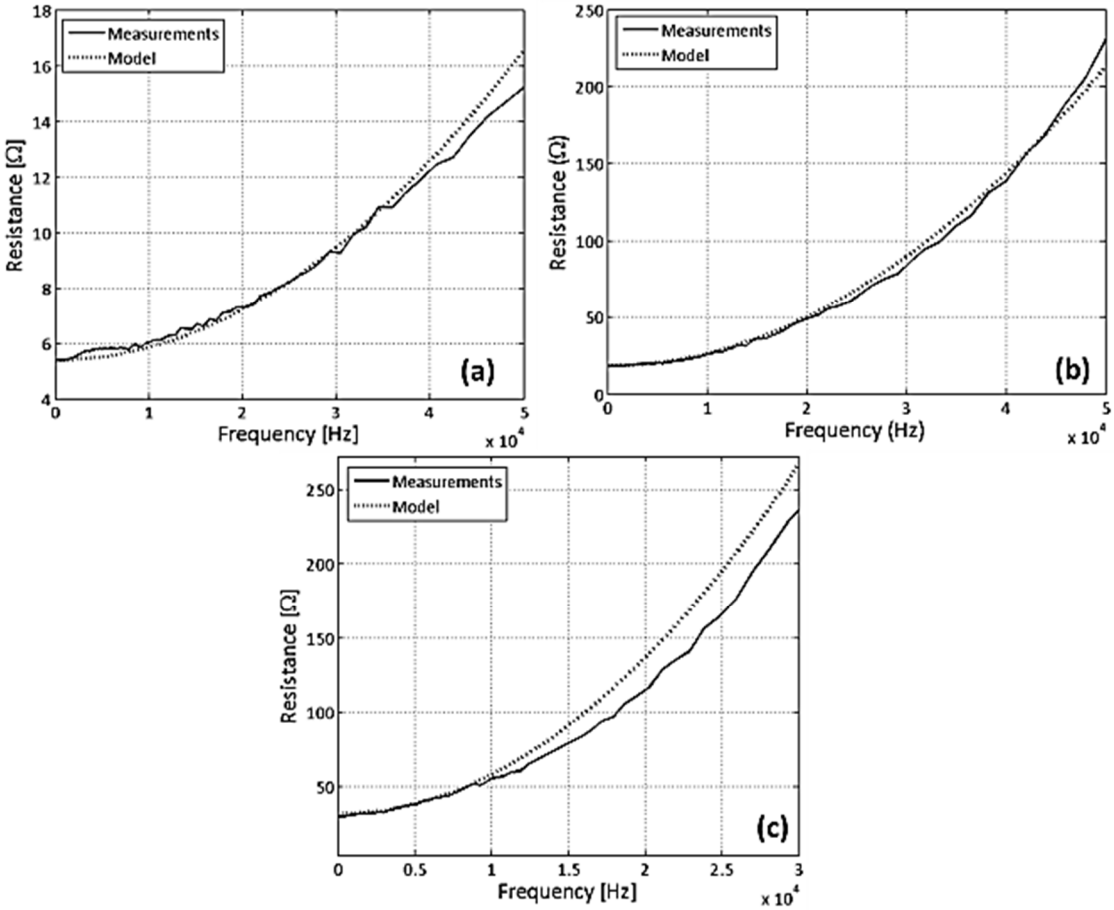

Figure 4.8. Comparison between model's results and experimental measurements regarding the electrical resistance as a function of frequency for (a) Coil A, (b) Coil B and (c) Coil C.

assembled Ironless Inductive Position Sensor, since in this case the real and imaginary parts of the coils' impedance do not correspond to the resistance and the reactance of the winding, as evident from the model's equations, in particular from (3.16) and (3.17).

Table 4.1 shows the parameters of the three coils used for the validation. The three coils present dimensions and parameters so as to be potential candidate of moving coil for an I2PS. The wire diameter which has been used guarantees a nearly uniform distribution of the turns along the coil, allowing the winding of many layers. However, an inevitable degradation of the uniformity is expectable when a very high number of layers (e.g. more than 15) is wound. In fact, the choice of a bigger diameter would lead to evident imperfections in the winding profile, whereas a much smaller diameter would relegate the skin and proximity effects to very high frequencies (i.e. more than 100 kHz), preventing the impedance analyser from detecting them at lower frequencies with respect to parasitic capacitance effects. Very different values have been chosen for the number of layers (the key-factor for proximity effect): therefore, three very different configurations of magnetic fields inside the layers will be described by the model's equations. This will be useful to validate the model in different conditions.

The impedance analyser which has been used is a Cypher Instruments C-60, capable to perform impedance measurements (amplitude and phase) from 10 Hz to 40 MHz with 0.5 % to 4.5 %

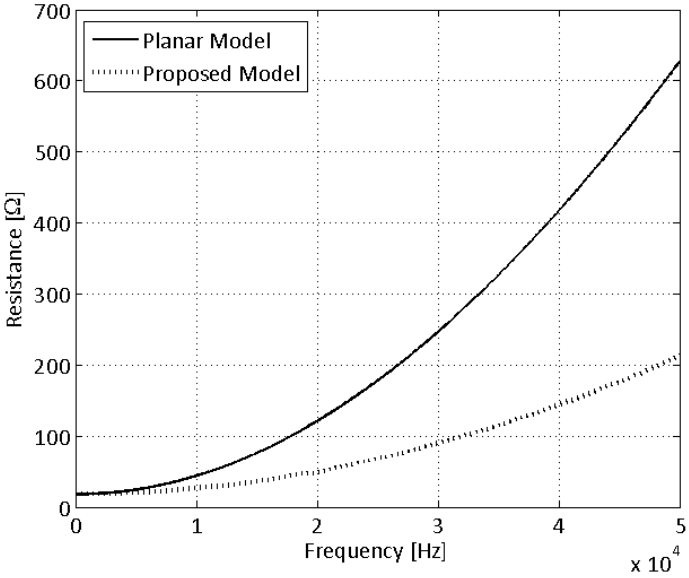

Figure 4.9. Comparison between proposed model and planar model (i.e. not taking into account the curvature radius of the conductors) regarding the electrical resistance of Coil B.

amplitude accuracy and 80 dB dynamic range [110]. The real part of the impedance (i.e. the electrical resistance, since the coil is not coupled with any other element) has been computed and compared to the value obtained with the model in the frequency range from DC to 50 kHz for Coil A and Coil B and from DC to 30 kHz for Coil C[11].

The results are depicted in Figure 4.8. The electrical resistance is growing with the frequency, as expected. In addition, the model closely matches the values coming from the impedance analyser: the agreement regarding Coil A and Coil B is above 93 % everywhere, whereas for Coil C the agreement is above 89 %. In the case of Coil C, the agreement is lower because of the very high number of layers. As a matter of fact, the model described in Chapter 3 assumes that all winding layers are arranged so as to present a uniform conductors' density. In reality, as mentioned, the higher the number of layers, the more difficult is to guarantee a uniform distribution of the layers along the length. Therefore, the proximity effect is less pronounced for Coil C and the measurements exhibit a lower resistance with respect to the value calculated by the model. On the contrary, as Coil A and Coil B are more uniformly wound, the agreement is very good.

In Chapter 3, the high-frequency electromagnetic analysis has taken into account a cylindrical coordinate system, since it has been stated that the conductors are wound circularly and their curvature radius cannot be neglected as it is done in [74, 75]. This assumption can also be verified, by calculating the value of resistance at different frequencies using the model described in [74], which does not take into account the conductors' curvature radius, and comparing it to the value obtained with the model in Chapter 3[12].

The results are in Figure 4.9. The two models return very different results, suggesting that the

[11] After 30 kHz, the evaluation of the electrical resistance for Coil C returned NaN because of the very small difference between the Bessel's functions compared to their absolute value. The numerical problem has been already addressed in Chapter 3.

[12] The model used for the comparison also considers among its hypotheses that the coil presents a ferromagnetic core. Nevertheless, as mentioned in Chapter 3, this assumption affects the magnetic and electric fields distribution, but not the expression of the electrical resistance. Therefore, the comparison is fair.

assumption to neglect the curvature radius of the conductors cannot be made for windings like the ones adopted in an Ironless Inductive Position Sensor, where the internal coil diameter can be of the order of some millimeters (Table 4.1). Therefore, the formulation of the proposed model is even more justified.

The validated high-frequency model can be used in order to perform some preliminary investigations on the winding parameters which are chosen in the design process, in order to establish whether strong influences of skin and proximity effects will be present on the sensor to be designed. Nevertheless, given the nature of generality of the model formulation, it can also be used as a tool of study and analysis of the generic behaviour of electric and magnetic fields in a coil at high frequencies.

4.3. Validation of the Reading Techniques

In this section, experimental measurements on a Ironless Inductive Position Sensor prototype are presented in order to validate the reading algorithms regarding the precision and the temperature compensation. In addition, a remark on the real-time implementation (in order to be actually used for I2PS position reading) is also proposed. Since the aim of the measurements is to validate the reading algorithms and assess their effectiveness, the prototype is not optimized in terms of dimensions and winding parameters.

4.3.1. Validation of the Noise Suppression Algorithm

The noise-suppression algorithm with the designed window function proposed in Chapter 3 has been applied to simulated and measured signals in order to assess its performances and compare them to standard three-parameter Sine Fit (3PSF) algorithm ones.

First, the algorithm has been verified on a simulated test signal. In particular, the main signal amplitude and frequency are 8 V and 1000 Hz. The disturbance signal amplitude is 0.1 V, with a random initial phase in the acquired time window. Actually, the choice of the main signal's amplitude has been made taking illustrative values of winding parameters and calculating the coils' voltages with the electromagnetic model, whereas the frequency has been chosen in order for the amplitude not to exceed 10 V. The signal-to-white-noise ratio is 56 dB, taken as typical value in critical installations, such as the LHC Collimators control system [15].

The results with a simulated signal are shown in Figure 4.10 for a disturbance frequency of 45 Hz. It is evident that with the proposed algorithm, the precision of the amplitude estimation remains within its nominal value (i.e. values without disturbance), without being affected in any way by the sinusoidal disturbance. On the contrary, the standard three-parameter Sine Fit (3PSF) algorithm experiences a strong error on the amplitude estimation. The same results have been observed with several different values of the frequency of the disturbing sinusoidal signal, therefore confirming the effectiveness of the algorithm on simulated signals.

The validation via measurements exploits the signals coming from an actual Ironless Inductive Position Sensor prototype, which has been tested for this validation purpose. The prototype has been tested on the test bench described in section 4.1, its coils' signals have been acquired through

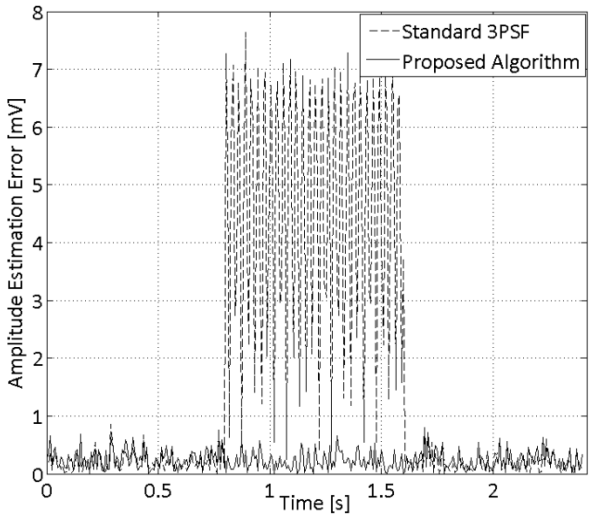

Figure 4.10. Comparison in simulation between the standard 3PSF and the proposed algorithm with a 45 Hz sinusoidal additional disturbance between 0.8 s and 1.6 s. A white Gaussian noise (signal-to-noise-ratio of 56 dB) has been added to the signal as well.

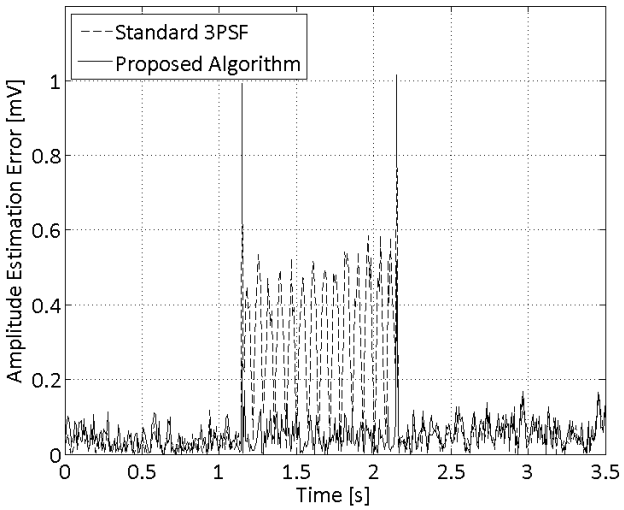

Figure 4.11. Comparison with measurements data between the standard 3PSF and the proposed algorithm with a 7 Hz sinusoidal additional disturbance between 1.1 s and 2.1 s having an amplitude of 70 mV. The measured Signal-to-White-Noise ratio is 56 dB.

data acquisition cards and processed.

The results with the measured signals are shown in Figure 4.11. In this experiment, the disturbance signal has been generated with an external solenoid fed by a sinusoidal current at 7 Hz. The resulting maximum magnetic flux density in air is 1 mT, a typical value which has been measured in critical magnetic environments [15, 111]. The 7-Hz sinusoidal field is coupled with the sense windings and gives rise to a 70 mV-peak sinusoidal voltage at the same frequency, which adds up to the nominal sense voltage due to the sensor's functioning. The measured signal-to-white-noise ratio is 56 dB.

Once again, the proposed algorithm performs better than the standard 3PSF in presence of the disturbance and the amplitude estimation precision remains within the nominal values. The same

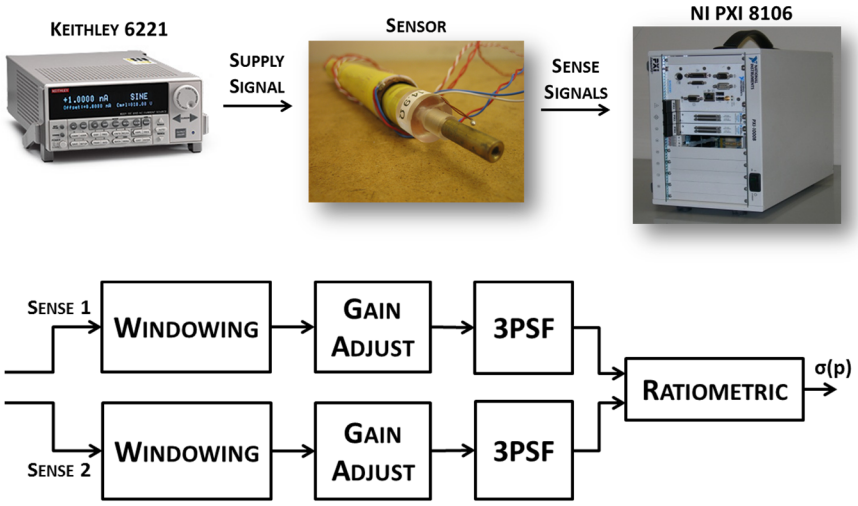

Figure 4.12. (Top) Real-time implementation block scheme. (Bottom) Real-time processing flow-chart to obtain the sensor's position estimation accuracy with ratiometric reading.

results have been observed for different external magnetic field amplitudes and frequencies.

For what has been observed on measured and simulated signals, the proposed noise-suppression algorithm guarantees high-precision and significantly reduces the effects of additional sinusoidal disturbances on the amplitude estimation of the main signal.

4.3.2. Real-Time Implementation of the Noise Suppression Algorithm

As mentioned in Chapter 3, the proposed noise-suppression algorithm includes an important step, which is the signal's windowing before the three-parameter Sine Fit. Given that in critical installation a precise survey time has to be kept (e.g. in the LHC collimators application, the survey time is imposed to be 10 ms), the I2PS position reading with this algorithm should be performed in real-time without constituting a significant burden for the timing of the readout system. This means that the performances of noise suppression and high precision of the algorithm have to be attained without significantly extending the computational time of standard 3PSF algorithm.

For this reason, the proposed algorithm has been also implemented and validated on a PXI controller platform[13] from National Instrument (NI PXI-8106) equipped with analog inputs acquisition cards with sampling frequency of 250 kS/s (NI PXI-6143). The aim of this additional test is to characterize the proposed algorithm in terms of computational time and obtain a comparison of the position reading precision between the proposed algorithm and the standard 3PSF. The physical arrangement and the flow-chart of the algorithm implementation are shown in Figure 4.12.

Table 4.2 summarizes the computational time results for the 3PSF and for the proposed windowing function. The standard deviation has been calculated on 1000 runs. The combination of

Algorithm Step	Average Computational Time [µs]	Standard Deviation [µs]
Three-parameter Sine Fit	206	11
Windowing	19	1

Table 4.2. Computational time performances of the two algorithm steps.

[13] PCI eXtensions for Instrumentation (PXI) is a modular instrumentation real-time platform introduced by National Instruments in 1997. It is designed for PC-based measurement, control and automation applications that require high-performance and modularity [112].

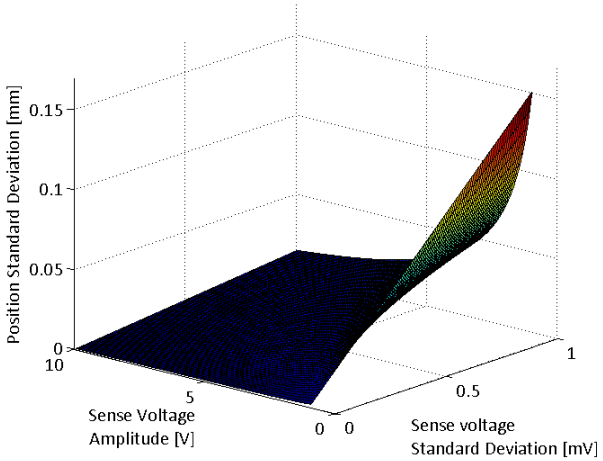

Figure 4.13. Position reading standard deviation of the I2PS with respect to the sense voltages amplitude and to the sense voltages standard deviation.

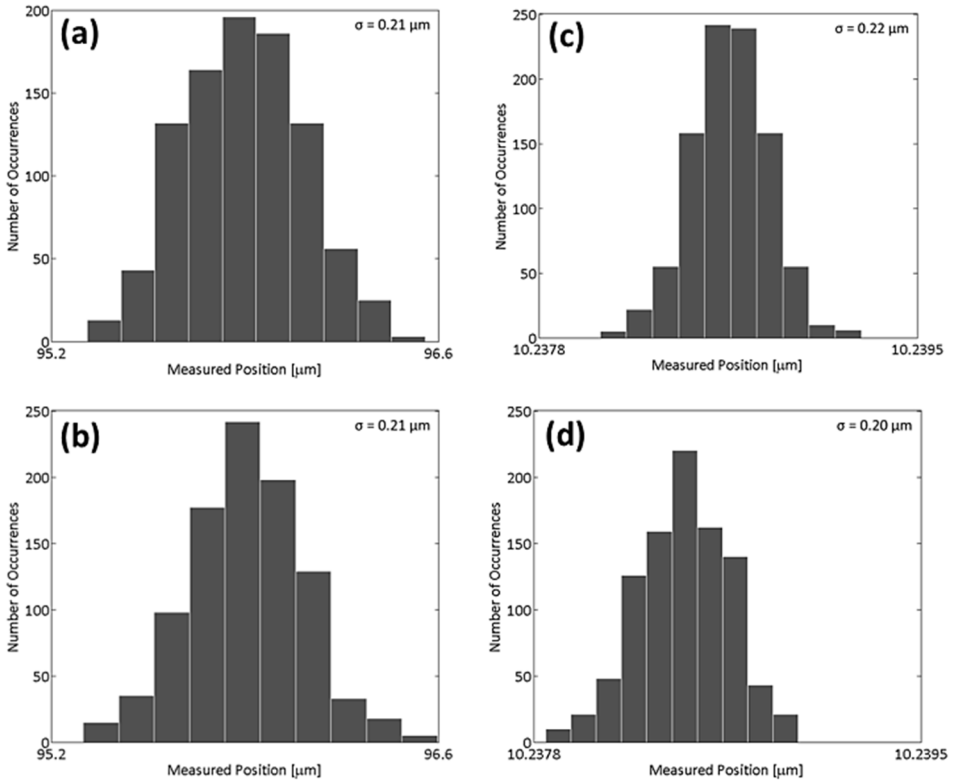

Figure 4.14. Position reading performances with the real-time measurements setup. (Top) Histograms of the I2PS position reading with standard 3PSF algorithm on 1000 readings with 56 dB signal-to-white-noise ratio (a) next to the null point and (c) around 10.24 mm. (Bottom) Histograms of the I2PS position reading with proposed algorithm in the same noise conditions (b) next to the null point and (d) around 10.24 mm.

the 2 algorithms would lead to a processing time of less than 0.3 ms, which is a suitable value for fast position readings conditioning. As an example, taking into account a signal acquisition time of 8 ms (2000 samples acquired at 250 kS/s), a survey frequency constraint of at least 100 Hz would be guaranteed. Overall, the additional windowing step does not constitute a critical load for the real-time application.

A ratiometric computation with the 2 sense coils has been performed to extrapolate the measured position from the voltage signals. Figure 4.13 shows the relation between the standard deviation of the measured position, the standard deviation of the voltages and their amplitude for

the I2PS. Such values have been computed taking into account the definition of ratiometric reading technique and applying the uncertainty propagation law. From this graph it is evident that voltages amplitudes of about 7-8 V and voltages standard deviation below 0.1 mV have to be attained to obtain position uncertainty below 1 micrometer.

For this reason, in the real-time test the sensor has been fed with a current signal so as to have an amplitude of 8 V for the sense windings voltages at a certain position. Figure 4.14 shows the position reading performances achieved with the real-time setup as histograms computed over 1000 repeated acquisitions in two different moving coil positions (i.e. around the null-point and about 10 mm). The standard deviation of the position readings is around 0.21 µm and is not worsened by the windowing in the two cases. As a matter of fact, the standard deviations of the sense windings' voltages showed practically the same values for the two algorithms (i.e. order of 10 µV). Similar results have been observed repeating the measurements with different values of the moving coil position.

Therefore, from what has been observed, it can be stated that on a real-time implementation the proposed algorithm shows very good precision on the estimated position and does not exhibit criticality concerning the computational time.

4.3.3. Validation of the Temperature Compensation Algorithm

In Chapter 3, the sensitivity of the Ironless Inductive Position Sensor reading with respect to ambient temperature has been investigated and an algorithm to compensate its effect on the ratiometric reading has also been proposed.

The algorithm has been applied on a I2PS sensor prototype. The prototype has been installed in a climatic chamber with temperature control, so as to simulate the variation of ambient temperature. The supply signal is a 25 mA-peak current sine-wave at 1 kHz, whereas the DC signal used to measure the average temperature is of 10 mA. Given that the series resistance of the two supply coils is about 100 Ω for this prototype, the value of DC voltage is expected to be around 1 V. The value of supply current does not influence the reading algorithm, since the ratiometric is independent from primary signal's variation [38]. The measurements have been carried out at different positions of the moving coil, in order to widely test the algorithm.

The compensation equation is (3.75)

$$r_0 = \frac{r(T)}{(1 + \zeta \cdot \Delta V_{DC}(T))} \tag{4.1}$$

where $r(T)$ is the acquired ratiometric, ΔV_{DC} is the variation of DC primary voltage due to the ambient temperature, $\zeta = \alpha_r / g_{DC}$ $[V^{-1}]$ is the correction factor. α_r and g_{DC} are the normalized variation of the ratiometric per unit degree and the constant of proportionality between the primary DC voltage and the ambient temperature (see Chapter 3).

First of all, the value of ζ has to be calculated. The value of g_{DC} has been found equal to $4.05 \cdot 10^{-3}$ V/°C. The value of α_r is slightly different for each position, but the temperature compensation has been performed adopting a weighted average of the values (the weight takes into account that in the extreme positions the position drift due to temperature variation is much more significant than

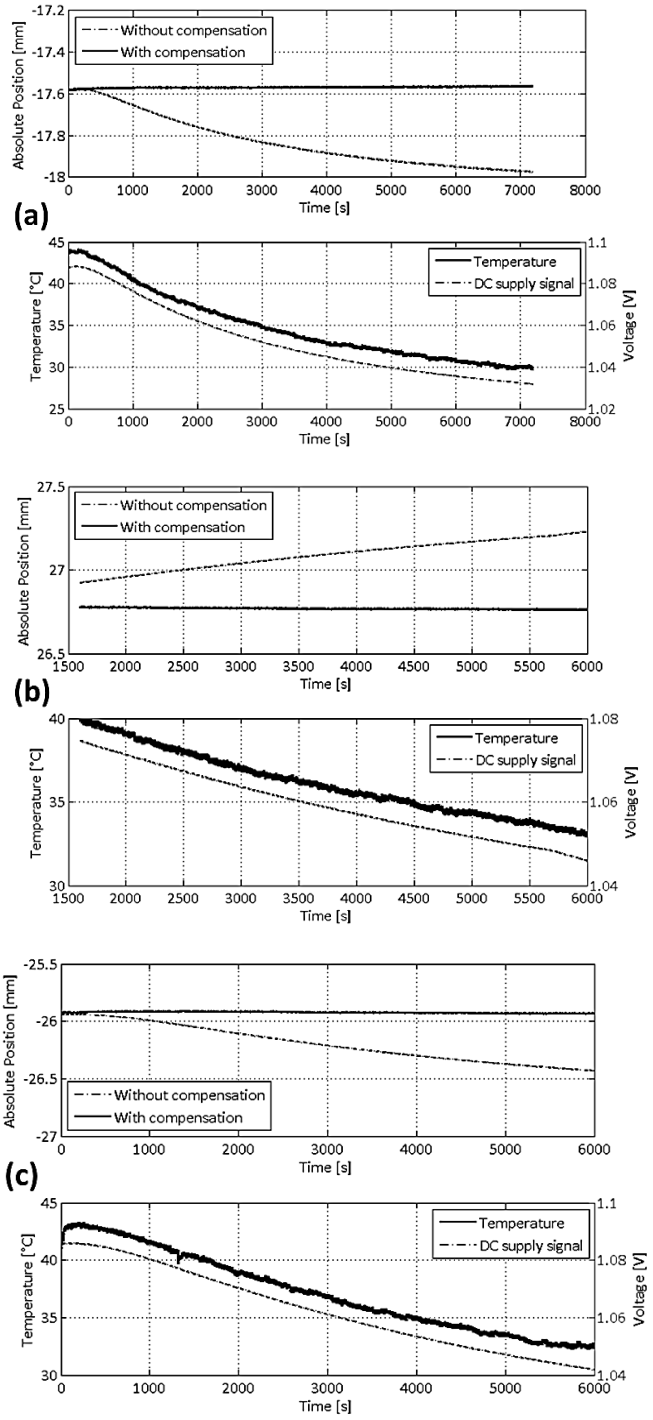

Figure 4.15. Experimental Measurements showing the effectiveness of the temperature compensation on the Ironless Position Sensor reading. (a) Position of about -17.6 mm; (b) Position of about 26.8 mm; (c) Position of about -25.8 mm. The temperature and the DC signal are also shown.

in the internal positions, as clearly observed in Chapter 3). The value of ζ which has been calculated in the measurements is -0.42 V^{-1}, whereas the reference DC voltage value has been taken at 44 °C and is 1.088 V. In principle, the reference temperature can be fixed *a priori* and it establishes the temperature at which the sensor's calibration has to be performed.

Figure 4.15 shows the results of the experimental measurements which have been carried out on the I2PS prototype at different positions. The sensor has been tested with slow temperature drops of 14 degrees maximum over almost 2 hours. The temperature and the DC supply voltage have also

been acquired and displayed, in order to give a complete overview of the experiments.

Figure 4.15(a) shows that without compensation the sensor's reading exhibits a thermal position drift at -17.6 mm of about 400 µm over a temperature drop of 14 degrees. Instead, the thermal position drift reduces significantly when the compensation is applied. In particular, the position sensitivity to ambient temperature at about -17.6 mm is 29 µm/°C without compensation, whereas it reduces to 1.4 µm/°C with the compensation algorithm, denoting an improvement of a factor 21. Figure 4.15(b) shows that the sensitivity to ambient temperature at about 26.8 mm is 50 µm/°C without compensation, whereas with the compensation algorithm it drops to 2.2 µm/°C, denoting an improvement of a factor 23. The reason why the two position readings (i.e. with and without the compensation) do not start at the same position value is that the starting temperature (i.e. about 40 °C) does not coincide with the reference temperature (i.e. 44 °C), and therefore the graph trace starts already with a compensated value. Figure 4.15(c) shows that the sensitivity to ambient temperature at around -25.8 mm is 46 µm/°C without compensation, whereas it reduces to 1.8 µm/°C with the compensation algorithm, denoting an improvement of a factor 26. Similar results have been observed for other moving coil position values. In particular, around the zero the position sensitivity to ambient temperature exhibits its smallest value without compensation (about 2 µm/°C). Nevertheless, in this case, the sources of this very weak temperature sensitivity are not located in the moving coil resistance (for which the sensitivity should be null). They can be instead ascribed to the tiny current flowing in the sense windings, introducing a weak dependence on the sense winding resistances. However, the sensitivity reduces to 1.5 µm/°C with the compensation.

The results shown in Figure 4.15 also confirm that thermal expansion does not play a role and can therefore be neglected. It is also worth noticing that the factor α_r has been measured and at -17.6 mm its value is $-1.65 \cdot 10^{-3}$ °C^{-1}, which is very similar to the values of α_r obtained with the model and already illustrated in Figure 3.19.

Finally, it has been observed that the position uncertainty is not significantly affected by the compensation algorithm, as moreover predicted by the uncertainty analysis which has been carried out in Chapter 3. In fact, the standard deviation on the position reading without compensation is about 0.5 µm, whereas it is 0.6 µm with the compensation.

For what has been observed, the compensation algorithm shows full effectiveness at different moving coil positions. Therefore, the theoretical treatment on which it is based is also confirmed, as well as the non-criticality of the approximation on the variability of the factor α_r.

Regarding the real-time implementation of this temperature compensation, it involves just the operation described in (3.75), which is a division between single readouts (i.e. single numbers, not arrays), where the factor ζ is pre-calculated. Therefore, the compensation does not produce a significant increase of the computational time.

4.4. Sensor's Optimization and Test

Once the theoretical models have been fully demonstrated and the reading techniques validated, the design optimization of an Ironless Inductive Position Sensor can be performed taking a case study as target application. In this case, the LHC Collimators application will be adopted. The

optimization process here described is based on the design optimization guidelines given in Chapter 3. The final sensor is also tested and the magnetic immunity, the main property of this device, is demonstrated with experimental measurements.

4.4.1. Requirements and constraints

The LHC Collimation system has been described in detail in Chapter 1. To measure the jaws' position, Linear Variable Differential Transformers are used. To replace such sensors with Ironless Inductive Position Sensors, a similar space occupancy has to be guaranteed. In this way the new sensor's installation would not lead to profound alteration of the collimator's mechanical assembly. In addition, the same position range has to be respected. In numbers:

- The maximal sensor's diameter cannot exceed 26 mm. Such constraint will have impact on all coils' diameters.
- The total sensor's length cannot exceed 220 mm. Such constraint will have impact on the coils' lengths and the connectors.
- The moving coil position range has to be [-25 mm, 25 mm]. A slight non-linearity (0.2 % in [-18 mm, 18 mm]) is acceptable. This specification will have impact on the coils' lengths.
- A strict survey time of 10 ms has to be respected in the readout system. This constraint will have impact on the choice of the frequency and the readout parameters (sampling frequency, number of samples etc.).
- The coils' voltages cannot exceed 10 V, in order to respect the data acquisition channels' range and guarantee a good resolution of the conditioning electronics. This constraint will have impact on the choice of the frequency and excitation signal amplitude.

As mentioned in Chapter 3, the current supply case is preferred to the voltage supply when the temperature compensation has to be adopted, therefore the optimization will be carried out in this case. The objective function of the procedure will be the ratiometric swing (i.e. the value of ratiometric at one extreme position).

4.4.2. Optimization Process

Henceforth, the notation regarding diameters and other dimensions adopted in Chapter 3 (Figure 3.27) will be adopted. To keep the current density in the wires at a low level for thermal stability, the wire diameter of the supply coils have to be bigger than the sense coils' one. The latter can be chosen small since no current is flowing into the sense coils. The moving coil's wire diameter has also to be big since this will keep the resistance small, but given the high number of layers which is expectable, the space constraints should be kept. The values chosen are d_{wp} = 0.2 mm for the supply coils, d_{ws} = 0.05 mm for the sense coils, d_{wc} = 0.4 mm for the moving coil.

Given the constraint of maximum length, the upper bound for the supply and sense coils' lengths is about 90 mm. With this value, the winding assembly will have a length of 180 mm. 20 mm on each side have been left for connections and washers. Given the big moving coil wire diameter, the coil support should have a tiny diameter and at the same time the total diameter of the moving coil should reserve enough space for the sense and supply coils. In addition, at least 1 mm of air-gap between the moving coil and the fixed coils' bobbin has to be left, in order to guarantee contactless

sensing. For these reasons, the upper bound for the outer diameters of moving coil and supply coils are fixed to 15 mm and 22 mm respectively. 2 mm of space on each side for the sensor's housing have been left. Given that the performances of the sensor increase with the radial dimensions, the upper bounds are taken as design choices. The inner diameter of the moving coil is chosen to be 4 mm. Smaller values would lead to technical difficulties in the manufacturing of the support bobbin, which anyway would be too thin to withstand the winding process.

With the chosen values, 14 winding layers are expectable for the moving coil. For the fixed coils, the support bobbin has a diameter of 17 mm and a thickness of 1.5 mm. Therefore, the inner diameter of the sense coils is 20 mm. For this reason, 1 mm on each side is available for the winding of sense and supply coils. This space is enough for three 0.05-mm layers (sense) and four 0.2-mm layers (supply), leaving 0.05 mm for the insulator in-between. For what has been also said in Section 4.1, the number of layers is small enough to guarantee a good winding regularity.

The coils' lengths have now to be fixed. To minimize the non-linearity of the device, the optimum choice would be (3.86)

$$a_C \geq 2p_{MAX} \tag{4.2}$$

where a_C is the moving coil semi-length and p_{MAX} is the extreme position. This means that a_C should be at least 50 mm. In addition, in Chapter 3 it has been demonstrated that the solution which gives best ratiometric swing is

$$a_S = a_P = a_C \tag{4.3}$$

Winding	Parameter	Value
Moving Coil	Wire diameter	0.4 mm
	Inner diameter	4 mm
	Outer diameter	15 mm
	Number of layers	14
	Number of turns per layer	225
	Length	90 mm
Sense Coils	Wire diameter	0.05 mm
	Inner diameter	20 mm
	Outer diameter	20.3 mm
	Number of layers	3
	Number of turns per layer	1600
	Length	80 mm
Supply Coils	Wire diameter	0.2 mm
	Inner diameter	20.4 mm
	Outer diameter	22 mm
	Number of layers	4
	Number of turns per layer	400
	Length	80 mm

Table 4.3. Dimensional parameters after optimization of the I2PS coils.

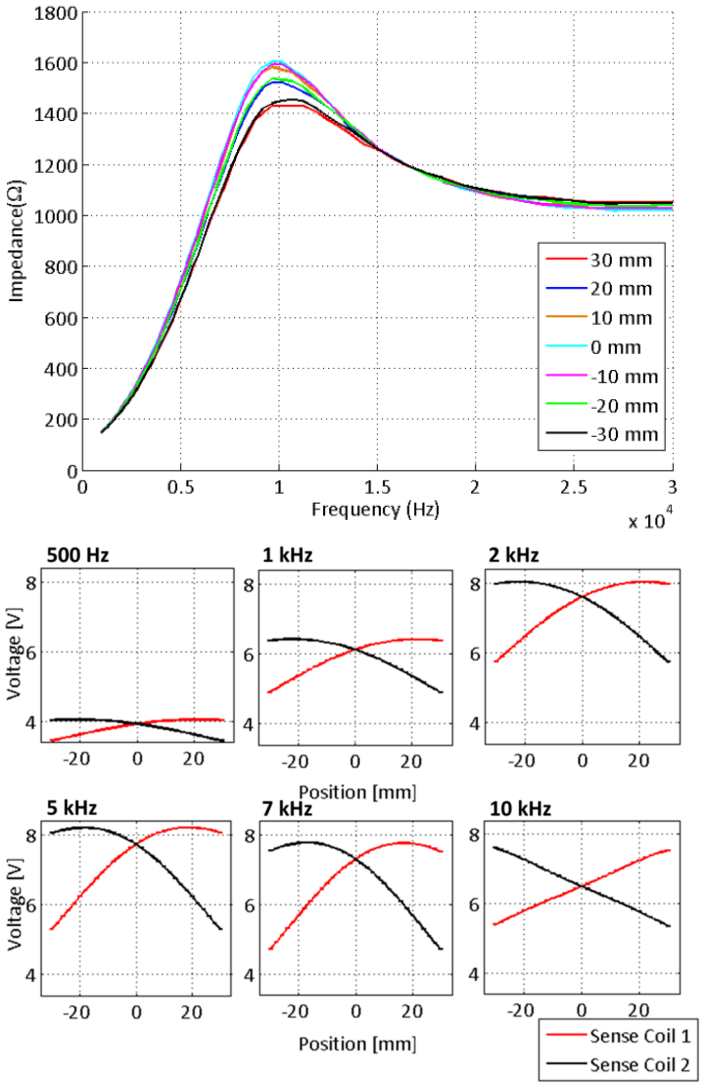

Figure 4.16. (Top) Impedance seen by supply coils' electrodes at different frequencies and several positions. (Bottom) Sense voltage profiles at different frequencies. For each frequency value, the supply current has been chosen in order to have always the same amplitude of voltage on the supply windings.

This means that the fixed coils would have a total length of at least 100 mm. This value would lead to unacceptable longitudinal dimensions of the sensor. Therefore, since a slight non-linearity is anyway acceptable, the value of a_C is chosen to be 45 mm and a_S and a_P will be 40 mm. Thus, the total length of the fixed coils' assembly will be 160 mm, which is below the limit and gives a reasonable margin for uncertainty. At this point, the number of turns per layer can also be determined.

Table 4.3 shows the list of dimensional parameters which have been obtained with the optimization. The parameters left are the operational frequency, the acquisition settings and the excitation current amplitude. These can be found after the manufacturing of the prototype, with additional experimental tests.

The formulas in Chapter 3 demonstrate that with current supply the voltages on the supply windings grow with the frequency, as long as parasitic capacitances do not influence them. The impedance seen by the supply coils' electrodes is then prevalently inductive. Figure 4.16 shows the impedance seen by the supply electrodes as function of the frequency. The measurement has been carried out with the impedance analyser. It is evident that after about 8 kHz, the effects of parasitic

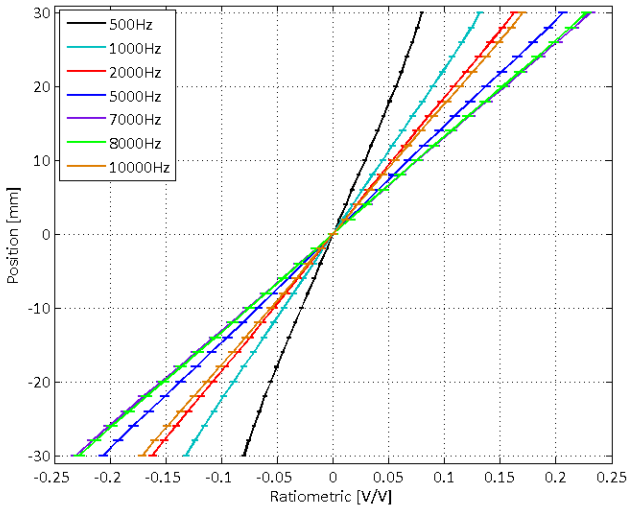

Figure 4.17. Calibration curves at different frequencies. For each frequency value, the supply current has been chosen in order to have always the same amplitude of voltage on the supply windings.

capacitances start playing the major role. The same phenomenon happens for several moving coil position values. From Figure 4.16 it is also evident how the sense voltages are affected. As a matter of fact, below 8 kHz they always present a maximum inside the position range (as the theory predicts). Nevertheless, at 10 kHz the maximum does not appear anymore and the amplitudes start decreasing already after 6-7 kHz. For frequencies above 10 kHz, the measurements showed that the voltages do not exhibit symmetry anymore. Therefore, the operational frequency should be well below 8 kHz.

Other two important points to take into account when choosing the frequency are the sensitivity and the reading uncertainty. Figure 4.17 shows the position-ratiometric curves for different frequencies in the range [-30 mm, 30 mm]. The curves which exhibit the smallest slope indicate a more remarkable sensitivity of the device. It is interesting to notice that the slope decreases when the frequency increases, but after 7-8 kHz the trend changes and the slope starts increasing. Therefore, from this point of view, a high frequency is advisable, however not higher than 7-8 kHz.

When the frequency rises, more and more samples are acquired inside the acquisition time window, therefore reducing the amplitude estimation uncertainty. Therefore, from this point of view, a high frequency is also advisable.

As a result of the extensive experimental tests made on the I2PS prototype, the frequency of 1 kHz has been chosen. It is far enough from 8 kHz, so as to avoid high-frequency effects, guarantee good sensitivity and position uncertainty (8 periods acquired in 8 ms), as the tests will show.

For the acquisition parameters, a sampling frequency of 250 kS/s has been chosen in order to have enough samples in a period. Knowing the relation between number of samples and required precision, 8 periods (2000 samples) of the signals can be acquired, leaving 2 ms for the processing.

Once the operational frequency is chosen, the amplitude of the supply current can be established by imposing a maximum level of 10 V for the voltages and calculating the current density in the supply wire (for thermal stability). A 30 mA-peak sinusoidal signal satisfies all these requirements (the current density is about 0.8 A/mm^2 and the internal heat generation in the wire can be

Parameter	Value
Operational Frequency	1 kHz
Excitation Current Amplitude	30 mA
Sampling Frequency	250 kS/s
Number of Samples	2000

Table 4.4. Electrical and acquisition parameters after optimization of the I2PS coils.

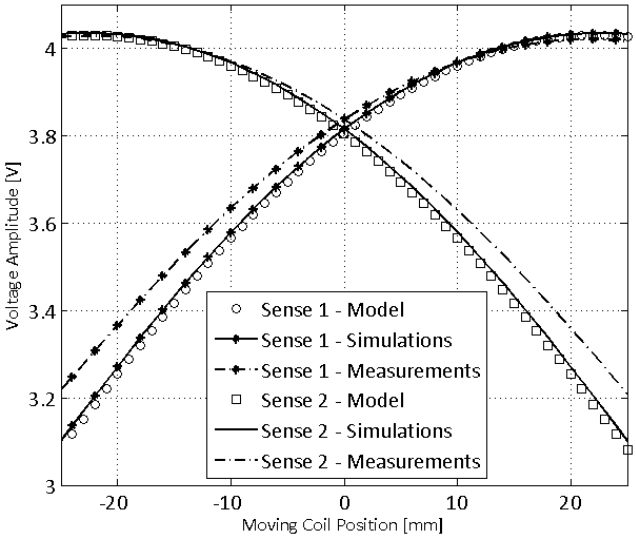

Figure 4.18. Sense voltages at different positions for the optimized prototype, obtained with the electromagnetic model, FEM simulations and with experimental measurements. The uncertainty on the experimental measurements is about 50 µV.

neglected).

Table 4.4 lists the electrical and acquisition parameters which have been chosen in the design. At this stage, the design of an Ironless Inductive Position Sensor for the LHC Collimators application is complete. The choice of the housing material is not crucial from the design viewpoint (as long as it is non-magnetic and exhibits a high resistivity to minimize the eddy currents) and it can be performed *a posteriori*, with experimental tests.

Finally, this process may be followed as a general example also for different kind of application where the ratiometric swing constitutes the objective function to optimize.

4.4.3. Test

The optimized prototype has been tested in order to draw its characteristic curves and verify the magnetic immunity. The sense voltages at different positions are reported in Figure 4.18. In this figure, a comparison with the voltages obtained with the electromagnetic model and with a FEM simulation of the optimized structure is also proposed, as a further experimental confirmation of the theoretical results. The voltage values coming from the model have been computed taking into account the high-frequency effects on the moving coil's electrical resistance and adopting a scaling factor of 0.1. The measurements show very good agreement with the theoretical values (always above 94 %) especially for maximum coupling (where the agreement is 99 %). The 5 % discrepancy which can be observed may be due to the fact that in the experimental tests the moving coil's

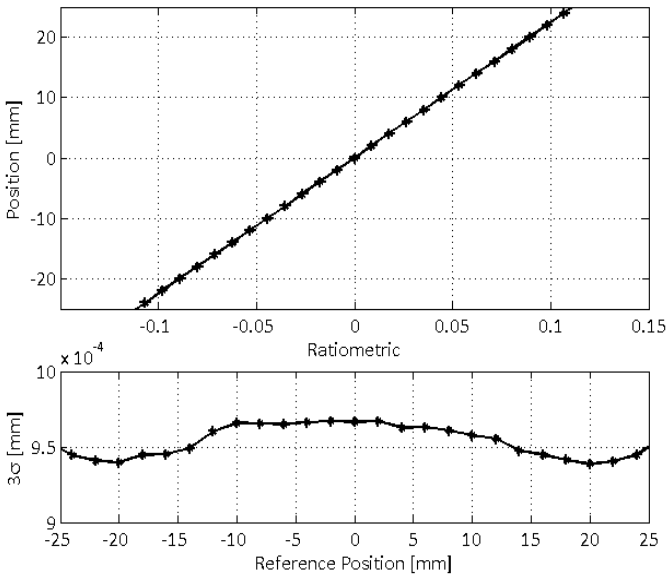

Figure 4.19. (Top) Calibration curve of the optimized sensor. (Bottom) Position reading uncertainty reached with the optimized sensor's configuration, obtained as the standard deviation on 30 repeated measurements with a coverage factor 3.

longitudinal axis cannot be precisely centred with the axis of the sensor. These results give also further confirmation to the hypotheses made as basis of the models.

As far as the measurements results are strictly concerned, good symmetry is observed in Figure 4.18, testifying an accurate sensor's manufacturing. In addition, the maximum of the sense voltages occurs at about 22.5 mm, as the theory predicted. Even being slightly inside the position range, the maximum does not produce enormous non-linearity in the calibration curve of the device. This curve is depicted in Figure 4.19, together with the position reading uncertainty for all the position values in the range. The non-linearity error can be calculated in the position range as

$$NLE = 100 \cdot max\left(\frac{p' - p^*}{MCPR}\right) \tag{4.4}$$

where p^* is the moving coil reference position, p' is the position calculated through linear interpolation of the calibration curve, $MCPR$ is the moving coil position range considered. For the optimized prototype, the NLE is 0.6 % in the full position range and reduces to 0.2 % in [-18 mm, 18 mm]. These values are not far from common non-linearity errors of Linear Variable Differential Transformers. The sensor's gain (i.e. the slope of the linear interpolation of the calibration curve), which also gives an indication on the sensitivity, is 225.4 in the full position range, whereas it is 225.0 in [-18 mm, 18 mm], once again confirming the good linearity. From this value, the sensitivity of the sensor is about $1/225 = 4.4 \cdot 10^{-3}$ mm^{-1}. LVDTs exhibit sensitivities of the same magnitude.

From Figure 4.19 the nominal uncertainty of the position reading can also be discussed. With the optimized parameters (mainly excitation current and operational frequency) a position uncertainty of less than 1.5 µm has been achieved (often even less than 1 µm). This value is well within the specifications given in Chapter 3. However, if the uncertainty has to be even lower, it is sufficient to slightly increase the frequency (adjusting the excitation current so not to have voltage amplitudes of more than 10 V), improving in this way also the sensitivity (as from Figure 4.17). Additional

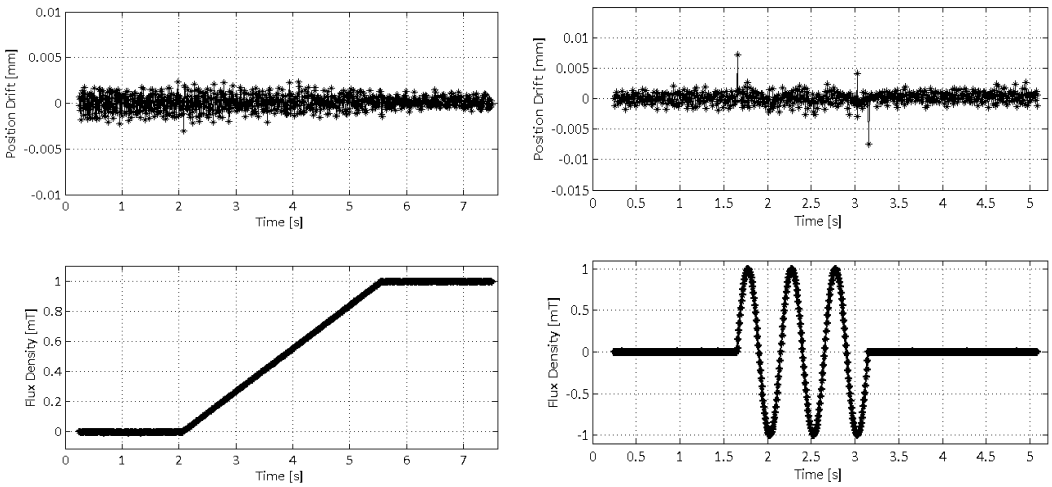

Figure 4.20. (Left) Position drift with an external ramped magnetic flux density of 1 mT at 0.3 mT/s. (Right) Position drift with an external sinusoidal magnetic flux density of 1 mT at 2 Hz.

measurements showed that with 2 kHz and 20 mA of excitation current, the uncertainty is 0.6 µm and the sensitivity is $5.4 \cdot 10^{-3}$ mm^{-1}. This solution can be adopted as a backup choice in the case when an analysis of the environmental noise shows that an operational frequency of 1 kHz is not possible. However, frequencies higher than 2 kHz have to be discarded because approaching the limit of 8 kHz.

The last matter to be discussed is the magnetic field immunity. As a matter of fact, this particular sensor's property has been advanced when describing the working principle and the electromagnetic model in Chapters 2 and 3. Experimental measurements with external longitudinal magnetic fields on the described test bench have been performed on the optimized prototype in order to verify this property. In particular, the tests have been performed with a ramped magnetic field reaching 800 A/m (i.e. approximately 1 mT in air) with different ramp rates and with a sinusoidal profile at different frequencies.

The results are depicted in Figure 4.20 for two cases where the moving coil position is 10 mm. The ramp rate is 0.3 mT/s and the frequency of the sinusoidal field is 2 Hz. It is evident that the position drift (computed as the difference between the position read in presence of the external interference and the position read in absence of the interference, as defined in Chapter 2) stays always around the zero within its uncertainty. This happens with slowly-varying fields (i.e. during the ramp and the sinusoid) and with constant field (i.e. when the ramp reaches the maximum value). It is interesting to observe that at the beginning and at the end of the sinusoidal profile two spikes in the position drift are reported. These are due to the discontinuity of the derivative of the magnetic field profile (which contains all frequencies). The same results have been observed with different ramp rates, frequencies of the interfering sinusoidal signal and moving coil positions. The magnetic immunity is also confirmed with voltage supply, as expected.

For what has been observed, the results coming from the experimental tests carried out on the optimized structure confirmed the values of sensitivity and non-linearity expected. In addition, the sensor satisfies the dimensional and operational constraints given in subsection 4.4.1. Finally, the magnetic field immunity has also been confirmed.

Innovative Contribution of the Chapter and Related Publications

The theoretical basis which has been drawn in Chapter 3 regarding the low- and high-frequency electromagnetic models, the thermal compensation and the noise-suppression reading technique finds full confirmation in this chapter, where a Finite Element model of the sensor and experimental measurements are used to validate the theory. The agreement between models and validation data (obtained either with simulations or experimentally) is always very good (above 93 %), the temperature sensitivity is dramatically reduced and the disturbing effect on the three-parameter Sine Fit algorithm given by an additional sinusoidal signal is eliminated. In addition, the optimization process proposed in Chapter 3 has been here used to design an Ironless Inductive Position Sensor for the LHC Collimators application. On the optimized prototype, experimental tests have been carried out to verify the sensitivity, uncertainty and magnetic immunity.

1. A. Danisi, A. Masi, R. Losito, Y. Perriard: "*Electromagnetic Analysis and Validation of an Ironless Inductive Position Sensor*", accepted for publication in IEEE Transactions on Instrumentation and Measurement, November 2012.

2. A. Danisi, A. Masi, R. Losito, Y. Perriard: "*Modelling and Compensation of Thermal Effects on an Ironless Inductive Position Sensor*", proceedings of ECCE 2012, Rayleigh, North Carolina, September 2012.

3. A. Danisi, A. Masi, R. Losito, Y. Perriard: "*Electromagnetic Modeling of an Ironless Position Sensor*". Proceedings of IEEE I2MTC 2012, Graz, Austria, May 2012.

4. A. Masi, A. Danisi, R. Losito, Y. Perriard: "*Characterization of Magnetic Immunity of an Ironless Inductive Position Sensor*", submitted to IEEE Sensors Journal, February 2012.

5. A. Masi, A. Danisi, R. Losito, Y. Perriard: "*Ironless Position Sensor with Intrinsic Immunity to External Magnetic Field*", proceedings of IEEE Sensors 2011, Limerick, Ireland, October 2011.

Chapter 5

Conclusions and Outlook

Abstract

In this chapter, a conclusive analysis on the innovative contributions which have been proposed in this thesis is advanced. In addition, particular attention is given to the possible future development regarding the Ironless Inductive Position Sensor, but also concerning the exploitation of the developed models and their results in the forthcoming scientific research.

5.1. Achieved results

5.1.1. Analysis

The physical phenomenon of the magnetic interference on Linear Variable Differential Transformers has been observed in the specific application of linear position sensing in the Large Hadron Collider's collimators [111]. Taking this application as a starting point, a more general research work has been pursued regarding the study of possible countermeasures to this effect.

An extensive work has been dedicated to the characterization of the magnetic interference through Finite Element Method. The FEM model of an LVDT led to a design tool which can be used as a general-purpose mean to simulate the effect of magnetic fields on LVDTs. The model has also been used to conceive an effective method to reduce the position drift due to the external magnetic field. The solution presents a combination of proper magnetic shielding and a DC polarization superposed to the AC primary signal. The results showed that the position drift can be significantly diminished. Nevertheless, it is not possible to achieve complete immunity to external magnetic fields, due to the unavoidable presence of ferromagnetic materials in the sensor's assembly.

This result triggered an important breakthrough in the research workflow. In fact, at this point, the Ironless Inductive Position Sensor (I2PS) has been individuated as possible solution to the magnetic interference problems. The structure of the sensor is conceived so as to avoid any ferromagnetic material and at the same time keep the outstanding performances of the LVDT, in terms of uncertainty, robustness, radiation-hardness, lifetime and cost-efficiency. A detailed description on the realization and on the physics of the sensor is proposed, together with an exhaustive comparison with standard LVDTs.

Consequently, a wide and broad-spectrum modelling work has been carried out. A detailed electromagnetic model of the I2PS has been proposed, describing the working principle of the sensor in the phasors' domain and the effect of high-frequency phenomena (skin and proximity effects). The rigorous analyses are always preceded by state-of-the-art investigations on existing models and constitute actual analytical stand-alone modules: they do not need preliminary estimations from FEM simulations or measurements. The model regarding the working principle has been validated with FEM simulations and finally compared with experimental measurements on an optimized prototype for a specific application, showing very good agreement (more than 94 %). The electromagnetic analysis of the high-frequency phenomena has been validated with experimental

measurements carried on with an impedance analyser, showing an agreement of 93 %. A model has also been prepared for thermal effects influencing the sensor's position reading. After verifying that limiting the current density in the wires, the wire over-heating can be avoided even in closely-packed configurations, the results obtained with the electromagnetic model have been extended introducing the dependency on ambient temperature. The results showed that when important variations of the ambient temperature are foreseen, the current supply method is preferred to the voltage supply. Nevertheless, it has been demonstrated that the position reading is always affected by ambient temperature. Therefore, the thermal model has been used to conceive a reading algorithm for compensating the temperature drift. This algorithm is general and application-independent and does not affect the sensor's electromagnetic functioning. The validation of the compensation algorithm (which showed an average improvement factor of 23 on the position drift) on turn confirmed the theory of the thermal model.

The position reading of the I2PS can be performed just as for the LVDTs, adopting Sine-Fit based algorithms and ratiometric reading techniques. Nevertheless, experimental measurements and simulations showed that when the interfering field is sinusoidal, the three-parameter Sine Fit algorithm (3PSF) experiences important estimation errors on the voltage amplitudes, leading to position drift. The nature of these drifts is not physical though, but is rather due to the algorithm itself. As a matter of fact, the 3PSF experiences these errors whenever a second sinusoidal signal is superposed to the signal to analyse. This phenomenon has never been observed on LVDTs since in this case the presence of external fields gives rise to magnetic phenomena, which completely hide this numerical effect. Therefore, it is evident only in ironless structures. To reject it, an efficient reading algorithm has been conceived, making use of standard 3PSF algorithm with a preliminary time-windowing of the acquired signal. The test of this algorithm on simulated and measured signals confirmed its performances. In addition, a further test on a real-time platform defined its non-criticality for real-time I2PS position reading.

Once the complete model of the sensor together with its conditioning algorithms are defined, an optimization process for the I2PS design has been prepared. This procedure is general and constitutes an example of maximization of the sensor's sensitivity. Several design rules are advanced, having the models as reference. The procedure is applied for the specific case of the LHC collimators: the resulting sensor has been actually manufactured and tested, reporting that its performances are within the specifications.

5.1.2. Summary of scientific contributions

- LVDT magnetic interference characterization and possible countermeasures.
- The Ironless Inductive Position Sensor (I2PS) as a replacement solution for the LVDT magnetic interference, reaching immunity to external magnetic fields.
- Low-frequency electromagnetic model of the ironless inductive position sensor (I2PS) in all supply cases.
- Electromagnetic analysis of high-frequency phenomena taking places in circular coils with small curvature radius (such as I2PS coils).

- Modelling and compensation of thermal effects affecting the ironless sensor's position reading.
- Conception of noise-suppression reading algorithm to reject the estimation error of conventional Sine-fit algorithm due to possible additional sinusoidal signals.
- Optimization procedure for maximizing the ratiometric swing. Application to the CERN case study.

5.2. Future development

The research proposed in the previous chapters constitutes a complete study: it gives the possibility to actually design an Ironless Inductive Position Sensor according to the particular application. However, many of the parts presented are even more generic, allowing them to be considered for further research or application in more broad-spectrum problems.

The application of the Ironless Inductive Position Sensor as a novel solution can be seriously taken into account in critical applications as Tokamaks (linear position measurements for plasma control in the vessel, usually characterized by intense magnetic fields), energy plants (as nuclear plants, also characterized by severe nuclear radiations), medical (linear position sensing in imaging machines involving high-intensity magnetic fields), manufacturing processes and similar situations.

Regarding the analytical developments and the algorithms, the low-frequency electromagnetic model is a validated design tool and can be used for technical purposes like application-specific sensor's optimizations or design choices, as well as fast counterchecks in a research framework. The high-frequency analysis constitutes a generic treatment of skin and proximity effects and their influences on magnetic and electric fields in cylindrical coils with low curvature radius. Therefore, it can be applied for studying these effects or be the starting point for the modelling with more complex geometries and/or boundary conditions. The thermal model and compensation constitute again a design tool and a method for studying thermal drifts due to ambient temperature variations in ironless structures. The reading algorithm to reject the effect of superposed sinusoidal signals is also a generic solution whenever this problem can arise; in addition, more complex studies can be performed at the digital signal processing level, to characterize the effect according to the signals parameters (amplitude, frequency, initial phase etc.). Finally, the optimization procedure can be seen as an *incipit* for different kinds of applications.

Regarding the Ironless Inductive Position Sensors itself, the optimized version proposed in the previous chapter will be installed for future tests in the LHC collimators where the magnetic interference effects have been observed and it is likely to replace the Linear Variable Differential Transformers.

References

[1] C. Sutton. *Particle Accelerator*. Available: www.britannica.com

[2] "The International System of Units (SI)," Bureau International des Poids et Mesures 2006.

[3] M. Conte and W. W. MacKay, *An Introduction to the Physics of Particle Accelerators*, 2nd ed. Singapore: World Scientific, 2008.

[4] M. S. Livingston and J. P. Blewett, *Particle Accelerators*. York: McGraw-Hill, 1962.

[5] M. G. Minty and F. Zimmerman, *Measurement and Control of Charged Particle Beams*. New York: Springer, 2003.

[6] S. Russenschuck, *Field Computation for Accelerator Magnets*. Weinheim: Wiley, 2010.

[7] CERN. (2008, 10.09.2008). First Beam in the LHC - Accelerating Science. *CERN Press Release*. Available: press.web.cern.ch

[8] R. Oerter, *The Theory of Almost Everything: The Standard Model, the Unsung Triumph of Modern Physics*: Penguin, 2006.

[9] F. Englert and R. Brout, "Broken Symmetry and the Mass of Gauge Vector Mesons," *Physical Review Letters,* vol. 13, no. 9, pp. 321-323, 1964.

[10] P. W. Higgs, "Broken Symmetries and the Masses of Gauge Bosons," *Physical Review Letters,* vol. 13, no. 16, pp. 508-509, 1964.

[11] H. Bohr and H. B. Nielsen, "Hadron Production from a Boiling Quark Soup: Quark Model Predicting Particle Ratios in Hadronic Collisions," *Nuclear Physics B,* vol. 128, no. 2, p. 275, 1977.

[12] J. Adams, "The LEP Collider: from Design to Approval and Commissioning," CERN, Geneva 1990.

[13] CERN. (2012, 04.07.2012). CERN Experiments Observe Particle Consistent with Long-Sought Higgs Boson. *CERN Press Release*. Available: press.web.cern.ch

[14] S. Redaelli, R. Assmann, P. Gander, M. Jonker, M. Lamont, R. Losito, A. Masi, and M. Sobczak, "The LHC Collimators Controls Architecture - Design and Beam Tests," in *PAC*, Albuquerque, New Mexico, 2007, pp. 344-346.

[15] A. Masi and R. Losito, "LHC Collimators low level control system," *IEEE Transactions on Nuclear Science,* vol. 55, no. 1, pp. 333-340, 2008.

[16] S. Redaelli, R. Assman, P. Gander, M. Jonker, M. Lamont, R. Losito, A. Masi, and M. Sobczak, "The LHC collimator controls architecture - design and beam tests," in *PAC 2007*, 2007, pp. 344-346.

[17] T. Weiler, O. Aberle, R. Assmann, R. Chamizo, Y. Kadi, J. Lettry, R. Losito, and S. Redaelli, "LHC Collimation System Hardware Commissioning," in *PAC*, Albuquerque, New Mexico, 2007.

[18] J. Fraden, *Handbook of Modern Sensors*, 3rd ed.: AIP Press, 2004.

[19] L. K. Baxter, *Capacitive Sensors: Design and Applications*: IEEE Press Series on Electronics Technology, 1997.

[20] F. N. Toth and C. M. Meijer, "A Low Cost, Smart Capacitive Position Sensor," *IEEE Transactions on Instrumentation and Measurement,* vol. 41, no. 6, 1992.

[21] E. Dimovasili, A. Herty, H. M. Durand, A. Marin, F. Ossart, and T. Wijnands, "Radiation induced effects on the sensors of the Hydrostatic Leveling System for the LHC low beta quadrupoles," in *RADECS 2005*, 2005, pp. 2-4.

[22] W. Coosemans, B. Dehning, M. D. Hildreth, A. Marin, G. Mugnai, E. Torrence, J. Prochnow, and F. Roncarolo, "Determination of the accuracy of wire position sensors," in *EPAC 2000*, Vienna, 2000.

[23] W. Coosemans, B. Dehning, M. Hildreth, A. Marin, J. Matheson, G. Mugnai, J. Prochnow, F. Roncarolo, and E. Torrence, "Performance of Wire Position Sensor in a Radiation Environment," presented at the IWAA, Grenoble, France, 1999.

[24] D. S. Nyce, *Linear Position Sensors*. Hoboken, NJ: Wiley-Interscience, 2004.
[25] W. B. Ribbens, *Understanding Automotive Electronics*: Newnes, 2003.
[26] A. Holmes-Siedle, *Handbook of radiation effects*, 2nd ed.: Oxford University Press, 2007.
[27] H. C. Seat, S. Pullteap, and T. Bosch, "An Extrinsic Fibre Optic Interferometer with Possible Signal Fading Compensation for Vibrometric Applications," in *IEEE I2MTC 2005*, 2005, pp. 2236-2241.
[28] X. Zhou and Q. Yu, "Wide-Range Displacement Sensor Based on Fiber-Optic Fabry–Perot Interferometer for Subnanometer Measurement," *IEEE Sensors Journal,* vol. 11, no. 7, pp. 1602-1606, 2011.
[29] Attocube. (2010). *AttoMetrology: Interferometric Displacement Sensor*. Available: http://www.attocube.com
[30] E. J. Friebele, K. J. Long, and M. E. Gingerich, "Radiation damage in single-mode optical-fiber waveguides," *Applied Optics,* vol. 22, no. 11, 1983.
[31] M. N. Ott, "Radiation Effects Data on Commercially Available Optical Fiber: Database summary," in *IEEE REDW*, 2002, pp. 24- 31.
[32] A. F. Fernandez, F. Berghmans, B. Brichard, and M. Decreton, "Toward the Development of Radiation-Tolerant Instrumentation Data Links for Thermonuclear Fusion Experiments," *IEEE Transactions on Nuclear Science,* vol. 49, no. 6, 2002.
[33] D. S. Nyce, "Magnetic Displacement Sensors," in *The Measurement, Instrumentation and Sensors Handbook*, 10th ed: CRC Press, Springer-Verlag and IEEE Press, 1999.
[34] H. Eren, "Inductive Displacement Sensors," in *The Measurement, Instrumentation and Sensors Handbook*, 10th ed: CRC Press, Springer-Verlag and IEEE Press, 1999, pp. 6.26-6.32.
[35] P. Ripka, *Magnetic Sensors and Magnetometers*: Artech House, 2001.
[36] (2007) Shaevitz LVDTs provides rugged position sensing for Super Collider. Available: http://www.meas-spec.com/assets/0/78/136/497/a03b1506-410c-4438-83ad-5b9d42bf86c5.pdf
[37] J. Megusar, "Low temperature fast-neutron and gamma irradiation of Kapton® polyimide films," *Journal of Nuclear Materials,* no. 245, pp. 185-190, 1997.
[38] K. Ara, "A Differential Transformer With Temperature- and Excitation-Independent Output," *IEEE Transactions on Instrumentation and Measurement,* vol. 21, no. 3, pp. 249-255, 1972.
[39] A. Masi, A. Brielmann, R. Losito, and M. Martino, "LVDT Conditioning on the LHC Collimators," *IEEE Transactions on Nuclear Science,* vol. 55, no. 1, pp. 67-85, 2008.
[40] R. Bozorth, "Iron-Nickel Alloys," in *Ferromagnetism*, 3rd ed New York, NY: D. Van Nostrand Company, 1951.
[41] K. Hoselitz, "Magnetically soft materials," in *Ferromagnetic properties of Metals and Alloys*, ed Oxford, GB: Oxford Univ. Press, 1952.
[42] L. Li, "Controlling Annealing and Magnetic Treatment Parameters to Achieve High Permeabilities in 55 Ni–Fe Toroid Cores," *IEEE Transactions on Magnetics,* vol. 37, no. 4, pp. 2315-2317, 2001.
[43] S. C. Saxena and S. B. L. Seksena, "A Self Compensated Smart LVDT transducer," *IEEE Transactions on Instrumentation and Measurement,* vol. 38, no. 3, pp. 748-753, 1989.
[44] D. Crescini, A. Flammini, D. Marioli, and A. Taroni, "Application of an FFT-based Algorithm to Signal Processing of LVDT Position Sensors," *IEEE Transactions on Instrumentation and Measurement,* vol. 47, no. 5, pp. 1119-1123, 1998.
[45] Y. Kano, S. Hasebe, and H. Miyaji, "New Linear Variable Differential Transformer with square coils," *IEEE Transactions on Magnetics,* vol. 26, no. 5, pp. 2020-2022, 1990.
[46] R. S. Weissbach, D. R. Loker, and R. M. Ford, "Test and Comparison of LVDT Signal Conditioner Performance," in *IEEE I2MTC*, Baltimore, MD, 2000, pp. 1143-1146.
[47] T. Weiler, O. Aberle, R. Assman, R. Chamizo, Y. Kadi, J. Lettry, R. Losito, and S. Redaelli, "LHC collimation system hardware commissioning," in *PAC 2007*, 2007, pp. 1625-1627.
[48] A. Danisi, "Simulation of DC Interfering Magnetic Field Effects on the LHC Collimators' LVDT

Positioning Sensors," M.Sc., Electronic Engineering Department, University of Naples "Federico II", Naples, Italy, 2009.

[49] R. Wolf and W. V. Delsolaro, "Magnets Pre-Cycle for LHC Operation," CERN, Geneva, Switzerland 2009.

[50] A. Masi, M. Lamberti, R. Losito, and M. Martino, "Reduction of Magnetic Interference on the Position Sensors of the LHC Collimators," in *IPAC*, San Sebastian, Spain, 2011.

[51] M. Martino, G. Golluccio, R. Losito, and A. Masi, "An analytical model of the effect of external DC magnetic fields on the AC voltages of an LVDT," in *IEEE IMTC 2010*, 2010, pp. 213-218.

[52] R. Bozorth, "Concepts of Ferromagnetism," in *Ferromagnetism*, ed New York, NY: D. Van Nostrand Company, 1951, pp. 1-14.

[53] G. Bertotti, "Maxwell's Equations in Magnetic Media," in *Hysteresis in Magnetism*, ed Oval Road, UK: Academic Press, 1998, pp. 73-102.

[54] J. Jin, *The Finite Element Method in Electromagnetics*. New York, NY: Wiley and Sons, Inc., 2002.

[55] CEDRAT, "Flux® 9 2D/3D Applications User's Guide," ed. Meylan, FR, 2006.

[56] M. Krizek and P. Neittaanmaki, "Finite Elements," in *Mathematical and Numerical Modelling in Electrical Engineering*, ed Dordrecht, NL: Kluwer Academic Publishers, 1996.

[57] I. K. Kang, H. H. Scholefield, and A. P. Matin, "Some Concepts Concerning the New High Permeability 50–50 nickel–iron alloys," *Journal of Applied Physics,* vol. 38, no. 3, pp. 1178–1183, 1967.

[58] G. Spiezia, R. Losito, M. Martino, A. Masi, and A. Pierno, "Automatic Test Bench for Measurement of Magnetic Interference on LVDTs," *IEEE Transactions on Instrumentation and Measurement,* vol. 60, no. 5, pp. 1802-1810, 2010.

[59] P. E. Greenwood and M. S. Nikulin, *A Guide to Chi-squared Testing*. New York, NY: Wiley, 1996.

[60] S. Wu, S. Mo, and B. Wu, "An LVDT-based self-actuating displacement transducer," *Sensors and Actuators A,* vol. 141, no. 2, pp. 558-564, 2008.

[61] *Metals Handbook*, 10th ed. vol. 1: ASM International, 1990.

[62] *Designers Handbook : The when, why and how of Magnetic Shielding*. Blairsville, USA: Westinghouse, 1966.

[63] K.-B. Kim, E. Levi, Z. Zabar, and L. Birenbaum, "Mutual Inductance of Noncoaxial Circular Coils With Constant Current Density," *IEEE Transactions on Magnetics,* vol. 33, no. 5, pp. 4303-4309, 1997.

[64] C. Akyel, S. Babic, and S. Kincic, "New and Fast Procedures for Calculating the Mutual Inductance of Coaxial Circular Coils (Circular Coil-Disk Coil)," *IEEE Transactions on Magnetics,* vol. 38, no. 5, pp. 2367- 2369, 2002.

[65] C. Akyel, S. I. Babic, and M.-M. Mahmoudi, "Mutual Inductance Calculation for Non-Coaxial Circular Air Coils with Parallel Axes," *Progress in Electromagnetics Research,* vol. 91, no., pp. 287-301, 2009.

[66] M. Abramowitz and I. A. Stegun, *Handbook of Mathematical Functions with Formulas, Graphs, and Mathematical Tables*. New York, NY: Dover, 1965.

[67] S. Babic and C. Akyel, "Improvement in calculation of the self- and mutual inductance of thin-wall solenoids and disk coils," *IEEE Transactions on Magnetics,* vol. 36, no. 4, pp. 1970-1975, 2000.

[68] R. R. Nimmo and H. D. Poole, "The Significance of the Sign of a Mutual Inductance," *Mathematical Proceedings of the Cambridge Philosophical Society,* vol. 28, no. 04, pp. 531-537, 1932.

[69] C. Altman and K. Such, *Reciprocity, Spatial Mapping and Time Reversal in Electromagnetics*. Dordrecht: Kluwer, 1991.

[70] R. L. Stall, *The Analysis of Eddy Currents*. Oxford: Clarendon Press, 1974.

[71] J. K. Watson, *Applications of Magnetism*. New York: John Wiley and Sons, Inc., 1980.
[72] M. K. Kazimierczuk, "Skin Effect," in *High Frequency Magnetic Components*, ed Singapore: Wiley, 2009.
[73] A. Massarini and M. K. Kazimierczuk, "Self-Capacitance of Inductors," *IEEE Transactions on Power Electronics,* vol. 12, no. 4, 1997.
[74] M. K. Kazimierczuk, "Winding Resistance at High Frequencies," in *High Frequency Magnetic Components*, ed Singapore: Wiley, 2009.
[75] M. K. Kazimierczuk, G. Sancineto, U. Reggiani, and A. Massarini, "Small-signal High-frequency Model of Ferrite Inductors," *IEEE Transactions on Magnetics,* vol. 35, no., pp. 4185-4191, 1999.
[76] P. J. Dowell, "Effects of Eddy Currents in Transformer Windings," *Proceedings of the IEEE,* vol. 113, no. 8, pp. 1387-1394, 1996.
[77] V. J. Katz, "The Hystory of Stokes' Theorem," *Mathematics Magazine,* vol. 52, no. 3, pp. 146-156, 1979.
[78] G. N. Watson, *A Treatise on the Theory of Bessel Functions*, 2nd ed. Cambridge: University Press, 1966.
[79] I. S. Grant and W. R. Phillips, *Electromagnetism*, 2nd ed.: John Wiley & Sons, 2008.
[80] J. H. Poynting, "On the Transfer of Energy in the Electromagnetic Field," *Philosophical Transactions of the Royal Society of London,* vol. 175, no., pp. 343-361, 1884.
[81] F. Robert, "A theoretical discussion about the layer copper factor used in winding loss calculation," *IEEE Transactions on Magnetics,* vol. 35, no. 5, pp. 3177-3179, 2000.
[82] E. C. Snelling, *Soft Ferrites: Properties and Applications*. London: Iliffe Books, 1969.
[83] M. Ward, *Electrical Engineering Science*: McGraw-Hill, 1971.
[84] H. Pops, "The importance of conductor and control of its properties for magnet wire applications," in *Nonferrous Wire Handbook*. vol. 3, ed: The Wire Association International, 1995.
[85] M. Martino, R. Losito, and A. Masi, "Analytical Metrological Characterization of the Three-Parameter Sine Fit Algorithm," *ISA Transactions,* no., 2011.
[86] S.-T. Wu and J.-L. Hong, "Five-Point Amplitude Estimation of Sinusoidal Signals: With Application to LVDT Signal Conditioning," *IEEE Transactions on Instrumentation and Measurement,* vol. 59, no. 3, pp. 623-630, 2010.
[87] M. Bertocco and C. Narduzzi, "Sine-Fit Versus Discrete Fourier Transform-Based Algorithms in SNR Testing of Waveform Digitizers," *IEEE Transactions on Instrumentation and Measurement,* vol. 46, no. 2, pp. 445-448, 1997.
[88] D. Belega, D. Dallet, and D. Petri, "Performance Comparison of the Three-Parameter and the Four-Parameter Sine-Fit Algorithms," in *IEEE I2MTC*, Hangzhou, China, 2011.
[89] N. M. Vucijak and N. M. Radojevic, "Three, Four and Seven Parameters Sine-fitting Algorithms Applied in the Electric Power Calibrations," in *EUROCON*, Belgrade, Serbia & Montenegro, 2005, pp. 1148-1150.
[90] O. M. Solomon, "The Effects of Windowing and Quantization Error on the Amplitude of Frequency-Domain Functions," *IEEE Transactions on Instrumentation and Measurement,* vol. 41, no. 6, pp. 932-937, 1992.
[91] H. Wen, Z. Teng, and S. Guo, "Triangular Self-Convolution Window With Desirable Sidelobe Behaviors for Harmonic Analysis of Power System," *IEEE Transactions on Instrumentation and Measurement,* vol. 59, no. 3, pp. 543-552, 2010.
[92] A. Datar, A. Jain, and P. Sharma, "Performance of Blackman Window Family in Mchannel Cosine Modulated Filter Bank for ECG Signals," in *IMPACT*, 2009, pp. 98-101.
[93] C. W. Stearns, "A Generalized Hann Window for Apodization of Filtered Backprojection PET Images," presented at the IEEE NSS, Wyndham El Conquistador, Puerto Rico, 2005.
[94] G. Andria, M. Savino, and A. Trotta, "Windows and Interpolation Algorithms to Improve Electrical Measurement Accuracy," *IEEE Transactions on Instrumentation and Measurement,*

vol. 38, no. 4, pp. 856-863, 1989.
[95] D. Belega, D. Petri, and D. Dallet, "Sine-Fitting by the Energy-Based Method in the Dynamic Testing of ADCs," in *IDAACS*, Prague, Czech Republic, 2011, pp. 33-38.
[96] D. Belegat and D. Dallet, "Accurate ADC Dynamic Testing by Means of the Three-Parameter Sine-Fit Algorithm," in *IEEE IMS3TW*, Scottsdale, Arizona, 2009, pp. 1-6.
[97] A. S´arhegyi and I. a. Koll´ar, "Robust SineWave Fitting in ADC Testing," in *IEEE I2MTC*, Sorrento, Italy, 2006, pp. 914-919.
[98] F. C. Alegria, "Bias of amplitude estimation using three-parameter sine fitting in the presence of additive noise," *Measurement,* vol. 42, no. 2009, pp. 748-756, 2009.
[99] F. C. Alegria and A. C. Serra, "Uncertainty of the Estimates of Sine Wave Fitting of Digital Data in the Presence of Additive Noise," in *IEEE I2MTC*, Sorrento, Italy, 2006, pp. 1643-1647.
[100] D. Belega, D. Petri, and D. Dallet, "An Effective Procedure for the Estimation of the Harmonic Parameters of Distorted Sine-Waves," in *IEEE I2MTC*, Graz, Austria, 2012, pp. 1429-1434.
[101] F. J. Harris, "On the use of windows for harmonic analysis with the discrete Fourier transform," *Proceedings of the IEEE,* vol. 66, no. 1, pp. 51-83, 1978.
[102] G. L. Nemhauser and L. A. Wolsey, *Integer and combinatorial optimization*: Wiley, 1988.
[103] L. A. Wolsey, *Integer programming*: Wiley, 1998.
[104] D. Bertsekas, *Convex Analysis and Optimization*: Athena Scientific, 2003.
[105] D. E. Goldberg, *Genetic Algorithms in Search, Optimization and Machine Learning*. Boston, MA: Kluwer Academic Publishers, 1989.
[106] M. Repetto and J. Simkin, "Engineering Analysis for Design Optimization of Differential Transformers," *IEEE Computer- Aided Engineering Journal,* vol. 5, no. 2, pp. 51-53, 1988.
[107] J. K. Sykulski, E. Sykulska, and S. T. Hughes, "Application of Finite Element Modelling in LVDT Design," *COMPEL,* vol. 11, no. 1, pp. 73-76, 1992.
[108] D. Parker, J. Bussink, H. T. v. d. Grampel, G. W. Wheatley, E.-U. Dorf, E. Ostlinning, K. Reinking, F. Schubert, and O. Jünger, "Polymers, High-Temperature," in *Ullman's Encyclopedia of Industrial Chemistry*, ed: Wiley On-line Library, 2012.
[109] M. Tavlet and H. v. d. Burgt, "Radiation Resistance and other Safety Aspects of High-Performance Plastics by ERTA," in *Workshop an Advanced Materials for High-Precision Detectors*, CERN, 1994, pp. 157-167.
[110] *C-60 System User's Manual*: Cypher Instruments, 2005.
[111] M. Martino, A. Danisi, R. Losito, A. Masi, and G. Spiezia, "Design of a LVDT with high rejection to external interfering magnetic field," *IEEE Transactions on Magnetics,* vol. 46, no. 2, pp. 674-677, 2010.
[112] (2008). *Articles about PXI*. Available: http://zone.ni.com/devzone/cda/pub/p/id/174

Curriculum Vitae

- ***Personal Information***

COMPLETE NAME: **ALESSANDRO DANISI**

CURRENT ADDRESS: *110,* RUE DES CORNEILLES, 01630 PERON, FRANCE
ITALIAN ADDRESS: *16,* VIA LEONARDO DA VINCI, 80010 VILLARICCA (NA), ITALY
E-MAIL: alessandro.danisi@live.it
PHONE NUMBERS: +41762749213 / +393881830926 / +41227678521
DATE OF BIRTH: August 12th, 1985
GENDER: Male **NATIONALITY**: Italian.

- ***Occupational Field*:** **ELECTROMAGNETISM ENGINEER**
- ***Working Experience***

RESEARCH ASSOCIATE/DOCTORAL STUDENT

FROM: 1st March 2009 **TO**: *31st* December 2012.
EMPLOYER: **European Organization for Nuclear Research (CERN)**, EN/STI Group, ECE Section. Route de Meyrin, CH-1211 Geneva 23, Switzerland. Supervisor: **Dr. Alessandro Masi** (Alessandro.Masi@cern.ch).
MAIN ACTIVITIES AND RESPONSIBILITIES: Study/FEM Simulation of magnetic phenomena regarding Linear Variable Differential Transformers and their behavior with external magnetic fields. Conception, modeling, optimization and design of a magnetic-field-immune inductive position sensor. Basic Modeling of Thermal aspects.

STAGER

FROM: 1st September 2008 ***TO***: 31st January 2009.
EMPLOYER: **European Organization for Nuclear Research (CERN)**, EN/STI Group, ECE Section. Route de Meyrin, CH-1211 Geneva 23, Switzerland. Supervisor: **Dr. Alessandro Masi** (Alessandro.Masi@cern.ch).
MAIN ACTIVITIES AND RESPONSIBILITIES: Study of Fields' Behaviour in electromagnetic sensors, Study of simulation technique for electromagnetic problems, 2D and 3D simulation (using FLUX) of Electromagnetic Sensors.

- ***Education History***

PH. D. IN ELECTRONIC ENGINEERING

FROM: January 2010 **TO**: expected December 2012.
INSTITUTE: Swiss Federal Institute of Technology Lausanne (EPFL) – IMT-LAI Laboratory.
MAIN SUBJECTS: Study of Magnetic interference on LVDTs. Electromagnetic Modeling (analytical and FEM-aided), design and optimization of a magnetic-field immune electromagnetic sensor. **Thesis title: Ironless Inductive Position Sensor for Harsh Magnetic Environments (Director: Prof. Y. Perriard**, Yves.Perriard@epfl.ch**)**.

MASTER DEGREE IN ELECTRONIC ENGINEERING (EMPHASIS ON ELECTROMAGNETISM)

FROM: February 2007 **TO**: May 2009
INSTITUTE: University of Naples "Federico II" – Engineering Department. 80, P.le Tecchio, Naples (ITALY).
MAIN SUBJECTS: Antennas, Solid State Physics, Superconductivity, Optics, Remote Sensing, DSP, RF/Microwave Theory and Measurement, Transmission Lines, EMC, Business and Project Management, Automations Technology, Power Electronics, FEM Simulations techniques. **Thesis: Simulation of DC Interfering Magnetic Field Effects on the LHC Collimators' LVDT Positioning Sensors (Directors: Prof. Vittorio G. Vaccaro** – vaccaro@na.infn.it**, Prof. G. Ruello** – giuseppe.ruello@unina.it**)**. Grade: **110/110 with honors** (May 28th, 2009).

BACHELOR DEGREE IN ELECTRONIC ENGINEERING

FROM: October 2003 **TO**: January 2007
INSTITUTE: University of Naples "Federico II" – Engineering Department. 80, P.le Tecchio, Naples (ITALY).
MAIN SUBJECTS: Electro-techniques, Computer Science and Programming, Chemistry, Electronics, Signal Theory and Transmission, Basic Control Theory, Electromagnetic Fields, Microwave Theory, Digital IC, Electronic instrumentation control and measurement, Electromagnetic Compatibility. **Thesis Work:**

Synthetic Aperture Radar Simulation of Fractal Oil Slicks in Ocean Environments (Director: Prof. G. Ruello – giuseppe.ruello@unina.it**).** Grade: **110/110 with honors** (January 31st, 2007).

DIPLOMA OF HIGH SCHOOL (EMPHASIS ON SCIENCE)

FROM*:* September 1998 **TO***:* July 2003

INSTITUTE*:* Liceo Scientifico Statale "A.M. de Carlo", 188, Via Marchesella, 80014 Giugliano in Campania, ITALY.

MAIN SUBJECTS*:* Mathematics, Latin, Philosophy, Chemistry, Biology, Astronomy, Physics. Final Grade: **100/100**.

▪ *Personal Skills and Competences*

MOTHER TONGUE*:* Italian.

OTHER LANGUAGES*:* English (*Writing*: Advanced; *Listening*: Advanced; *Reading*: Advanced; *Speaking*: Fluent), French (*Writing*: Intermediate; *Listening*: Intermediate, *Reading*: Intermediate; *Speaking*: Intermediate).

TECHNICAL SKILLS AND COMPETENCES*:* Electromagnetic Analytical Modeling (Advanced), Applied Knowledge of Magnetic Materials (Advanced), Finite Element Method (Advanced), Computational Electromagnetics (Advanced), Magnetic/RF/Microwave Measurements (Extensive), EMC (Elementary), Metrological Characterization of EM sensors (Extensive), Electromagnetic Devices Design and Prototyping (Extensive), Accelerator Physics and Technology (Extensive), Optimization Techniques (Extensive), Electronic Instrumentation control and programming (Elementary), Scientific and Technical writing/presentation (Advanced), Technical/Commercial Contact with Companies (Extensive).

COMPUTER SKILLS AND COMPETENCES*: FEM Simulators*: Cedrat FLUX 2D & 3D (Advanced), Ansoft Maxwell (Elementary), HFSS (Elementary). *Programming*: C++ (Elementary), Python (Elementary), Matlab (Advanced), NI Labview (Extensive), IDL (Elementary). *Circuit Simulators*: Microwind (Elementary), Spice (Extensive). *Office Software*: MS Office package (Advanced), Visio (Extensive), Image/Audio/Video editing (Extensive).

SOCIAL SKILLS AND COMPETENCES*:* Organizational, Communicative and Relational skills, Student Supervision Activity, Result-Achieving, Problem Posing/solving attitudes, Persistence attitude, Attitude for working in a team, Work in international environments.

HOBBIES*:* Reading, Running (2012 Berlin Marathon finisher), Hiking, Table Tennis.

DRIVING LICENSES*:* Category B.
NATIONAL SERVICE*:* Exempt.

▪ *Training Courses*

1. January, 2012 (5 days). **Labview for Experts (Core III and Connectivity)**. CERN, Switzerland. Ref: **Joseph Tagg**, National Instruments Switzerland Corp., Switzerland.
2. October, 2011 (3 days): **Piezoelectric materials**. CERN, Switzerland. Ref: **CEDRAT Technologies**, France.
3. September, 2011 (14 days): **CERN Accelerator School on Intermediate Accelerator Physics**. Chios, Greece. Ref: **Barbara Strasser**, CERN, Switzerland. Laboratory on: **RF Measurements Techniques**.
4. March, 2011 (6 days): **Design of Experiments**. Lausanne, Switzerland. Ref: **Dr. Jean-Marie Fuerbringer**, EPFL, Switzerland.
5. June, 2010 (10 days): **Highlights in Microtechnology**. Neuchatel, Switzerland. Ref: **Marcella Giovannini**, EPFL, Switzerland.
6. October, 2009 (1,5 days): **Python Scripting for FLUX**. Grenoble, France. Ref: **Dr. Patrick Lombard**, Cedrat Group, France.
7. October, 2009 (120 hours): **General and Professional French Course**. CERN, Switzerland. Ref: **Lucette Fournier**, CERN, Switzerland.
8. November, 2008 (3 days): **Cedrat FLUX 2D & 3D Advanced Applications**. Morges, Switzerland. Ref: **Dr. Daho Taghezout**, Applied Magnetics, Switzerland.
9. June, 2002: **European Computer Driving License (ECDL)**. Giugliano, Italy. Ref: **Associazione Italiana Calcolo Automatico** (AICA).

▪ *List of Publications and Presentations*

Journal papers

1. A. Danisi, A. Masi, R. Losito, Y. Perriard: "*High-Frequency Electromagnetic Effects Modelling of an Ironless Inductive Position Sensor*", submitted to IEEE Transactions on Magnetics, August 2012.

2. A. Masi, A. Danisi, M. Di Castro, R. Losito: "*Real-Time High-Precision Reading Algorithm for an Ironless Inductive Position Sensor*", submitted to IEEE Transactions on Nuclear Science, July 2012.
3. A. Danisi, A. Masi, R. Losito, Y. Perriard: "*Electromagnetic Analysis and Validation of an Ironless Inductive Position Sensor*", accepted for IEEE Transactions on Instrumentation and Measurement, June 2012.
4. A. Masi, A. Danisi, R. Losito, Y. Perriard: "*Characterization of Magnetic Field Immunity of an Ironless Position Sensor Prototype*", accepted for IEEE Sensors Journal, February 2012.
5. A. Masi, A. Danisi, R. Losito, M. Martino, G. Spiezia: "*Study of Magnetic Interference on a LVDT: FEM Model and Experimental Measurements*". Journal of Sensors, Hindawi Publishing Corp., vol. 2011.
6. M. Martino, A. Danisi, R. Losito, A. Masi, G. Spiezia: "*Design of an LVDT with High Rejection to External Interfering Magnetic Fields*". IEEE Transactions on Magnetics, February 2010.

Conference Proceedings

1. A. Danisi, A. Masi, R. Losito, Y. Perriard: "*Modelling and Compensation of Thermal Effects on an Ironless Inductive Position Sensor*", proceedings of ECCE 2012, Rayleigh, North Carolina, September 2012.
2. A. Masi, A. Danisi, M. Di Castro, R. Losito: "*High Accuracy Reading Algorithm for Ironless Linear Position Sensor*". Accepted for publication in Proceedings of IEEE Real Time Conference 2012.
3. A. Danisi, A. Masi, R. Losito, Y. Perriard: "*Electromagnetic Modeling of an Ironless Position Sensor*". Accepted for publication in Proceedings of IEEE I2MTC 2012.
4. A. Masi, A. Danisi, R. Losito, Y. Perriard: "*Ironless Position Sensor with Intrinsic Immunity to External Magnetic Fields*". Proceedings of IEEE SENSORS 2011.
5. A. Masi, A. Danisi, R. Losito, M. Martino, G. Spiezia: "*Study of Magnetic Interference on a LVDT Prototype*". Proceedings of IEEE I2MTC, 2010.
6. A. Danisi, G. di Martino, A. Iodice, D. Riccio, G. Ruello, M. Tello, J. J. Mallorqui, C. Lopez-Martinez: "*SAR Simulations of Ocean Scenes Covered by Oils Slicks with Arbitrary Shapes*". Proceedings of IGARSS 2007.
7. M. Tello, J. J. Mallorqui, C. Lopez-Martinez, A. Danisi, G. di Martino, A. Iodice, D. Riccio, G. Ruello: "*Characterization of Local Regularity in SAR Imagery by Means of Multi-Scale Techniques: Application to Oil Spill Detection*". Proceedings of IGARSS July 2007.

Presentations and Seminars

1. *"Study and brand-new countermeasures for the LVDT Magnetic Interference"*, Seminar during the course "Integrated Transducers" by Dr. Miroslav Markovic, EPFL, November 4th, 2011.
2. *"LVDT magnetic interference on the LHC collimators: study and possible solutions*", presented at EN/STI Students' coffee, 5th Meeting, CERN, July 12th, 2011.
3. "*Simulation of DC Magnetic Field Effects on the LHC Collimators' LVDT Positioning Sensors*", presented at the FLUX Users' Conference, Autrans, France, October 2009.

SEPTEMBER, 2012